An Inverse Finite Element Approach for Identifying Forces in Biological Tissues

by

P. Graham Cranston

A thesis
presented to the University of Waterloo
in fulfillment of the
thesis requirement for the degree of
Master of Applied Science
in
Civil Engineering

Waterloo, Ontario, Canada, 2009

© P. Graham Cranston 2009

I hereby declare that I am the sole author of this thesis. This is a true copy of the thesis, including any required final revisions, as accepted by my examiners.

I understand that my thesis may be made electronically available to the public.

P. Graham Cranston

Abstract

For centuries physicians, scientists, engineers, mathematicians, and many others have been asking: 'what are the forces that drive tissues in an embryo to their final geometric forms?' At the tissue and whole embryo level, a multitude of very different morphogenetic processes, such as gastrulation and neurulation are involved. However, at the cellular level, virtually all of these processes are evidently driven by a relatively small number of internal structures all of whose forces can be resolved into equivalent interfacial tensions γ. Measuring the cell-level forces that drive specific morphogenetic events remains one of the great unsolved problems of biomechanics. Here I present a novel approach that allows these forces to be estimated from time lapse images.

In this approach, the motions of all visible triple junctions formed between trios of cells adjacent to each other in epithelia (2D cell sheets) are tracked in time-lapse images. An existing cell-based Finite Element (FE) model is then used to calculate the viscous forces needed to deform each cell in the observed way. A recursive least squares technique with variable forgetting factors is then used to estimate the interfacial tensions γ that would have to be present along each cell-cell interface to provide those forces, along with the attendant pressures in each cell.

The algorithm is tested extensively using synthetic data from an FE model. Emphasis is placed on features likely to be encountered in data from live tissues during morphogenesis and wound healing. Those features include algorithm stability and tracking despite input noise, interfacial tensions that could change slowly or suddenly, and complications from imaging small regions of a larger epithelial tissue (the frayed boundary problem). Although the basic algorithm is highly sensitive to input noise due to the ill-conditioned nature of the system of equations that must be solved to obtain the interfacial tensions, methods are introduced to improve the resulting force and pressure estimates. The final algorithm returns very good estimates for interfacial tensions and intracellular cellular pressures when used with synthetic data, and it holds great promise for calculating the forces that remodel live tissue.

Acknowledgements

I would first like to thank my supervisor, Prof. G. Wayne Brodland, without whose tireless support this project would never have reached completion. His ability to understand and explain mechanical phenomena at the deepest levels is as inspiring as it is uncanny.

Sincerest thanks to my colleagues, Tony Leung, Caleb Horst, and Paul Groh, for your immeasurable help in completing this thesis, and innumerable memories. Very special thanks to Jim Veldhuis who provided unflappable technical support not to mention making the experience an enjoyable one.

I wish to thank my sister Brittany for helping through the biology that otherwise would have left me baffled.

Thanks to Prof. Sriram Narasimhan for his technical help and guidance.

Many thanks to my family for their support, and my wonderful wife Sharon for putting up with me. I love you all.

Finally, thanks to Pete Thompson, my partner-in-crime and stalwart friend. You know what you did.

This work was funded in part by a Human Frontier Science Program (HFSP) grant to Prof. G. Wayne Brodland.

Dedication

To my wife, Sharon, whom I love. That we should all be so lucky...

If I have seen further it is only by standing on the shoulders of giants.

-Sir Isaac Newton

Contents

List of Figures

List of Tables

Chapter 1

Introduction

One of the unsolved problems in biology is the identification of forces which drive the self-rearrangement of biological cells. Such fundamental processes as cell sorting, cancer metastases, wound healing, embryogenesis, and a host of other phenomena are all examples of large scale tissue re-shaping resulting from small scale re-organisation of individual cells. The motions in these processes must be driven by forces, in accordance with the laws of physics; wherever a mass is displaced, it must be driven by a force.

Though much research has been done investigating the processes themselves – the topological changes and biological factors affecting them – very little has been done to uncover the nature of the forces driving these motions. Finite element (FE) models based on the assumption that tensions along cell-cell interfaces provide possible explanations for cell sorting [7, 9], wound healing [45], neurulation and other embryogenetic processes [12], amongst others in both 2- and 3-dimensions. These belong to the class of computational models called forward models. They simulate the motions of live cells based on a starting configuration and certain mechanical properties of the cell mass.

If the assumptions in these forward models are correct, it should be possible, given a displacement history, to determine the interfacial tensions and other forces driving those displacements. There are two classes of data which are available: synthetic data and live data. Synthetic data are generated using the forward model *Simba* [6, 11], whose output is a displacement history. Live data are gathered by directly observing displacements in live cells over time to compile a displacement history.

There are a number of reasons to investigate these forces. Obviously, a deeper understanding of forces driving any motion imparts a deeper understanding of the motion itself. The capability to determine driving forces in specific structures within a cell will refine attempts to comprehend – and perhaps control – certain morphogenic or embryogenic processes at a more fundamental level. By manipulating the genome of an organism to express or suppress certain genes, it may even be possible to determine the contributions of specific structural proteins to the forces

in these structures. A breakthrough of such magnitude could revolutionise biology and medicine. For example, it is one thing to know that spina bifida, the most common birth defect in humans, is a failure of the neural tube to close [76]; it is an entirely different thing to know which structures or perhaps even proteins generate the forces necessary for correct neural tube formation.

The algorithm developed here could also be used to further validate and tune existing forward models. Since algorithm is based on the existing forward model, positive results using live data would indicate that the assumptions underlying the forward models are likely sound. The results of the new algorithm could also be used be used to set the input parameters of the forward model so that they accurately represent the particular organism being studied.

The purpose of this study is to develop an algorithm to determine from which sub-cellular structures the forces driving cell motions arise. This algorithm, colloquially called *Scar*, utilises the existing FE model *Simba* to describe patches of biological cells in terms of nodes, edges, and cells. With this basis as a starting point, equations are developed to describe the relationships between forces in cell-cell interfaces and other structures within the cells, and the nodal forces in the FE model. The completed algorithm is used to identify forces generated by specific structures within cell patches from the synthetically generated displacement histories.

The remainder of this treatise is structured as follows: first, a description of the FE model, *Simba*, on which this work is based, as well as a review of the current state of the art in tissue mechanics and parameter estimation. Following that, the indentification algorithm is developed from the underlying FE model. The algorithm, *Scar*, is designed to accommodate live data and all the particular challenges associated therewith. With the algorithm developed, *Scar's* performance is assessed using synthetic data, with emphasis placed on how that performance is affected by various tuning factors, and discuss these results. Finally, conclusions and recommendations for further development are presented.

This work is sometimes presented in the context of wound healing responses, as a result of collaborations with Professor Shane Hutson. Professor Hutson's lab at Vanderbilt University in Tennessee are specialists in biophotonics. They investigate the physical mechanisms involved in laser tissue ablation, and the use of laser-microsurgery to probe forces driving morphogenesis.

Chapter 2

The State of the Art

This thesis makes use of tissue mechanics modelling and experimentation, and parameter estimation methods. Accordingly, this chapter begins with a literature review of both tissue mechanics and parameter estimation, highlighting some of the seminal and recent results in both fields. It concludes with a detailed discussion of the finite element model on which this study is based.

2.1 Tissue Mechanics

For the better part of a century, scientists and engineers alike have been striving toward a rigorous understanding of how the many anatomical structures of an organism arise. A vast body of literature on the subject reveals approaches to the problem at tissue, cell, and sub-cellular scales. Figure 2.1 shows the key structures at the tissue, cellular, and sub-cellular scales, which interact to give strength to an organism and determine its form. The elements of the cytoskeleton and the cell membrane give structure and strength to each cell. Each cell, in turn, gives structure and strength to the tissues which they form. Some of these structures can also generate forces to alter the shape of cells and remodel entire tissues.

In this section, the hierarchy of elements which compose organic tissues, their interactions, and the morphogenic processes which result are discussed. I also discuss experimental programs which investigate the mechanics properties of these elements, as well as the forces acting on and through them. From the knowledge gained through observation and experimentation, several computational models of cell and tissue mechanical behaviour have been, and continue to be developed.

2.1.1 Cell Membrane and Cytoskeleton

The cell membrane is composed of a phospho-lipid bilayer, which is in tension from the intracellular pressure. The membrane of typical animal cells is from 6 to 10

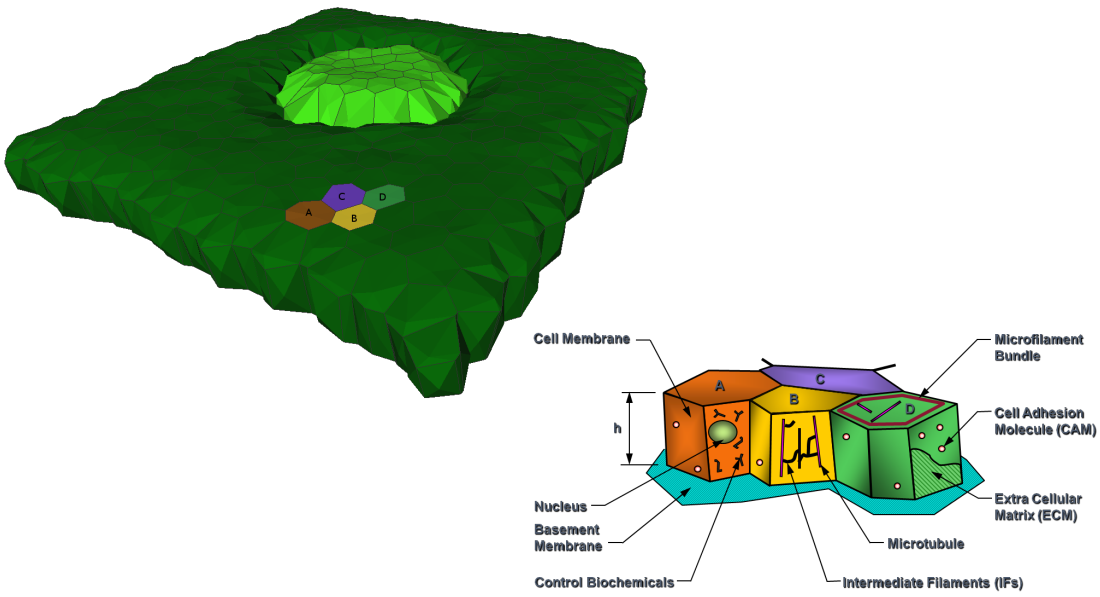

Figure 2.1: The multiple scales in the structure of an organism

nm thick. Scattered about the membrane are many transmembrane and surface molecules. The membrane is partially connected to aspects of the cytoskeleton at specific sites across its surface [19].

At the interior of the cell are found the various structural elements collectively called the cytoskeleton. The cytoskeleton is a network fibrous proteins which serve a variety of functions in the cell, including determination and maintenance of cell shape, mechanical strength and integrity, support and intracellular transport of organelles, and chromosome separation during mitosis/meiosis, to name a few [19, 28]. The three primary classes of protein are microfilaments, intermediate filaments, and microtubules.

Microfilaments are composed of the protein actin. Actin is present in all cells as a thin layer just inboard of the cell membrane (the subcortical region of the cell). This structure is also known as the cortical actin layer [19]. It is composed of series of antiparallel, mutually sliding actin filaments, connected by myosin bridges [4]. In embryonic epithelial cells of some species – including the *Drosophila melanogaster* – actin is also present in a bundle surrounding the apical end of the cell [4, 65]. Actin is also present in bundles criss-crossing the cell, which reinforce the cortical actin [19]. The microfilaments contract, generating tensile forces along and in the vicinity of the cellular membrane. Apical bundles of microfilaments in a group of neighbouring cells can act in concert to create contractions over large distances along a tissue [4].

Intermediate filaments are a large and varied class of proteins. They form a stabilizing network of fibres which gives mechanical strength and integrity to the cell by bracing the microfilaments and microtubules They also aid in supporting organelles within the cell [19].

Microtubules are the largest structures of the cytoskeleton, and are also composed of actin. They provide structural rigidity and aid in cell locomotion. They are also transport agents for proteins and organelles within the cell, and aid in shape changes during cell division [19]. Growing and mutually sliding microtubules are primarily for cell elongation during mitosis, but can also resist tensions applied to the cell [4].

For additional details regarding the physical structures within the cell, the reader is directed to *The Dynamic Architecture of a Developing Organism* [5]. Chapter 2 details the function of cytoskeletal components, and how their actions manifest at the tissue level. The treatise is presented in terms of mechanical stresses and strains, thermodynamic equilibrium, self-equilibration, oscillations, and large responses to small stimuli.

2.1.2 Cell

Several instruments exist to investigate how the cytoskeletal components manifest physically at the cell level. Below the tissue scale, traditional engineering methods to measure mechanical properties of a material simply do not work. One cannot place a cell in a loading frame to measure its force-displacement behaviour and derive constitutive relationships. Testing a cell in such a manner is akin to trying to determine the properties of a polymeric molecule by testing a whole sheet of rubber. A different approach is needed.

One of the earliest devices to probe the mechanical properties of single cells was micropipette aspiration [28, 60]. A glass pipette is brought into contact with the cell, and a small negative pressure is applied. Deformations over time are observed directly by microscope. Forces are calculated from the pipette geometry and the applied pressure. Micropipette aspiration is capable of applying forces on the order of $10pN - 10\mu N$ [60].

A more recent survey paper indicates that forces can also be calculated according to Laplace's Law, which relates transmembrane pressure to membrane tension and curvature, given below in Eq. (2.1) [61]. The relationship assumes an ideal thin-walled spherical membrane in tension. Transmembrane pressure, ΔP, is the pressure in the pippete relative to the pressure in the cell. The radius of curvature of the membrane is denoted by ρ, and the tension in the membrane is γ. The arrangement is shown schematically in Figure 2.2. Interestingly the original paper by Mitchison notes that the stiffnesses measured by

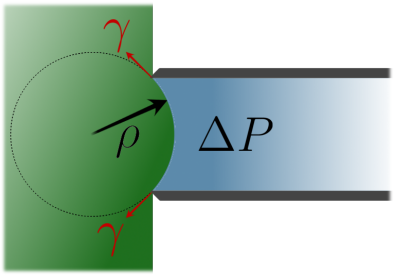

Figure 2.2: Micropipette aspiration: Laplace's Law relating membrane tension and transmembrane pressure

his device were higher than predicted by Laplace's Law, indicating that some factor other than membrane tension was resisting the deformation [60].

$$\gamma = \frac{\Delta P \times \rho}{2} \tag{2.1}$$

Using the micropipette technique, researches have measured tensions in the basal cortical membranes of single *Dictyostelium* cells *in vitro*. The tensions were found to be $1.50 dyne/cm$ or $1.5 mN/m$. The same study also found that myosin I motors are a component necessary for generating cortical tension [21].

By using a second pipette, the adhesive properties of the cell membrane can also be measured. A microsphere coated with antibodies directed at cell-surface molecules can be manipulated by the second pipette, while the first holds the cell immobile. By bringing the microsphere into contact with the cell and then withdrawing it, the strength of the adhesion can be measured [28].

Another method of measuring properties of single cells or even large molecules is atomic force microscopy (AFM). A probe on the end of a flexible beam is driven into the cell, deforming its surface. A laser is then reflected off the beam thereby measuring its position. Force information is calculated by approximating the position of the end of the beam as a linear spring. Displacement measurements are accurate to $\sim 1nm$ [28].

AFM can be used to map the stiffness of living cells by taking displacement and force measurements at regular intervals of $10 - 100nm$. It then remains to solve the contact mechanics problem shown below in Eq. (2.2), first treated by Hertz in 1882[28]. The stiffness of the cell, E, can be determined assuming the cell is planar and linear elastic over the deformation, where α is the half-angle of the conical probe tip. F is the force applied on the cell surface causing it to displace by a distance δ, and ν is Poisson's ratio for the cell, often taken as $\nu = 0.5$ [28].

$$\delta^2 = \frac{\pi}{2} \frac{F(1-\nu^2)}{E \, tan\alpha} \tag{2.2}$$

Two final methods for investigating the mechanical properties of single cells rely on the manipulation of a small bead which has been coated to adhere to the cell surface, similar to that used in the two pipette technique above. The bead is manipulated in one of two ways. One method uses a pair of laser beams, utilising the momentum of the photons to manipulate the bead. The displacement of the bead is observed directly by microscope. This apparatus, also known as 'optical tweezers', is capable of generating forces on the order of $1 - 200pN$. The second method relies on magnetism to manipulate the bead, and is capable of applying forces on the order of $0.1 - 10\mu N$ [28]. Forces on the beads cannot be directly measured. Instead, an empirical calibration is used, often by manipulating the bead in a fluid of known viscosity, and calculating the drag force according to Stoke's Law, Eq. (2.3), where μ is the fluid viscosity, r is the radius of the bead, and v is the velocity [22].

$$F = 6\pi\mu r v \tag{2.3}$$

The optical tweezer method has led to several important findings. One study was able to monitor interactions between the cell membrane and the cytoskeleton, and also to measure mechanical properties of the membranes themselves [20]. A subsequent study showed that membrane tension may regulate cell surface area through the rate of endo- and exocytosis [22, 61]. By applying a force to membrane tethers, it has been shown that membrane tension is continuous, and that continuity was experimentally observable when any point of the membrane not adhered to the substrate was tested [61].

For other examples of the use of micropipette aspiration, AFM, optical tweezers and magnetic bead rheology for membrane tension and mechanical property measurement, see [20, 21, 22, 28, 61] and references therein.

With regards to sub-cellular structures, researchers have been able to measure the stiffness of actin by a variety of methods, reporting values for E_{actin} between $1.5GPa$ and $2.5GPa$. Most of these studies used optical and x-ray diffraction techniques and tested muscular actin [28].

All the methods mentioned here, whether for tissues or single cells, require excising that tissue or cell from the host organism, with the possible exception of AFM. In this manner, they are highly invasive and preclude measurement of mechanical properties *in vivo*. Given the dynamic nature of biological tissues, especially during processes like embryo- and morphogenesis and wound healing responses, this shortcoming is significant. That being said, these methods have produced invaluable results which led to the early mechanical models of cells, essential to the development of todays finite element and continuum models described in §2.1.4 and §2.2.

The forces generated by, and the stresses transmitted through, the various elements of the cytoskeleton shown in Figure 2.1 each contribute to a force along the interface between two cells, which is denoted γ. The distribution of the interfacial forces is responsible for the self-rearrangement of biological cells [4, 19, 38, 65, 30]. This process is discussed further in the next section.

2.1.3 Tissue

There is now sufficient background to discuss the self-rearrangement of biological cells. Many prominent authors have stated that cell self-rearrangement – such as embryonic development, morphogenetic processes, cell sorting and wound healing responses – can be described from a purely mechanical basis [4, 5, 19, 38]. These statements have been supported experimentally, and many such experiments are discussed in this section. This is not to say that neither chemistry nor genetics play a role in morphogenesis. Effects of mechanical triggers may be chemically or genetically regulated, and vice-versa [4]. In this study, I focus on the mechanical

system, not to discard the chemical or genetic, but simply to acknowledge them as outside the current scope.

There are two mechanisms for getting differentiated cells in an embryo into their correct locations: differentiation based on position and position based on differentiation. The former theory results in differentiated cells automatically finding themselves in their correct anatomical positions. The later requires that each cell type includes some property or set of properties which cause it to preferentially move to some location. In animal development both mechanisms are in action [38]. As the focus of this study is the identification forces driving cell *m*otions, only the second mechanism is discussed.

Cell sorting (differentiation controlling position) was first observed by Wilson in the simplest of all multicellular organisms: the sponges [38]. Sorting was later demonstrated in embryonic vertebrates. In both cases, the cells were dissociated and mixed randomly. The dissociated cells then reassembled themselves into functioning organisms. Wilson concluded that the movements he observed had to have occurred simply to reassemble the individual cells [86]. The result implies that the forces driving sorting must come from the cells themselves [38].

Some time later, Holtfreter observed sorting using species-specific pigmentation of cells to track their movements directly. He hypothesised that the same forces which drove the cells to re-sort themselves could also be responsible for the original sorting of newly differentiated cells during embryogenesis [42]. His hypothesis implies that cell sorting is an appropriate analogue for the study of embryogenesis. Holtfreter also suggested that differential adhesion between cell types may be *among* the properties which lead to sorting. Further work along these lines led to the discovery of cadherins, N-CAMs, and other cell surface proteins responsible for adhesion.[38].

Townes and Holtfreter performed experiments in morphogenesis with an aggregate of neural cells and certain other different cell types. They observed that no matter which of three different starting configurations was used, the mass always tended to the same final geometry: a mass of neural cells surrounded by other cells [82]. This suggested that the same – or at least similar – mechanism was responsible for each of engulfment, invagination, and cell sorting [38]. Later, Steinberg also proposed a common mechanism behind each instance of cellular self-rearrangement [78, 77].

There is extensive experimental evidence to suggest that the mechanism driving cellular self-rearrangement is mechanical in nature. Infolding of neural plate (neurulation) has been shown to be driven by active contraction of actin-myosin on the apical surface of the neural plate [12, 14, 49]. Harris reports on experiments completed by Grim where non-muscular cells were grafted into premuscular masses at the wing buds of chicken embryos. These cells took on the geometry of muscle cells appropriate for that location. Harris postulates that the signals which caused this event could be shown to be physical (rather than chemical or positional biology) if the experiment were repeated with inert material such as silicone rubber

[38]. Additional experiments with the slime mould *Physarum* also support such an assertion [5].

Harris gives a list of requirements for tissues to reshape themselves mechanically [38]:

1. There must be two or more mutually opposed forces, that collectively are strong enough to change the geometry of the system.
2. The relative strengths of at least some of these forces must change as functions of the existing geometry.
3. These changes in strength must be such that the forces are exactly counterbalanced when (and only when) the correct geometrical shape or arrangement exists.
4. For all (nearby) shapes or arrangements, the directions of the imbalanced forces must be such as to pull the system back toward this correct geometry.

Harris seems to neglect the possibility of the orientations of the forces changing in item #2 rather than the magnitude.

Having established that morphogenesis is governed by a set of mechanical forces generated by structures within the cell themselves, one must now ask 'but what is the nature of these forces'? Historically, there have been two theories describing specifically how interfacial forces drive cellular self-rearrangement. The first was Steinberg's *Differential Adhesion Hypothesis* (DAH) [37]. He regarded cell sorting as logically equivalent to the behaviour of immiscible liquids. Just as liquids with higher intermolecular adhesion will form droplets suspended in the other liquid, so will cells of one type sort out to the interior of others, with cell-cell adhesion taking the place of molecular adhesion. He proposed that cells sort out internally because their cell-cell adhesion forces are higher [77].

Three sets of observational evidence were presented for the DAH [78].

1. Transitive hierarchy. If cell type A engulfs cell type B, and cell type B engulfs cell type C, then cell type A will engulf cell type C. Steinberg demonstrated this for all 56 combinations of 8 different cell types and it always held.
2. If one type sorts internally to another, then it will also be engulfed by that other type.
3. Those cell types which sort more internally are also more resistant to flattening out of aggregates of their type.

There is significant opposition to the DAH. For example, all three sets of observations are equally consistent with a cell's cortical contractibility (tensions in the cortical surface) being responsible for sorting, rounding, and engulfment. In

fact, item #1 would hold for any theory based on a quantitative difference. Item #2 merely indicates that the forces responsible for sorting are also responsible for engulfment, while item #3 suggests that these same forces are also responsible for the tendency of aggregates to round up [37].

The alternative theory – called the *Differential Interfacial Tension Hypothesis* (DITH) – proposes that differences in the tensions in the cortical surface drive cell self-rearrangement [6, 9, 37, 38]. In liquids, molecular adhesion results in an apparent contractile film on the surface; in tissues, surface contractility is the likely cause of surface tension-like effects [38]. Note however, that none of the observed phenomena could exist if the cells did not adhere to one another. Harris posits that there are two elements to cell sorting. The adhesion of cell types (by N-CAM or the cadherins) sorts the cells according to histotype, and the differential cortical tensions arrange the groupings into their final positions, where the stronger contractile forces move those cells toward the interior of the mass [38]. Many researchers agree that the geometric fate of differentiated cells cannot be governed by adhesion alone, but is the result of the interplay between adhesion and cell surface tensions [41, 53, 55, 69].

A paper attempting to refute the DITH details an experiment designed to confirm the DAH [30]. Motions in a mass of cells were tracked. The mass was composed of cells which were identical in all ways except for their surface adhesion molecules. In this way, any sorting observed must therefore be due to differential adhesion [30]. Others have noted, however, that under these conditions, while the cells do group themselves according to histotype, they fail to sort one type internally to the other [38]. This experiment is a classic case of confirmation bias; the experimenter designed his experiment such that it could only confirm his hypothesis. The DITH does not deny that intercellular adhesion plays a role in sorting, but states that ultimately it is the interfacial tensions which govern the final position of cells, not the intercellular adhesions which merely keep the mass together [6].

Measuring Tissue Stresses

There are, experimental techniques to investigate quantitatively the state of stress in tissues. The first and perhaps most obvious is dissection. At any particular point of interest, the tissue is incised and the recoil of the surrounding tissue is observed. Hole drilling has long been used to evaluate *in-situ* stresses in conventional building materials, and even has an ASTM standard method [2]. For biological tissues, it is important to ensure that active contractile responses from the surrounding tissue are eliminated if the precise state of stress is to be found. A series of such cuts can be used to compile a succession of stress reactions to active forces during cellular self-rearrangement [4].

Dissections have led to innumerable and valuable results. Laser microsurgery of *D. melanogaster* embryos have shown the embryonic epithelium is in tension. The same study was also able to show the existence of isotropic tension in the amniosera

– the structure beneath the epidermis – and that both these tensions are integral to *D. melanogaster* dorsal closure [50].

Dissections have been refined to such a point that single cells, single membranes, or even single cytoskeletal components can be ablated by laser [13, 15, 40, 54, 80]. In the discussion so far, it has been shown that observing self-rearrangement of cells is an excellent avenue to learn about embryonic development, presupposing that the cells are rearranging themselves in such a way that they can be observed. By ablating small groups or single cells, one can trigger primary wound healing [64]; in this way can one observe the self rearrangement of cells in a location that is easily observable, and in the desired cell types. Just as certain morphogenetic processes can be studied as surrogates for wound healing, so can wound healing be studied as a surrogate for embryo- and morphogenesis [83]. One can observe both the recoil – giving insight to the state of stress in a tissue at a particular stage of development – and the primary wound healing response: an excellent example of cellular self-rearrangement.

Davidson et al. were able to use laser microsurgery to define three distinct phases in embryonic wound healing: assembly of supracellular actin filaments in epithelial cells at the wound margin, contraction and ingression of deep cells exposed by the wound, and protrusion of the cells at the wound margin [23]. Hutson et al. found that dorsal closure – a phase in *D. melanogaster* embryonic development was also driven by the contraction of supracellular actin filaments [44]. These parallel results further strengthen the case for the study of wound healing as analogous to morphogenesis. It has also been shown that if the actin filaments are damaged, a new set are constructed in the remaining cells and dorsal closure (or wound healing) will proceed to completion [70].

During these studies, it was noted that adhesion was not a significant force in dorsal closure until the latest stages, further supporting the DITH: that cellular self-rearrangement is driven by differential *tensions* along cell-cell interfaces [44]. Sub-cellular ablation has shown that the behaviour of the amniosera of the *D. melanogaster* behaved somewhere "between... a continuous sheet and a 2D cellular foam (a network of tensile interfaces)" [58]. It was noted that tensions were carried predominantly in the cell-cell interfaces, but also in the apical actin structures [45, 58].

Dissections and ablation are, of course, invasive methods. Another method of exploring stresses in live tissue involves the analysis of membrane angles. One assumes that all mechanical forces which determine cell shape are balanced by tensions oriented along the membranes and acting in the immediate neighbourhood of the membranes. The neighbourhood then includes the plasma membrane itself and the apical bundle and cortical actin layer. One also assumes that the network of such tensions is in equilibrium at all times [4].

This method has been used by many researchers to generate a histogram of membrane angles; any particular modality in the histogram suggests a principle direction of stress in the tissue [4, 35, 45, 65, 79, 81]. The wide acceptance of this

approach shows that 2D methods are an acceptable avenue of analysis of tissue mechanics [4]. As embryonic tissues are largely composed of planar aggrerates, 2D methods are more than adequate [8].

Prior to this study, no one has been able to use membrane angle analysis to attribute a specific tension to each membrane – and neighbouring cytoskeletal structures – in a particular patch of cells. To develop such a method is the primary aim of this study.

2.1.4 Modelling

As the understanding of cellular mechanics advanced, several models for the mechanical behaviour of cells were developed. Continuum models of whole tissues have been developed but they are not relevant to the current study. They are therefore omitted from this discussion.

As a natural response to the experimental investigation into the structural elements of the cell, found in §2.1.2, several models of the mechanical behaviour of individual cells were developed. Various 1D equivalent mechanical circuits for the biomechanical behaviour of cells were proposed. These included Maxwell bodies, Kelvin bodies, a Kelvin body with an additional viscous damper in series, and many others [28]. These models are collectively called 'lumped parameter viscoelastic' models. Each equivalent circuit describes the behaviour of a single, isolated cell. These elements are later used to construct models of multicellular aggregates and tissues.

Another type of model seeks to describe the behaviour of the cytoskeleton in greater detail. As a purely philosophical exercise, these model the cytoskeleton as belonging to a class of structures called *tensegrity* structures. They consist of isolated compression elements connected by a network of tension elements [28]. The tension elements must be under load to maintain the integrity of the structure as a whole – hence the name. These models are a subject of very active investigation [18, 47, 46, 74, 75]

We move now to models which describe multicellular aggregates and tissues. Cellular automata – also known as lattice models – have been employed to attempt to describe cell sorting [19]. Similar models had been previously used to describe the behaviour of immiscible fluids, and given the work by Steinberg et al. [77, 78, 79] their application to morphogenetic processes seems almost inevitable. Longo et al. developed a cellular automata model to investigate blastocoel roof thinning curing epiboly based on the DAH, and validated it against experimental times to complete gastrulation. The model was able to predict dispersion of cells implanted to the blastocoel roof [57]. Cellular automata models have also been developed by Glazier and Graner, using multiple sites in the lattice to represent each biological cell [33]. These models are all computationally cheap, allowing the simulation of large patches of cells, as many as 1000 cells in some cases [85].

It is widely thought that the first computational model of cell self-rearrangement driven entirely by mechanical processes was developed by Odell et al. in 1981 [4, 19, 65]. Odell proposed that invagination processes, such as gastrulation of sea urchin eggs, neurulation in vertebrates, and ventral folding in *D. melanogaster* could all be the result of forces generated by active actin microfilaments contracting, and the resulting stress patterns such deformations generated [65].

The model consisted of a 2D ring of quadrilateral 'cells', each composed of a truss-like structure of passive viscoelastic elements to represent the cytoskeleton, an active actin element at the apical end of the cell to represent the apical microfilament bundle, and an internal cellular pressure. This active element would contract – or fire – given a certain state of strain. The model showed that to initiate invagination, the apical bundle of one cell must fire, constricting the apical surface of the cell. Odell likened the process to drawing a purse-string. Because the cells maintain a constant volume, apical constriction necessitates that the cells also elongate. The constriction of the apical surface of this one cell caused extension in the neighbouring cells; past a certain threshold of extension, the purse-strings in those cells would also fire, and the contraction propagates along the embryo until a state of mechanical equilibrium is reached, and invagination is complete [65]. It has been suggested that the initial activation of the process could be triggered by low cellular pressure [19].

Odell's work has formed the basis for a huge class of mechanically driven tissue models. Many continuum, finite element (FE), and other models have been developed. Some even go so far as to describe tip and whorl formation such as in fingerprints [19, 35]!

Davidson et al. developed a FE model to determine which of five hypothesised mechanisms was responsible for sea urchin invagination, specifically gastrulation. From these models, they found that different mechanical properties for the epithelial sheet were necessary for gastrulation to complete with each mechanism. Also, specific shape changes to arrive at the final configuration were predicted with each mechanism [24]. Davidson proposed a series of experiments to test which hypothesised mechanism was actually occurring; those experiments resulted in a set of physically plausible gastrulation mechanisms [25].

Numerical models frequently accompany the laser ablation studies detailed in §2.1.3. Sometimes, the observations from ablations can be used to validate or refine existing FE models [45]. Other times, new models are developed, which can predict the results from further experimentation [44].

As recently as 2006, the first cell-based constitutive model for embryonic tissue relating in-plane stresses, tissue deformations, topological evolution of cellular fabric, mitosis and cell rearrangement was developed. This work relied heavily on finite element modelling to supplement the available experimental data [8].

2D and 3D cell based finite element models have been developed by Brodland et al. based on the DITH [10, 9, 11, 12, 14, 87]. That model is used as the basis for the current study; it is discussed at length in §2.2.

There are continuum models of cells and cytoskeletal networks have been developed [51, 71]. There are also models based on Steinberg's DAH, and investigating more precisely the nature of cell-cell adhesions, which do agree with the Steinberg's experiments [52, 67]. Since the current study does not make use of this model, they are not discussed further, and are included here for completeness only.

Clearly, it can be said that neither modelling nor experimentation alone can be relied upon to unlock the secrets of cell self-rearrangement. Experimentation is necessary to support modelling, and, as Harris said, "[w]ithout something of that kind [modelling], we won't know what other sorts of behavior [sic] to look for, nor whether our list is already adequate to predict (and thereby explain) the formation of anatomical patterns... [D]evelopmental biology will remain a prisoner of our inadequate and conflicting physical intuitions and metaphors." [38].

2.2 The Finite Element Model

A finite element (FE) model has been developed to simulate displacements in biological cells. The 2D implementation of the model, called *Simba*, is used as a foundation on which the new model *Scar* was built. *Simba* provides a system to mathematically describe the geometry of patches of cells over time, and some relationships between displacements and forces in these patches. Implicit in the model are several assumptions about the behaviour of these patches of cells, which are necessary to develop the model.

The FE model is a forward simulation. A starting geometry is input or generated. Various mechanical properties, applied forces, and constraints are specified. The model then calculates an increment of displacement, updates the geometry, and continues for the prescribed number of time steps.

2.2.1 Nodes, Edges, and Elements

The basic constructs of the FE model are nodes, edges, and elements. These structures mathematically define the geometry and topology of the cell patch.

Nodes

Nodes are points in space that correspond to triple junctions in the cell patch. A triple junction is where three cell membranes meet. It is at each node that equilibrium must be strictly satisfied. In the 2D case, each node can displace in either the x- or y-direction; displacements in the z-direction are held to zero. Alternatively, each node can be said to have two degrees of freedom (DOF). Therefore two equations of equilibrium can be written at each node.

It is assumed that no more than three membranes ever meet at one location. The restriction is imposed for calculation reasons. There is one physical situation where,

for an instant, four membranes will meet at one single node: a neighbour change between two cells, shown below in Figure 2.3. A neighbour change occurs when one cell slides past another. The portion of membrane between cells B and D shortens, drawing cells A and C closer and closer together. For an instant, when nodes 1 and 2 meet, all four cells share one node and the membrane between nodes 1 and 2 can be said to have zero length. This moment is shown in configuration b). This must happen, but computationally we instantaneously change from configuration a) to configuration c). This imposed change to the topology of the patch occurs when the length of a membrane is less than some critical value, l_{crit}. After the neighbour change, the length of that edge is set to be longer than l_{crit} to prevent another neighbour change on the following time step. Such an artificial change is necessary as short edges artificially stiffen the model, a phenomenon known as shear locking [11].

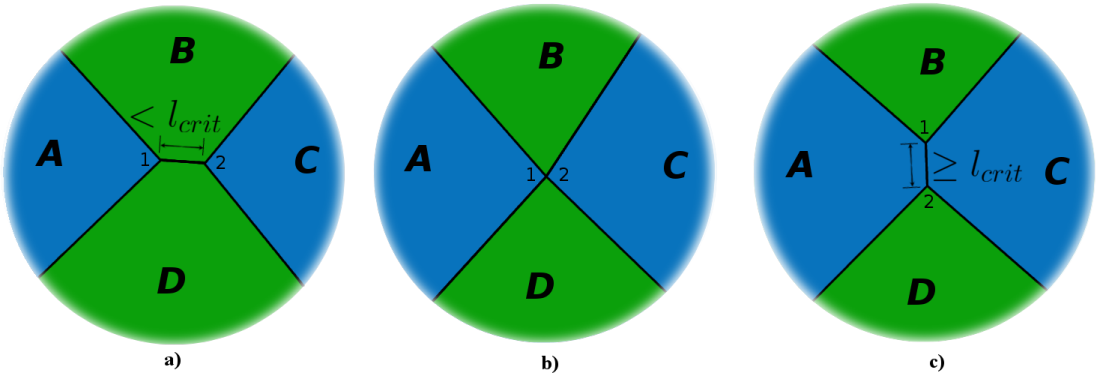

Figure 2.3: Neighbour change morphology

It is possible for a node to connect to only two membrane segments. This can occur along the boundary of a patch to capture the convexity of a cell in contact with the medium. A node connecting only two membranes is not permitted on the interior of a patch, that is, on an interface between two cells. Physically, a pressure difference between two adjacent cells curves the membrane between them such that is is convex to the cell with higher pressure. This of course produces a different insertion angle of the membrane at the node that does a straight line between two nodes. While a mid-side node could more accurately model the insertion angle of such a curved membrane, the effect is considered negligible, and mid-side nodes are not permitted. These legal and illegal configurations are shown in Figure 2.4.

Edges

An edge is the programming construct which models the cellular membrane, and the forces acting along it. Edges are straight line segments between two nodes.

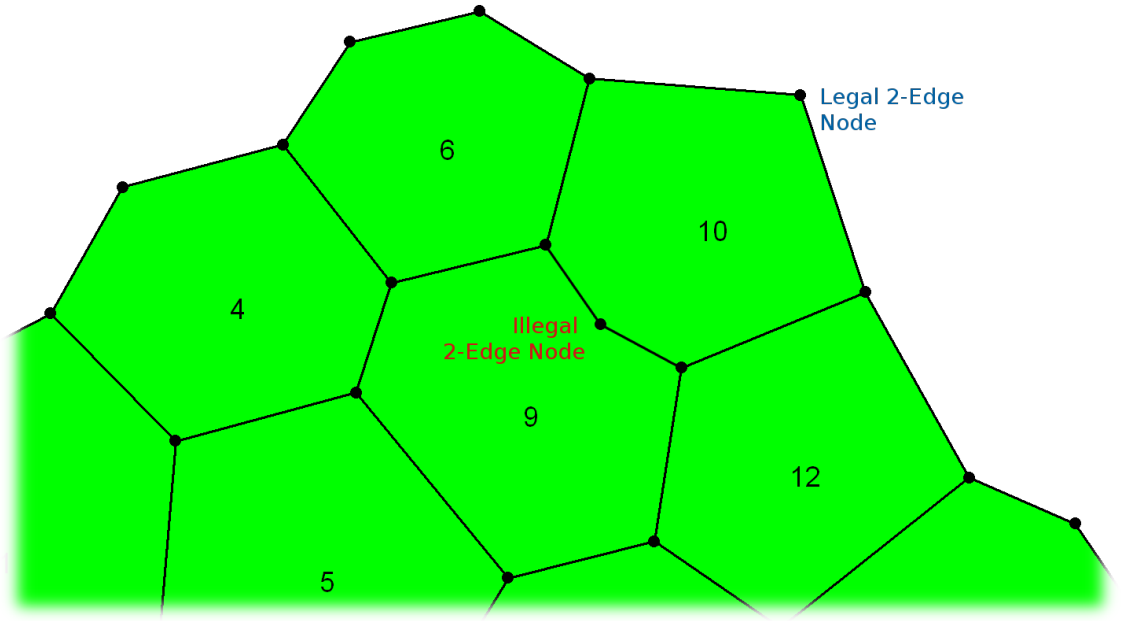

Figure 2.4: Legal and illegal configurations for a node connecting only two edges

The edge models the interface between two cells, or between a cell and the medium. Each edge has a tension specified, dependant on the nature of the interface. The user will specify a certain tension along a cell-medium interface, another between like cells, and if desired, yet another between cells of different types. The specified tension γ_{AB} aggregates a number of intra-cellular forces, shown schematically below in Figure 2.5. The forces form each structure are superposed according to Eq. (2.4)[9].

$$\gamma_{AB} = F_A^{Cyto} + F_B^{Cyto} + F_A^{Mem} + F_B^{Mem} - F_{AB}^{Adh} + F_{AB}^{Other} \tag{2.4}$$

The term F_A^{Cyto} includes forces oriented along the membrane from the cytoplasm, apical microtubules, and intermediate filaments (IFs) of cell A. The term F_B^{Mem} include the tension in the membrane itself, and also tensions in the cortical actin layer (CAL) which is located on the cortical surface of cell B. The term F_{AB}^{Adh} includes the adhesion force between cells A and B generated by the cell adhesion molecules (CAM). This adhesion force actually lowers the tension along the interface which is why this term is subtracted from the total in Eq. (2.4). Finally, the term F_{AB}^{Other} accounts for any other contractile forces along the interface between the two cells. The biological function of these structures, and further details of their composition can be found in §2.1.1 and §2.1.2.

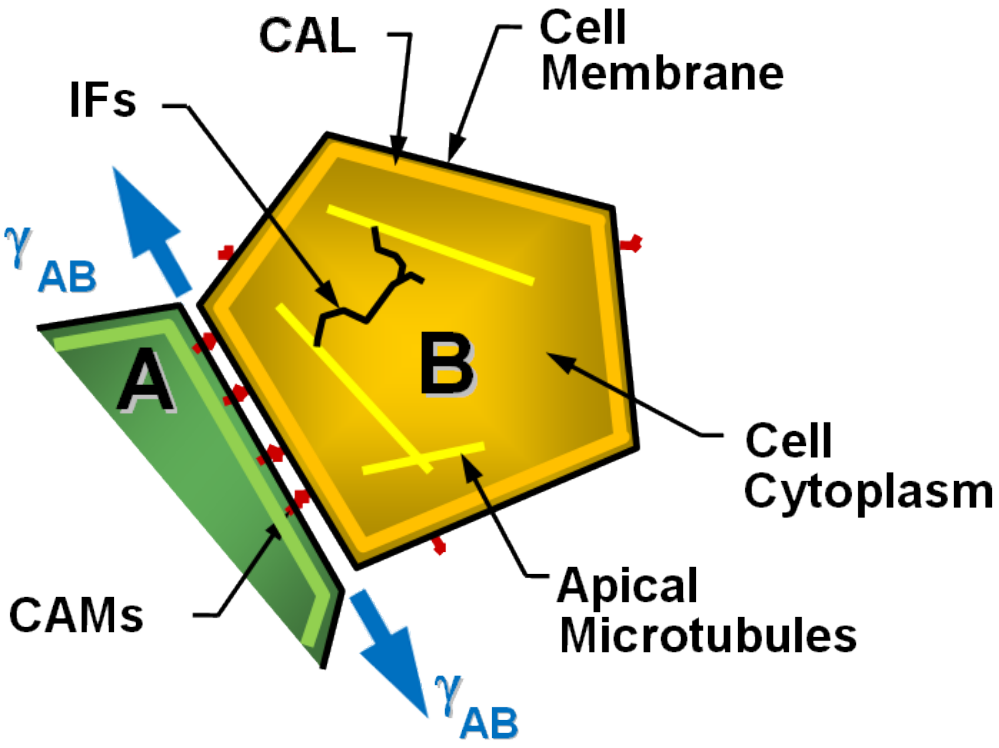

Figure 2.5: Contributions to the force along a cell interface

Elements

There are several classes of element available in the FE model. In addition to the familiar structural elements such as the truss and the beam, a customised element was developed for *Simba* to model biological cells. The Cell2D element is defined by a collection of edges, by which the Cell2D element inherits a collection of nodes.

It has been shown that biological cells undergo strain rates on the order of 10^{-6}/s during tissue remodelling processes such as sorting and embryogenesis. At this low rate, the mechanical behaviour of cell contents - cytoplasm and organelles - can be modelled as a massless, viscous, incompressible fluid [14]. Wound healing responses have been shown to have strain rates several orders of magnitude higher than normal tissue remodelling [45]. This fact has the potential to cause problems with a viscous-only model of cytoplasm mechanics, and will be discussed further in Chapter 4. The Cell2D element models the viscous cell contents as a system of orthogonal dashpots, shown in Figure 2.6. The orthogonal dashpots are oriented along the major and minor axes of the equivalent elliptical region. The dashpots are each connected to one node, and to a common ground. The figure shows the dashpots only in the major axis direction for clarity.

The stiffness of each dashpot is calculated according to Eq. (2.5)[11].

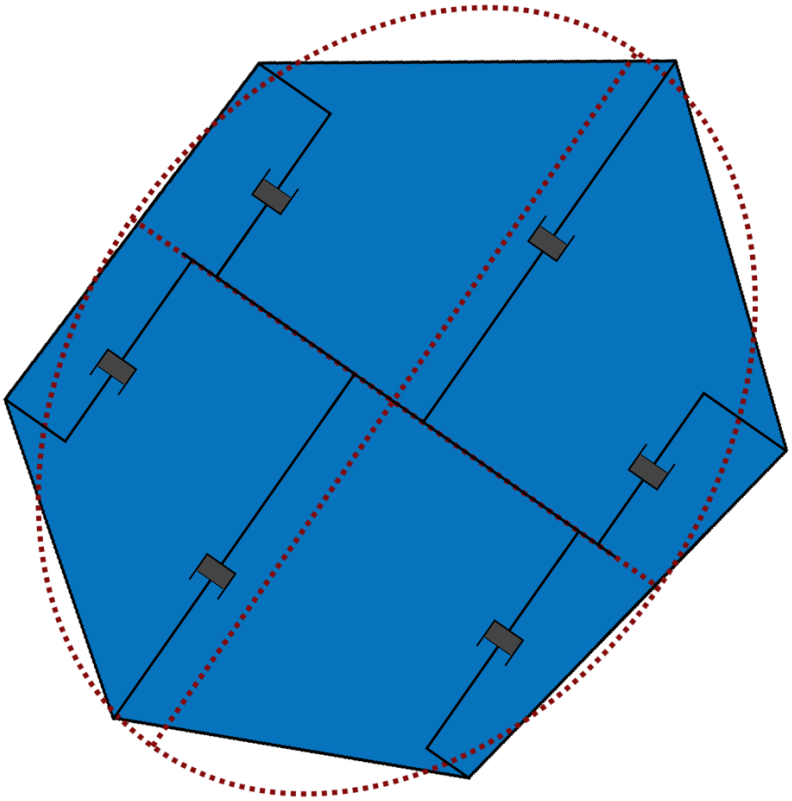

Figure 2.6: Dashpot model for viscosity of cell contents

$$\mu_A = \frac{4g\pi\mu hB}{nA} \tag{2.5}$$

In Eq. (2.5), g is a form factor equal to 0.682, μ is the specified cell viscosity, n is the number of nodes which comprise the cell, h is the cell thickness, and A and B are the major and minor axes of the cell, respectively. The γ–μ model was discussed at length in §2.1.

2.2.2 Supports and Constraints

The model allows the user to specify various constraints on the degrees of freedom. These include displacement, velocity, and force or stress constraints. The forces which arise from these constraints on the FE model will be of great importance to this study in Chapter 3.

It is assumed that the cell contents are incompressible. As such, throughout any motion, the volume of each cell is constant. It has been shown that planar

sheets of cells conserve area throughout motions [65, 45]. This means that for a two dimensional model, the area of each cell is constant, and so is the thickness of the planar sheet.

All the constraints on the model are imposed as Lagrange side conditions to the equations of motion. The resulting Lagrange multipliers and their meanings are discussed in §2.2.3.

2.2.3 Solution of the FE Model

The general equations of motion are given in Eq. (2.6). For the specific case of biological cells, the scale is so small that inertial forces can be ignored. As such, the second order terms can be ignored, reducing the system to a first order system of equations. As discussed above in §2.2.1, elastic forces can also be ignored, leaving only viscous or first order terms in displacement. These two statements are equivalent to saying that $\mathbf{f}_m = \mathbf{f}_k = 0$, and that $\mathbf{f}_c = \mathbf{F}$. The reduced equations of motion are then divided by the increment of time to solve directly for the nodal displacements, as given by Eq. (2.7).

$$\mathbf{M\ddot{u}} + \mathbf{C\dot{u}} + \mathbf{Ku} = \mathbf{f}_m + \mathbf{f}_c + \mathbf{f}_k = \mathbf{F} \tag{2.6}$$

$$\mathbf{C}\left(\frac{1}{\Delta t}\mathbf{u}\right) = \mathbf{F} \tag{2.7}$$

The system is geometrically nonlinear. The equations of motion, Eq. (2.7), augmented with the constraints as discussed in §2.2.2, are solved for one interval of time. The resulting solution vector is composed of the nodal displacements and the Lagrange multipliers associated with the constraints for that time step. It bears repeating the the ultimate output of the model *Simba* is a *time history* of nodal displacements and reactions.

The Lagrange multipliers for constrained degrees of freedom (DOF) such as nodal displacement or velocity constraints are the reaction forces at those DOF. These are the forces required to maintain equilibrium of the patch at each node. The Lagrange multipliers for the volume constraints on each cell correspond to the internal pressure required for that cell to maintain its volume.

The internal cell pressure is very important to this study. Though it arises as a reaction force in the FE model, it represents one half of a force balance present in living cells; the membrane tensions and cell pressures are at all times in dynamic equilibrium with the viscous resistance of the cell contents. It will be necessary for the current model to incorporate both tensions and pressures to achieve a complete set of forces at work for any motion being studied. The complete FE model is shown schematically in Figure 2.7.

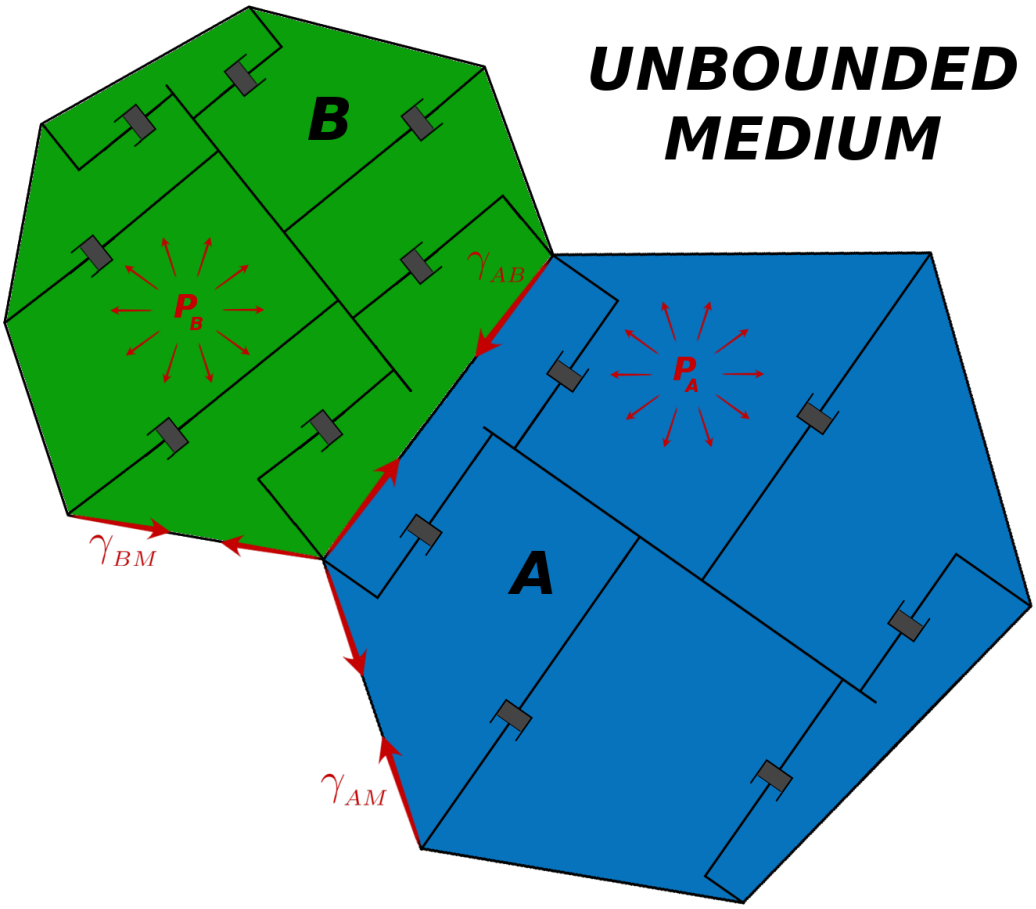

Figure 2.7: The finite element, differential tension model

2.3 Parameter Estimation

Parameter estimation is a topic within the field of system identification. In simplest terms, parameter estimation is a class of algorithms which seek approximations to certain parameters governing the behaviour of a dynamical system. These approximations – or estimates – are made using some combination of observations of the output from a dynamical system, some knowledge of the inputs to the system, and assumptions about the nature of the system. A number of basic methods exist to arrive at these estimates, and the variations on these methods are practically innumerable.

The oldest and simplest method for estimating the parameters relating a number of observed outputs to a number of inputs is a least-squares (LS) solution. The method was first developed by Carl Friedrich Gauss and was used to estimate orbits

of celestial bodies based on a few observations of position over time [31, 32]. When a relatively large number of observations are available, Laplace later showed that the LS method is the preferred approach, regardless of the distribution of the errors in those observations [31]. A modern mathematical description of the method is given below in Eq. (2.8) through Eq. (2.13), and was adapted from [27], [62], and [63].

Supposing a set of observations of input (u_k) and output (y_k) data to a system, which is assumed to have the form

$$y_k = -a_1 y_{k-1} - a_2 y_{k-2} + a_3 u_k + a_4 u_{k-1} \tag{2.8}$$

The parameters to be estimated are the coefficients a_1 through a_4. These are represented in the form of a parameter vector $\mathbf{p}^T = [a_1 \ a_3 \ a_3 \ a_4]$. We also define the information (previous output and current and previous input) vector at time step k as $\mathbf{h_k} = [y_{k-1} \ y_{k-2} \ u_k \ u_{k-1}]$. Assuming that $\mathbf{p}$ is constant over time, then the output at any time k is given by

$$y_k = \mathbf{h}_k \mathbf{p}. \tag{2.9}$$

Or, in matrix form, where each $\mathbf{h_k}$ is a row of $\mathbf{H}$, the entire history of the system is written as shown below. Note that the meaning of the sign $\simeq$ has yet to be defined, but is necessary to be strictly correct [63].

$$\mathbf{y} \simeq \mathbf{H}\mathbf{p} \tag{2.10}$$

If the system of equations in Eq. (2.10) is overdetermined – that is, there are more observations collected than unknown parameters – it is unlikely that a unique set of parameters will satisfy all the equations in the system. This is especially true if the information has been corrupted by measurement error or other noise. In this case, any set of *estimated* parameters $\hat{\mathbf{p}}$ will not exactly satisfy the system of equations, but will leave some residual, $\mathbf{r}$ defined as:

$$\mathbf{r} = \mathbf{y} - \mathbf{H}\hat{\mathbf{p}} \tag{2.11}$$

The essence of a LS solution then is to minimise the square root of the sum of the squares of the residual, also called the Euclidean norm of the residual, defined according to:

$$\|\mathbf{r}\|_E = \sqrt{\mathbf{r}^T \mathbf{r}} \tag{2.12}$$

This then is the objective function. It can be shown by simple evaluation of the partial derivative $\frac{\partial \|\mathbf{r}\|_E}{\partial \hat{\mathbf{p}}} = 0$ that the solution $\hat{\mathbf{p}}$ to the system

$$\mathbf{H}^T\mathbf{H}\hat{\mathbf{p}} = \mathbf{H}^T\mathbf{y} \tag{2.13}$$

is the solution which minimises the norm of the residual, and is the so-called LS solution to the overconditioned system Eq. (2.10). Eq. (2.13) is simply a set of n linear equations in n unknowns, and is called the set of *normal equations* for the original system. Simple inversion of the matrix product $\mathbf{H}^T\mathbf{H}$ and pre-multiplying on both sides will yield a solution for $\hat{\mathbf{p}}$. This approach can result in numerical stability issues arising out of the special structure of the product $\mathbf{H}^T\mathbf{H}$[63]. Fortunately, there exist a number of more sophisticated methods to arrive at the LS solution to a system of equations, such as the QR- and Singular Value decompositions. Development of these methods and their applications to LS solutions is left to specialised texts [26, 39, 63].

Another description of the LS solution is shown in Eq. (2.14) and Eq. (2.15), as presented in [27] and [62]. This representation makes use of an intermediate step in the procedure, which will prove useful later. We begin by defining two matrices, $\mathbf{P}_k$ and $\mathbf{B}_k$. In these definitions, $\mathbf{H}_k$ is the first k rows of the full matrix $\mathbf{H}$.

$$\begin{gathered}\mathbf{P}_k = (\mathbf{H}_k^T\mathbf{H}_k)^{-1} \qquad \textit{and} \qquad \mathbf{B}_k = \mathbf{H}_k^T\mathbf{y}_k \\ \textit{or} \\ \mathbf{P}_k = \left\{\sum_{i=1}^{k}\mathbf{h}_i^T\mathbf{h}_i\right\}^{-1} \quad \textit{and} \quad \mathbf{B}_k = \sum_{i=1}^{k}\mathbf{h}_i^T y_i\end{gathered} \tag{2.14}$$

The solution to the LS problem after k observations is now the matrix product:

$$\hat{\mathbf{p}}_k = \mathbf{P}_k\mathbf{B}_k \tag{2.15}$$

In this sense the LS algorithm is a batch estimator [27]. With the addition of each new batch of observations, the matrix inversion in $\mathbf{P}_k$ must be recalculated. This approach is expensive in terms of both computation and memory. It would be far preferable if the matrices $\mathbf{P_k}$ and $\mathbf{B_k}$, as well as the estimate $\hat{\mathbf{p}}$ could be updated as new information becomes available. The derivation of such a recursive least-squares (RLS) solution is quite lengthy, and is left to specialised texts [27, 43]. Assuming the parameters being estimated remain constant for a time which is sufficiently longer than the sampling interval, the resulting update laws for RLS are:

$$\begin{aligned}\mathbf{P}_k &= \mathbf{P}_{k-1} - \frac{\mathbf{P}_{k-1}\mathbf{h}_k^T\mathbf{h}_k\mathbf{P}_{k-1}}{1+\mathbf{h}_k\mathbf{P}_{k-1}\mathbf{h}_k^T} \\ \hat{\mathbf{p}}_k &= \hat{\mathbf{p}}_{k-1} + \frac{\mathbf{P}_{k-1}\mathbf{h}_k^T(y_k - \mathbf{h}_k\hat{\mathbf{p}}_{k-1})}{1+\mathbf{h}_k\mathbf{P}_{k-1}\mathbf{h}_k^T}\end{aligned} \tag{2.16}$$

The matrix $\mathbf{P}_k$ in Eq. (2.15) and Eq. (2.16) is more than just a convenient representation of terms in the LS formulation; it is related to the covariance matrix $\mathbf{\Sigma}$ by a constant [59]. For n parameters:

$$\mathbf{P}_k = \frac{1}{s_e^2}\mathbf{\Sigma} = \frac{1}{s_e^2}\begin{bmatrix} \widehat{var}(\hat{p}_0) & \widehat{cov}(\hat{p}_0,\hat{p}_1) & \dots & \widehat{cov}(\hat{p}_0,\hat{p}_n) \\ \widehat{cov}(\hat{p}_1,\hat{p}_0) & \widehat{var}(\hat{p}_1) & & \\ \vdots & & \ddots & \\ \widehat{cov}(\hat{p}_n,\hat{p}_0) & & & \widehat{var}(\hat{p}_n) \end{bmatrix} \tag{2.17}$$

This means that the diagonal of the matrix $\mathbf{P}_k$ contains information regarding the variance of the estimate of each parameter. High values on the diagonal of $\mathbf{P}_k$ imply large variance in the estimates of those parameters. Furthermore, the off-diagonal terms contain information relating to the covariance of the parameters being sought. The constant s_e^2 is an estimate of the variance, σ^2, of the residual [59]. This results allows us to assess – or at least compare – the accuracy of the estimates. Other statistical quantities can be derived from terms in the above formulation, but these are not relevant to the current study; the curious reader is referred to the extensive literature on the subject [3, 27, 43].

The recursive formulation presented in Eq. (2.16) provides an updated estimate of the parameters each time new information becomes available. One should therefore be able to adapt this algorithm to estimate parameters which vary over time. If in the formulation the newer information is given some precedence over the older, the output should track changes in the parameters. This can be accomplished by introducing an exponentially decaying weight to the objective function [27]. Recall Eq. (2.12). Substituting Eq. (2.11) and adding an exponentially decaying weight, with some algebraic manipulation, the cost function becomes:

$$J' = \sum_{i=1}^{k} \lambda^{k-i}(\mathbf{h}_i\hat{\mathbf{p}}_k - y_i)^2 \tag{2.18}$$

The cost function J' is presented in terms of a summation rather than the vector notation previously used for clarity of the inclusion of the weighting factor λ. This coefficient is called a *forgetting factor*, and has a range $0 < \lambda \leqslant 1$. Following a similar derivation to that used for the RLS formulation in Eq. (2.16), we find the following update laws for the RLS with forgetting factors (RLS-FF) [27]:

$$\mathbf{P}_k = \frac{\mathbf{P}_{k-1}}{\lambda} - \frac{(1-\lambda)}{\lambda^2}\frac{\mathbf{P}_{k-1}\mathbf{h}_k^T\mathbf{h_k}\mathbf{P}_{k-1}}{\left(1+\frac{1-\lambda}{\lambda}\mathbf{h}_k\mathbf{P}_{k-1}\mathbf{h}_k^T\right)} \tag{2.19}$$

$$\hat{\mathbf{p}}_k = \hat{\mathbf{p}}_{k-1} - (1-\lambda)\mathbf{P}_k(\mathbf{h}_k^T\mathbf{h}_k\hat{\mathbf{p}}_{k-1} - \mathbf{h}_k^T y_k)$$

The forgetting factor λ can be said to define the length of the algorithm's memory. Values of λ close to unity mean that old information is 'forgotten' very slowly; values close to zero mean that old information is forgotten more quickly. In this sense, λ would be more accurately called a 'remembering factor'. Some texts make the substitution $\alpha = 1-\lambda$ when constructing the cost function Eq. (2.18)[27] . The constant α can more appropriately be called a forgetting factor since higher values correspond to faster forgetting. The majority of the literature, however, uses λ, as does this study [16, 17, 29, 56, 48, 66, 72, 73]

The selection of an appropriate forgetting factor is somewhat of a compromise. Lower values of λ forget quickly. As such, the estimate will adapt to changing parameters and is said to have good tracking. A forgetting factor close to unity will be less susceptible to noise corruption (misadjustment) and will be more stable, but will track more slowly [66]. Another problem with forgetting factors arises as the system reaches a steady state. In that case, the update law for $\mathbf{P}_k$ reduces to $\mathbf{P}_k \rightarrow \frac{1}{\lambda}\mathbf{P}_{k-1}$. Since $\lambda < 1$, $\mathbf{P}_k$ can tend to increase exponentially or "blow-up"[27]. A solution to all these issues can be found in a variable forgetting factor.

The recursive least-squares with variable forgetting factors (RLS-VFF) was first proposed by Fortescue. His method is based on a scaling of the prediction error in an RLS formulation which more closely resembles the Kalman filter [29].

Since this seminal work, a number of other formulations for varying the forgetting factor have been published. So et al. propose a method based on the gradients of the parameter estimates [72]. Leung and So later proposed another gradient based method where the gradient is derived from a new mean square error analysis of the RLS algorithm [56]. Cooper and Worden present a similar method based on exponentials scaled using a normalised gradient of the parameter estimates [16]. That piece is noteworthy in its focus on applications to structures and dynamic structural system identification. Paleologu et al. introduce a method which depends on recovering the corrupting noise in the error signal and noise power estimates [66]. Song et al. derived a method which uses a Gauss-Newton approach incorporating second derivatives of the cost function. This method improves tracking of quickly varying parameters without sacrificing noise immunity and stability [73].

Each method has its own particular strengths, limitations, and appropriate uses. Selection of a RLS-VFF scheme is often a process of trial and error, trying the various methods and selecting the one which is most suited to the application at hand. For more details and methods, the reader is directed to [16, 56, 66, 72, 73, 88, 89] and the references therein.

The above discussion was completed for the single input, single output (SISO) system. For this study, there are multiple inputs (the displacement of each node in each direction) and multiple unknown forces. Such a system is called a multiple input, multiple output (MIMO) system, and andjustments to the LS and RLS formulations are required to cope with the increased order of the problem. Instead of the scalar SISO system from Eq. (2.9), the MIMO system is written at each step as

$$\mathbf{y}_k = \mathbf{h}_k^* \mathbf{p}. \tag{2.20}$$

where $\mathbf{y}_k$ is now a vector of system outputs, and $\mathbf{h}_k^*$ is a matrix of previous outputs and previous and current inputs. Eq. (2.10) remains unchanged in notation, but the matrix $\mathbf{H}$ now contains submatrices $\mathbf{h}_k^*$ for each timestep, rather than the vectors $\mathbf{h}_k$ as each row. The LS formulation remains the same for Eq. (2.11) through Eq. (2.13).

The intermediate matrices $\mathbf{P}_k$ and $\mathbf{B}_k$ for the MIMO system are now

$$\mathbf{P}_k = \left\{ \sum_{i=1}^{k} \mathbf{h}_i^{*^T} \mathbf{h}_i^* \right\}^{-1} \quad and \quad \mathbf{B}_k = \sum_{i=1}^{k} \mathbf{h}_i^{*^T} \mathbf{y}_i \tag{2.21}$$

with the matrix notation remaining unchanged. Finally, the RLS update laws for the MIMO system become

$$\begin{aligned} \mathbf{P}_k &= \frac{\mathbf{P}_{k-1}}{\lambda} - \frac{(1-\lambda)}{\lambda^2} \mathbf{P}_{k-1} \mathbf{h}_k^{*^T} \mathbf{h}_k^* \mathbf{P}_{k-1} \left(\mathbf{I} + \frac{1-\lambda}{\lambda} \mathbf{h}_k^* \mathbf{P}_{k-1} \mathbf{h}_k^{*^T} \right)^{-1} \\ \hat{\mathbf{p}}_k &= \hat{\mathbf{p}}_{k-1} - (1-\lambda) \mathbf{P}_k (\mathbf{h}_k^{*^T} \mathbf{h}_k^* \hat{\mathbf{p}}_{k-1} - \mathbf{h}_k^{*^T} \mathbf{y}_k) \end{aligned} \tag{2.22}$$

where $\mathbf{I}$ denotes the identity matrix.

Chapter 3

Scar: The Identification Algorithm

With the FE model from §2.2 as a foundation, a new method was developed to estimate forces which drive deformations in patches biological cells. Drawing on system identification techniques from §2.3, This new method is referred to as the *identification algorithm*, or colloquially as 'Scar'. This chapter will develop the algorithm's various elements model. At each step, we demonstrate the performance using a single input patch of synthetic data, kept consistent throughout the chapter. Such output is meant to be purely demonstrative; rigorous detailed discussion of results is left to Chapter 4.

3.1 Inverting the FE Model

The existing FE model *Simba* was discussed at length in §2.2, and is used as the foundation of the current study. The inputs to this new model will be the displacement history which was the output of the forward model. Note that while the FE model can output data such as cell pressures and support reactions, both of which would be useful to the current study, the inputs are restricted to the displacement history only, even when using synthetic data, since that information will not be available when live data are employed.

The first step is to use existing code libraries to assemble the damping matrix from the FE model. Eq. (2.7) was solved for nodal displacements subject to the applied constraints in the forward model. For the new algorithm, the displacement history is available, and so Eq. (2.7) is used instead to calculate forces at the nodes which arise from viscous resistance of the cell contents to the observed displacements.

As was hinted at before, this expression of nodal force includes only viscous forces; it does not include any concentrated forces at the nodes from support reactions or any other forces on the cell patch. During this early stage of algorithm

development, the synthetic data used have been constructed such that this assumption holds. This was achieved by ensuring that the patch of cells is isolated in an unbounded medium, with no external forces. Also the boundary conditions were set such that one node was pinned – both degrees of freedom at the node were held to be zero – and one other node is connected to a very weak spring as shown in Figure 3.1. The spring ensures static determinacy of the patch as a free body, but has such a low stiffness as not to attract any load. This set of boundary conditions ensures that no forces other than the viscous resistance to deformation are present, with all support reactions being zero. This simple input patch will be used to demonstrate each step in the identification algorithm.

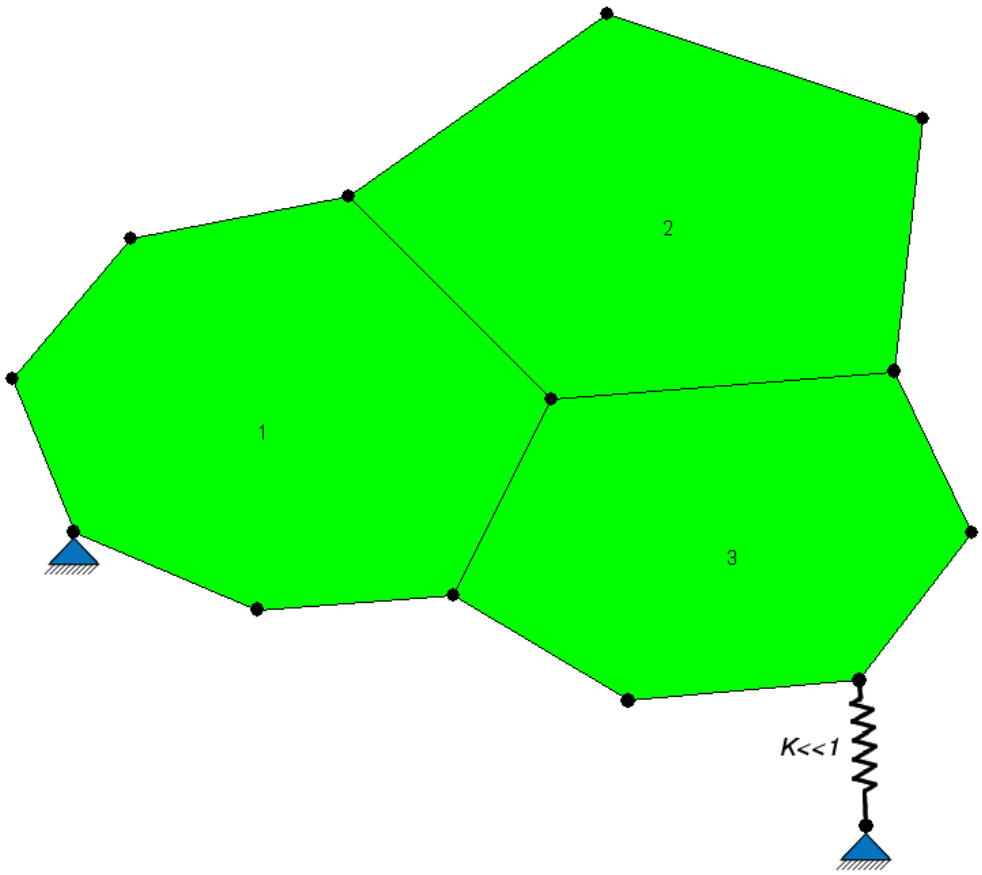

Figure 3.1: Input patch for demonstrating the elements of the identification algorithm

3.2 The Geometric Matrix

Having calculated the nodal forces, which include only the viscous forces according to Eq. (2.7), it must be determined which subcellular structures generate these forces. To this end, a set of equation dubbed the geometric matrix is developed,

which relates the nodal forces to forces in subcellular structures. These equations are written at each timestep individually, just as nodal forces were calculated at each time step individually.

3.2.1 Force Generators

Figure 3.2 shows a portion from the interior of a synthetic patch of cells. The two assumed contributions to the nodal forces are shown in this figure.

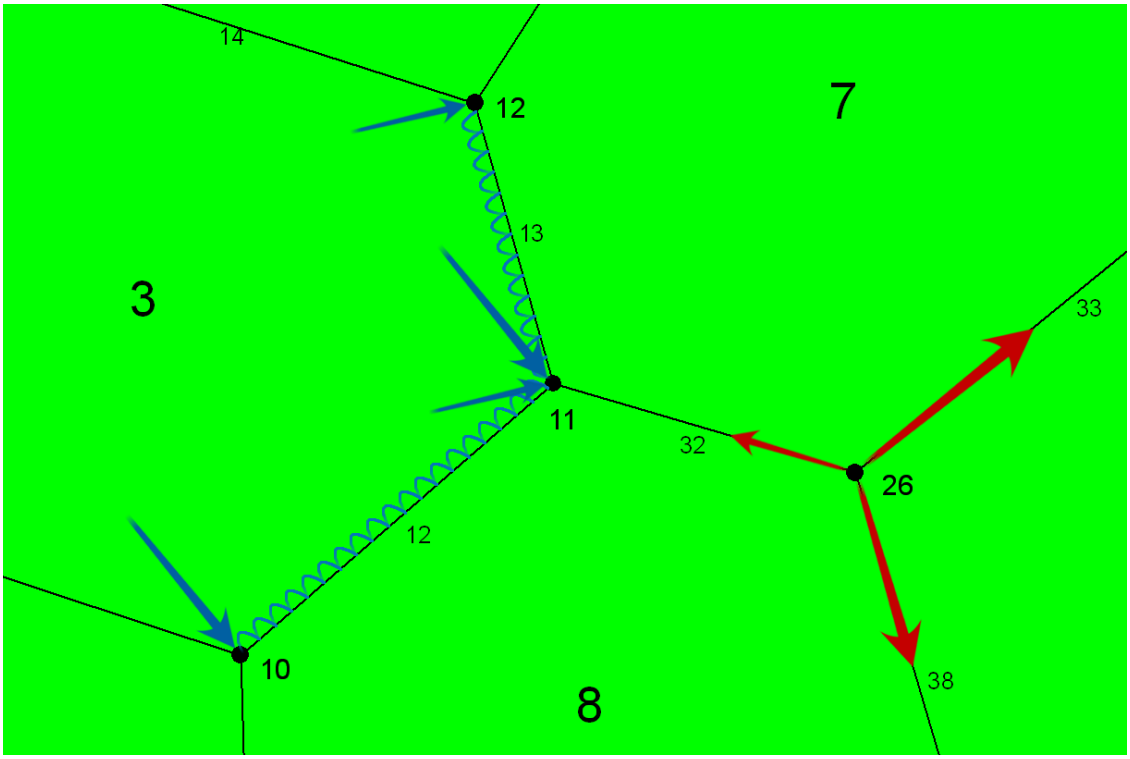

Figure 3.2: Contributions to Nodal Forces

We will first focus on Node 26. Each of the three edges which meet at this node is assumed to be in tension. Therefore, each exerts a force on Node 26 equal to the tension in that edge, and oriented along the edge itself. These forces are shown in red. The sizes of the arrows are arbitrary; as yet it is not known whether Edge 33 carries higher tension than Edge 32. It is assumed that the tensions are not necessarily equal.

A distributed load is shown in blue on Edges 12 and 13. This represents the in plane loads in cell three. Typically, this load is thought of as a pressure – and referred to henceforth as such – but represents any type of in-plane load carried by the apical and basal membranes and the contents of the cell, but not the cortical membranes. In addition to the pressure in the cytoplasm, this aggregate of forces could account for forces in the cytoskeleton or other structures within the cell. As a result, it is possible that this representation of pressure is negative, meaning

only that forces in certain structures within the cell oppose the pressure in the cytoplasm and are greater in magnitude. Negative 'pressures' arise easily form a patch in tension. As discussed in §2.1.3, embryonic tissues such as in the *D. melanogaster* are often in tension [50].

Figure 3.2 also shows concentrated loads at Nodes 10, 11, and 12. These are the resultants of the distributed pressures on the edges. The magnitude of the resultant is given by Eq. (3.1), and is simply the pressure in the cell, multiplied by half the length of the edge. The resultant forces act perpendicular to the edge in question. This representation is identical to a distributed load on a beam.

$$\|P\vec{R}\| = \frac{Pl}{2} \tag{3.1}$$

3.2.2 Assembling the Geometric Matrix

Having determined in the previous section the force generators in a patch of cells, we now have a system of equations in component form which relate the tensions and pressures to the nodal forces. All calculations are carried out in component form. This system of equations will take the form of Eq. (3.2), where $\mathbf{G}$ is the geometric matrix, $\mathbf{F}$ is a vector of nodal forces, and $\mathbf{T}$ is a vector of unknown tensions and pressure for which the equations are solved.

$$\mathbf{GT} = \mathbf{F} \tag{3.2}$$

$$[\mathbf{G}_T]\{\mathbf{T}_T\} + [\mathbf{G}_P]\{\mathbf{T}_P\} = \mathbf{F} \tag{3.3}$$

Eq. (3.2) can be seen as being composed of two sets of equations: one set relates tensions to nodal forces, and the second relates pressures. This representation is shown in Eq. (3.3), and is useful for the discussion of the assembly of the geometric matrix $\mathbf{G}$.

Tensions

The entries of $\mathbf{G}_T$ relate the tension in an edge to the force the edge exerts on a particular node. The entries are given by the components of a unit vector along the edge in question. Refer to Figure 3.3 and Eq. (3.4), where l is the length of the edge, and Δx and Δy are the x and y components of the edge, respectively.

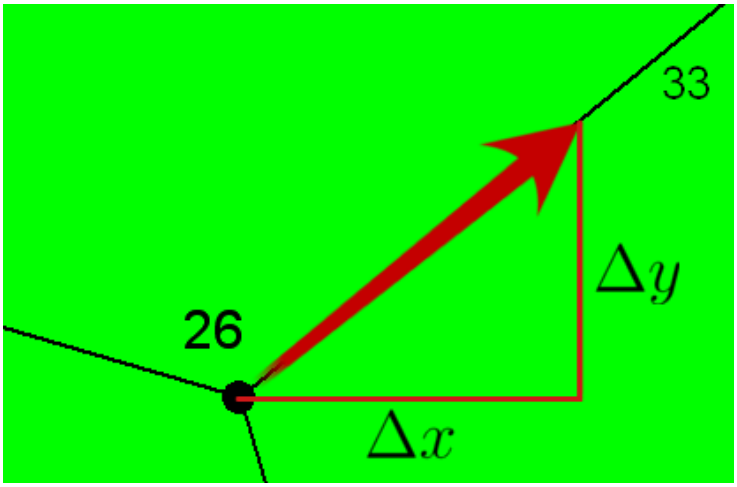

Figure 3.3: Development of tension components in the Geometric matrix, G

$$\begin{bmatrix} G_{T_{1,1}} & \cdots & & \\ \vdots & \ddots & & \\ & & G_{T_{53,33}} = \Delta x/l & \\ & & G_{T_{54,33}} = \Delta y/l & \\ & & & \ddots \end{bmatrix} \begin{Bmatrix} \vdots \\ T_{T_{33}} \\ \vdots \end{Bmatrix} = \begin{Bmatrix} \vdots \\ F_{T_{53}} \\ F_{T_{54}} \\ \vdots \end{Bmatrix} \tag{3.4}$$

In Eq. (3.4), the structure of the geometric matrix can be seen; the rows correspond to the degrees of freedom (DOF) of the model. In the example above, quantities in x and y at Node 26 are DOF 53 and 54. Entries in the 53^{rd} row of $\mathbf{G}$ are multiplied by the unknown tensions in $\mathbf{T}$, and summed, in accordance with the laws of matrix-vector multiplication. By having non-zero entries for a row in only those columns which correspond to the edge tensions which meet at that DOF, a compact notation is achieved, which relates components of force in x and y at each node to the unknown tensions in each edge.

Pressures

The entries of $\mathbf{G}_P$ relate the pressure in a cell to the forces exerted on each node in that cell. In the previous section, it was determined that the resultants of the distributed cell pressure acting on an edge are given by Eq. (3.1) and act perpendicularly outward from that edge. To determine the components of this vector in a Cartesian system, binormal vectors are employed, arranged as shown in Figure 3.4.

For the node in question, two vectors are defined. The vector $\vec{c}$ extends form the node in question to the centre of the cell. The vector $\vec{e}$ extends from the node along the edge on which pressure is acting. From here, we calculate two more vectors

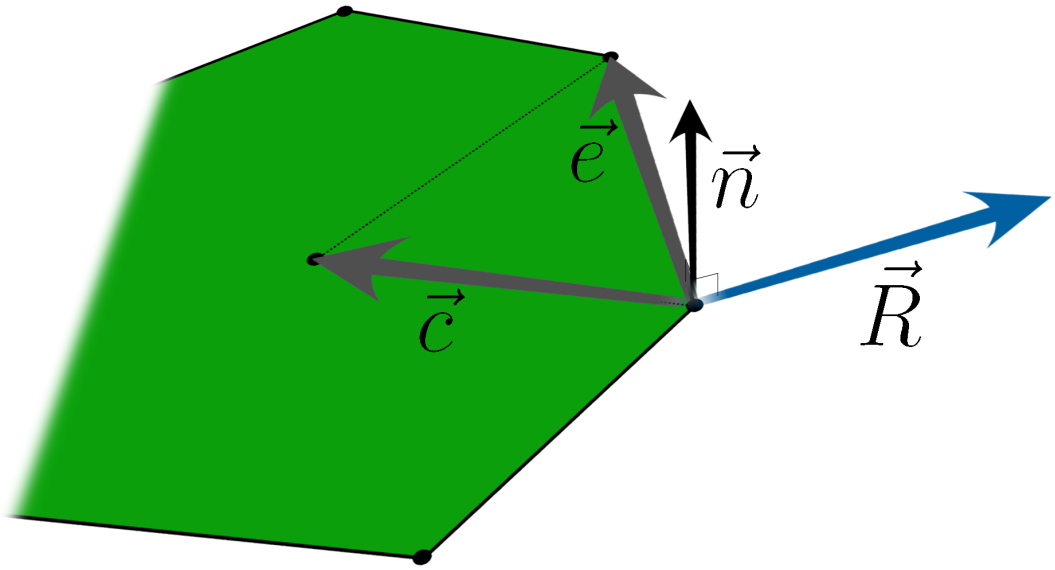

Figure 3.4: Development of pressure components in the Geometric matrix, G

according to Eq. (3.5) and Eq. (3.6). The order of the cross products ensures that $\vec{R}'$ is an outward normal to the cell's edge. $\vec{R}'$ is then scaled to give $\vec{R}$, such that when multiplied by the cell pressure, the vector $P\vec{R}$ is the resultant force on the node, as shown in Eq. (3.1). The complete formulation for $\vec{R}$ then given by Eq. (3.7), where l is the length of the edge on which the pressure acts.

$$\vec{n} = \vec{e} \times \vec{c} \tag{3.5}$$

$$\vec{R}' = \vec{e} \times \vec{n} \tag{3.6}$$

$$\vec{R} = \frac{l}{2} \frac{\vec{e} \times (\vec{e} \times \vec{c})}{\|\vec{e} \times (\vec{e} \times \vec{c})\|} \tag{3.7}$$

The cross product is only defined in $\Re^3$, so the resultant vector $\vec{R}$ has three components. For this 2D problem, the z-component is always zero; the x- and y-components are placed in $\mathbf{G}_P$. An example case of the placement of these components is shown in Eq. (3.8). This case is based on calculating the coefficients for Cell 3 at Node 11 in Figure 3.2. These terms will include contributions form the pressure acting on Edges 12 and 13. The symbol $R_x^{(12)}$ refers to the x component of the vector $\vec{R}$ when calculated for Edge 12.

$$\begin{bmatrix} G_{P_{1,1}} & \cdots & & & \\ \vdots & \ddots & & & \\ & & G_{P_{23,3}} = R_x^{(12)} + R_x^{(13)} & & \\ & & G_{P_{24,3}} = R_y^{(12)} + R_y^{(13)} & & \\ & & & & \ddots \end{bmatrix} \begin{Bmatrix} T_{P_1} \\ \vdots \\ T_{P_3} \\ \vdots \end{Bmatrix} = \begin{Bmatrix} F_{P_1} \\ \vdots \\ F_{P_{23}} \\ F_{P_{24}} \\ \vdots \end{Bmatrix} \tag{3.8}$$

3.2.3 Assembly

The geometric matrix is populated by looping through all edges and cells in the model. The two portions $\mathbf{G}_T$ and $\mathbf{G}_P$ are assembled into the full geometric matrix as shown in Eq. (3.9), whose form is identical to the original Eq. (3.2).

$$\left[\mathbf{G}_T \quad | \quad \mathbf{G}_P\right] \left\{ \frac{\mathbf{T_T}}{\mathbf{T_P}} \right\} = \mathbf{F} \tag{3.9}$$

3.3 Solution

Having assembled the Geometric Matrix in §3.2.2, and calculated the viscous forces in §3.1, two systems of equations in terms of forces at the nodes have been developed. By equating the right hand sides of Eq. (2.7) and Eq. (3.9), we can solve the system for the unknown tensions and pressures. But first, a closer inspection of the dimensionality of this system is necessary.

A system of equations can be either underdetermined, overdetermined, or have a unique solution. An underdetermined system will have infinitely many solutions; an overdetermined system has no unique solution. For any patch of cells which is surrounded by unbounded medium, it can be shown that this system is overdetermined, and has no unique solution.

The method to approximately solve overdetermined systems; the most well known is the least squares (LS) fit. The method minimises the sum of the squared residual error. For any vector $\mathbf{T}$, the residual error is defined by Eq. (3.10). The quantity to be minimised is the sum of the squares of the residual, which can be expressed as $\mathbf{r}^T\mathbf{r}$. The simplest method to minimise $\mathbf{r}^T\mathbf{r}$ is by solving the normal equations, Eq. (3.11) [63]. There are, however, a number of numerical problems with this formulation, and several more advanced methods for LS solutions to overdetermined systems exist.

$$\mathbf{r} = \mathbf{GT} - \mathbf{F} \tag{3.10}$$

$$\mathbf{G}^T\mathbf{GT} = \mathbf{G}^T\mathbf{F} \tag{3.11}$$

Due to the nature of the system, the geometric matrix is sparse. This fact enables us to make use of certain properties of properties of sparse matrices. To this end, the model employs the CSparse libraries developed by Timothy Davis of the University of Florida [26]. These libraries contain a robust method for performing a LS solution: QR decomposition.

Each time step is solved individually using the QR decomposition to affect a LS fit. The result, $\widehat{\mathbf{T}}$, is a time history of estimates of the tension in each edge and the pressure in each cell. Table 3.1 shows the mechanical and model properties for the 3-cell input patch from Figure 3.1. Any set of self-consistent units can be used in the FE model [14]. For the simulations here, base units of g, μm, and s were used for mass, length and time, respectively. The choice of these base units leads to the derived units for force, pressure (in 2D), and viscosity of $10^{-4} dyne$, $10^{-4} dyne/\mu m$, and $g/s \cdot \mu m$, respectively.

Table 3.1: Mechanical and model properties for the 3-cell input patch

γ_{gg}, $10^{-4} dyne$	7460
γ_{gm}, $10^{-4} dyne$	3730
μ, $g/s \cdot \mu m$	200
Number of Nodes/DOF	13/26
Number of Edges	15
Number of Cells	3
Total Number of Unknowns	18
Number of Steps, n	157
Interval between Time Steps	0.1

In Table 3.1, γ_{gg} is the tension in an edge between two green cells; likewise, γ_{gm} is the tension in an edge between a green cell and a the medium. μ is the viscosity of the cell contents. Pertinent model parameters are also shown.

The output from the identification algorithm for the 3-cell patch is shown in Figure 3.5. It can be seen from the figure, that the identification algorithm did correctly identify edge tensions and cell pressures for the 3-cell patch. Note also that the solution begins to diverge at later timesteps.

3.4 Sensitivity

In Figure 3.5, the output from the input patch, it can be seen that over time, the solution begins to diverge from the correct values, which are found in Table 3.1. The divergence in the solution is a numerical artefact of the least-squares (LS) solution method.

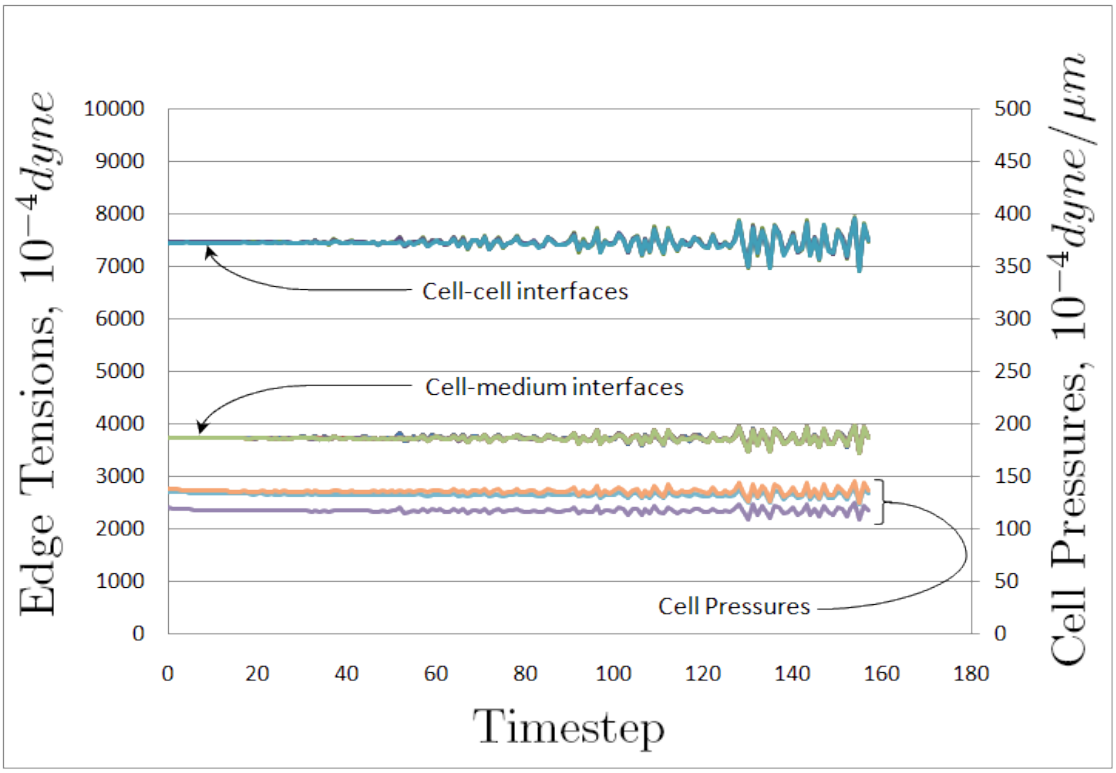

Figure 3.5: Output of the 3-cell model

The observed behaviour is because the problem is mathematically ill-posed, also known as ill-conditioned. With respect to a system of linear equations, a problem that is ill-posed will have a coefficient matrix which is near-singular. The structure of $\mathbf{G}$ matrix is such that $\mathbf{G}^T\mathbf{G}$ will always be near-singular.

An ill-posed problem will be very sensitive to input errors, and this problem is no different. The divergence observed in the output is due entirely to round-off error in node coordinates, which are stored with 6 significant figures. To assess the sensitivity of the input patch was corrupted with Gaussian random noise added to the nodal co-ordinates at each timestep. The corrupting noise induces error in the positions of the nodes prior to calculating the nodal displacements from one step to the next, and prior to the calculation of the damping and Geometric matrices from Eq. (2.7) and Eq. (3.2). The noise signal was mean zero (white noise) with a standard deviation scaled according to Eq. (3.12), where A_i is the area of a given cell, and N_C is the total number of cells.

$$\epsilon_0 = \sqrt{\frac{\sum\limits_{cells} A_i}{\pi N_C}} \tag{3.12}$$

Initially, a noise signal with $\sigma = \epsilon_0/50$ was used. It was found that this small amount of error in the input rendered the output completely unintelligible. The

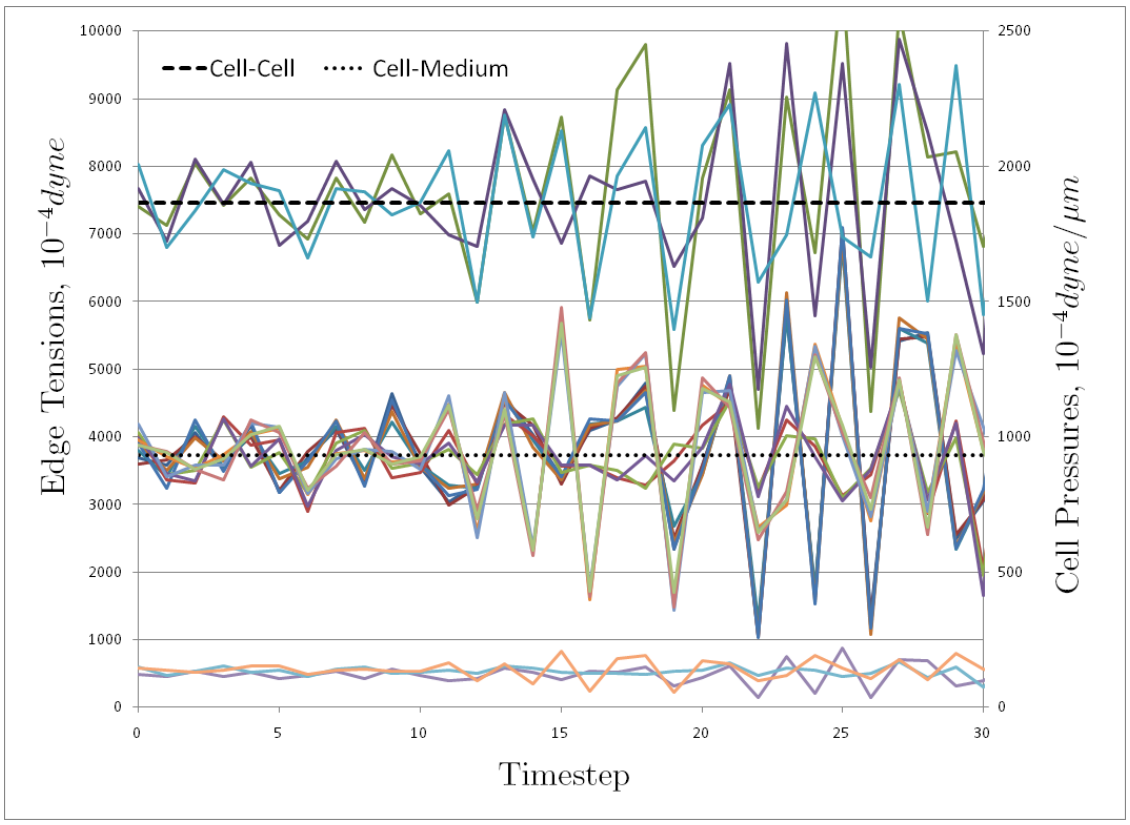

Figure 3.6: Scar output for the 3-cell model corrupted by noise. Rapid divergence of the solution.

problem is that noise in the input nodal coordinates is hugely amplified in the calculation of nodal displacements, which through Eq. (2.7), generate the right hand side of the identification equations. That result left the author rather taken aback; additional simulations were run with $\sigma = \epsilon_0/500$ and $\sigma = \epsilon_0/5000$, and still the results were unintelligible. Only at $\sigma = \epsilon_0/50000$ does the algorithm produce any meaningful results, and then only during the first few timesteps, as shown in Figure 3.6. After the first 25 or so timesteps, the solution quickly degrades.

Figure 3.7 shows the dramatic fall-off in the identification algorithm's performance when the input is corrupted by any amount of noise, and that the performance of the algorithm decreases with increasing input noise. The mathematics behind the performance measure shown in the figure are discussed in §4.1. The figure shows that any amount of noise dramatically reduces how well the fundamental elements of the algorithm perform, and that increasing amounts of noise further reduce the quality of the estimate. The identification algorithm is clearly an ill-posed system of equations, and the sensitivity is very high.

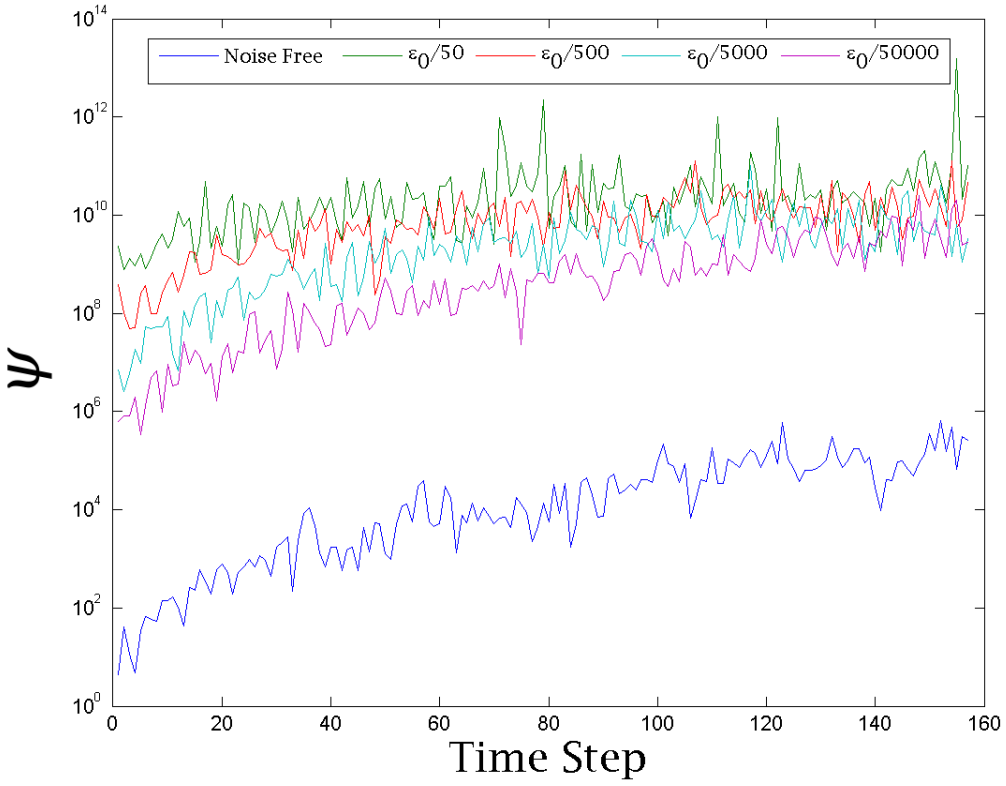

Figure 3.7: Estimator Performance for 3-cell model corrupted by noise

3.5 Live Data Mesh Extraction

As was discussed in §3.4, the model is very sensitive to input errors. Any process to extract a FE mesh from images of live tissues will necessarily be subject to some level of error. The sources of this error are discussed, and a procedure to reduce this error is presented.

3.5.1 Sources of Error

There are several sources of error which occur in the steps necessary to produce a FE mesh from live tissue. The signals corrupted by these errors are the nodal coordinates at each time step. The nodal coordinates are used to calculate nodal displacements and thence nodal forces, according to Eq. (2.7). In this way does input error propagate throughout the entire model.

The first avenue for error to occur is in the imaging of the tissue itself. The CCD capture of the image frequently has significant additive noise, and can also be corrupted by multiplicative noise. These two noise sources appear similar to the eye, but the signal processing techniques to remove them are quite different.

This noise in the image itself is more likely to cause problems with edge finding, watershed, and other image processing algorithms than to affect the coordinates of the nodes themselves. For a discussion of how these types of noise are treated, the reader is directed to the many texts on the subject [34, 36].

Another source of error comes from the projection of the 3D tissue surface onto a 2D image. Often times confocal microscope is used to capture a stack of $x-y$ images at a series of depths z through the tissue. If the surface of the tissue is curved, the image recorded by compositing the many confocal slices may be distorted when the stack is flattened from 3D to 2D. Portions of the recorded image affected this way might appear smudged or blurred, further impairing mesh extraction techniques.

The factors above all contribute to the inaccuracies in the extracted mesh, notwithstanding the fact that any such extraction algorithm will be subject to errors of its own. Current extraction techniques, subject to some of the sources of error discussed above, are far from perfect.

3.5.2 Smoothing

Ultimately, it is the cumulative effect of the many sources of error that is of interest to this study. While some of the individual error sources in the extraction process are likely to be normally distributed, others like out-of-plane effects are certainly not. Without substantially more detailed analyses of these sources of error, it is difficult to achieve any greater noise reduction than what smoothing can offer, assuming normally distributed, zero-mean error.

The Savitzky-Golay (SG) algorithm is a smoothing filter which, when convolved with a signal, reduces noise. The main advantage of the SG method over say a moving average or Gaussian smoothing filter, is that local extrema are preserved. Representative output comparing the performance of the SG filter with a moving average is shown below in Figure 3.8. Where an averaging filter deadens peaks in a signal as it smooths, the SG algorithm is essentially a windowed polynomial fit. Using LS regression, the polynomial of order k is fit to at least $k+1$ terms [68]. Here, smoothing order is denoted O_S and smoothing window size is denoted W_S. Another advantage of the SG algorithm is that the window need not be symmetrical, and a smoothed output signal is not truncated by half the window size as in a moving average filter. The code for implementing a SG filter was adapted from *Numerical Recipes 3rd Edition* [68].

The SG smoothing filter is applied to each node ordinate. That is, the position in x of Node 1 is treated independently of the position in y of the same node. This was done for ease of application. The smoothed nodal coordinates are then used for input to calculate nodal displacements, and the remainder of the identification algorithm proceeds as usual.

The selection of parameters used for the smoothing filter depends greatly on the data. In general, fitting a polynomial of order 2 and a window size of 31 has

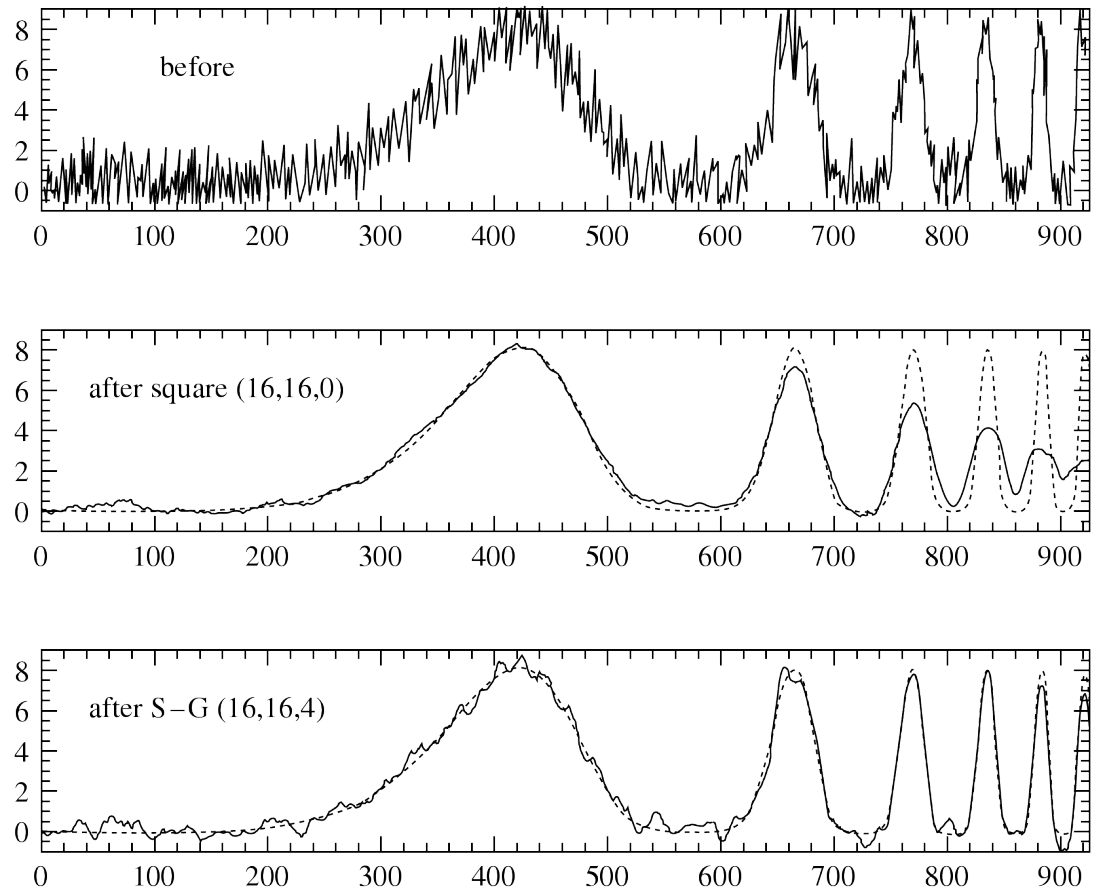

Figure 3.8: Representative output comparing the Savitzky-Golay smoothing filter with a moving average filter [68]

proven effective. The original, noise corrupted, and smoothed node position for a single DOF is shown below in Figure 3.9. In the figure, it is difficult to distinguish between the raw and smoothed node ordinate; the two are almost coincident.

Figure 3.10 shows the nodal displacement at the same DOF as Figure 3.9 for the raw, noise corrupted, and smoothed cases. Here it can be plainly seen that the small amount of noise corrupting the node coordinates has a profound effect on the nodal displacements, and that the SG filter has removed a great deal of noise.

The effects of the SG filter on Scar's performance are discussed in §4.4. That discussion includes a parameter study for the SG filter itself, as it relates to the final output.

3.6 Recursive Least Squares with Forgetting Factors

An extension to standard least squares (LS) algorithms is the Recursive Least Squares (RLS) method, which was discussed in §2.3. The RLS method updates

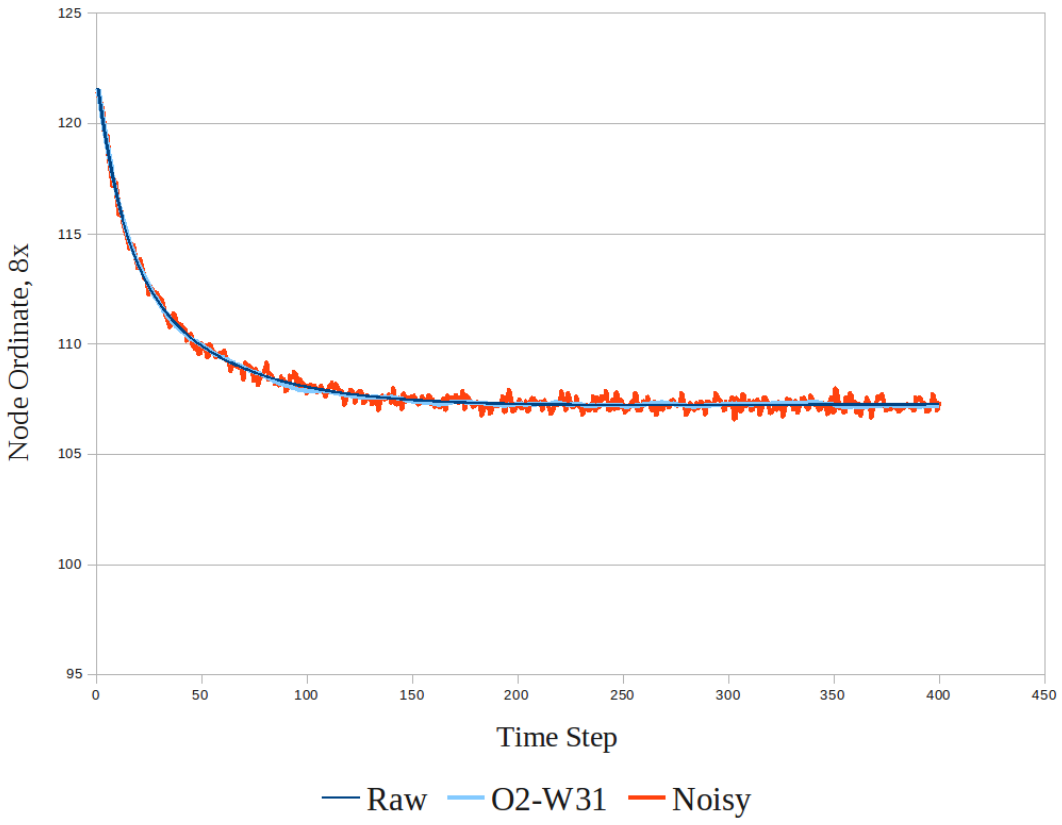

Figure 3.9: Original, noise corrupted, and smoothed node ordinate

the current estimate with any new observations from the system. By including a forgetting factor (FF) in the formulation of the estimator, older information is weighted exponentially less than the new information.

Assuming that the magnitudes of the tensions and pressures being estimated are changing slowly, a RLS estimator can be used to include information from previous time steps. The additional information should improve the conditioning of the problem, reducing the noise observed in the solution. To accomplish this, $\mathbf{G}_i$ and $\mathbf{F}_i$ are augmented with information from previous timesteps, subjected to an exponentially decreasing weight. For a FF λ, the augmented system at step i is:

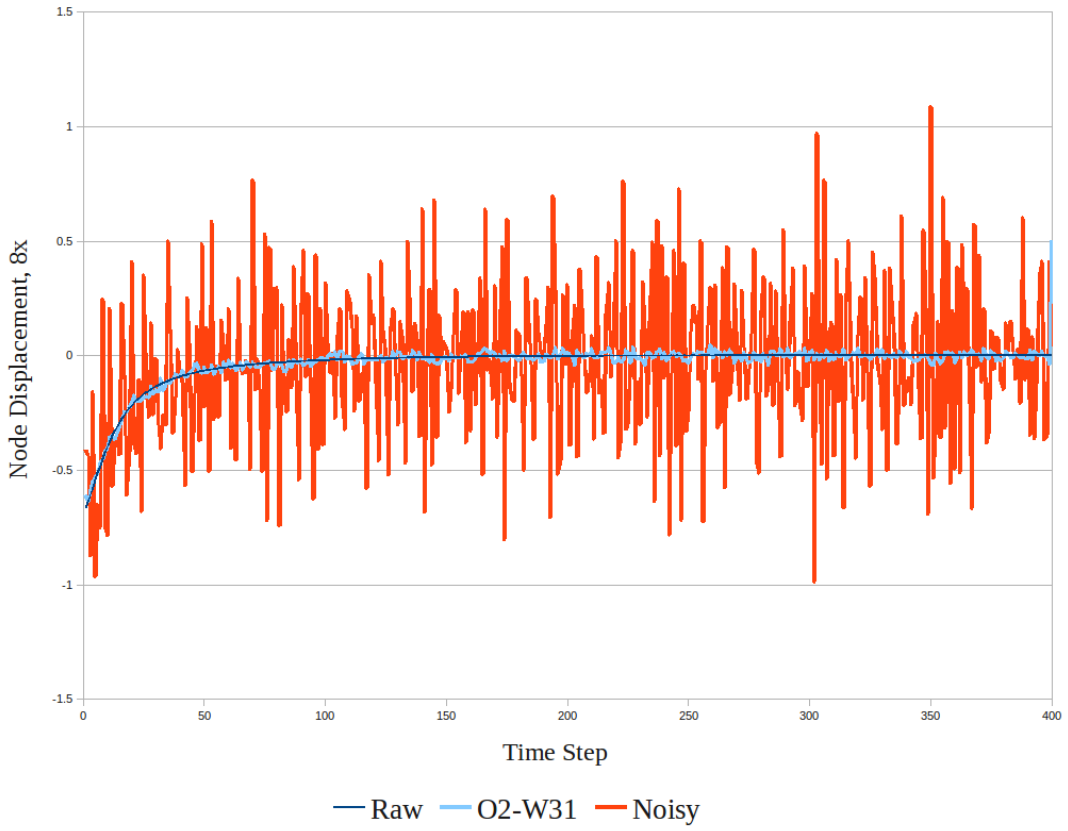

Figure 3.10: Original, noise corrupted, and smoothed node displacement for input

$$\begin{bmatrix} \mathbf{G}_i \\ (\lambda)\mathbf{G}_{i-1} \\ (\lambda)^2\mathbf{G}_{i-2} \\ \vdots \\ (\lambda)^k\mathbf{G}_{i-k} \\ \vdots \\ (\lambda)^i\mathbf{G}_0 \end{bmatrix} \left\{ \widehat{\mathbf{T}} \right\} = \begin{Bmatrix} \mathbf{F}_i \\ (\lambda)\mathbf{F}_{i-1} \\ (\lambda)^2\mathbf{F}_{i-2} \\ \vdots \\ (\lambda)^k\mathbf{F}_{i-k} \\ \vdots \\ (\lambda)^i\mathbf{F}_0 \end{Bmatrix} \tag{3.13}$$

or

$$\sum_{k=0}^{i}[(\lambda)^k\mathbf{G}_{i-k}\widehat{\mathbf{T}}] = \sum_{k=0}^{i}[(\lambda)^k\mathbf{F}_{i-k}]$$

and the LS problem is solved in the normal way. Eq. (3.13) can be formulated in terms of update laws, following the prototypes in Eq. (2.16), which is much more efficient computationally.

Figure 3.11 compares the output for the 3-cell model given three different values

for the forgetting factor, $\lambda = \{0,\ 0.65,\ 0.9\}$. Recall from Table 3.1 the correct values for the parameters being identified. Qualitatively, it can be seen that the higher the FF in the RLS formulation, the better the results. Note that mathematically, a FF of $\lambda = 0$ is identical to the simple LS fit from §3.3.

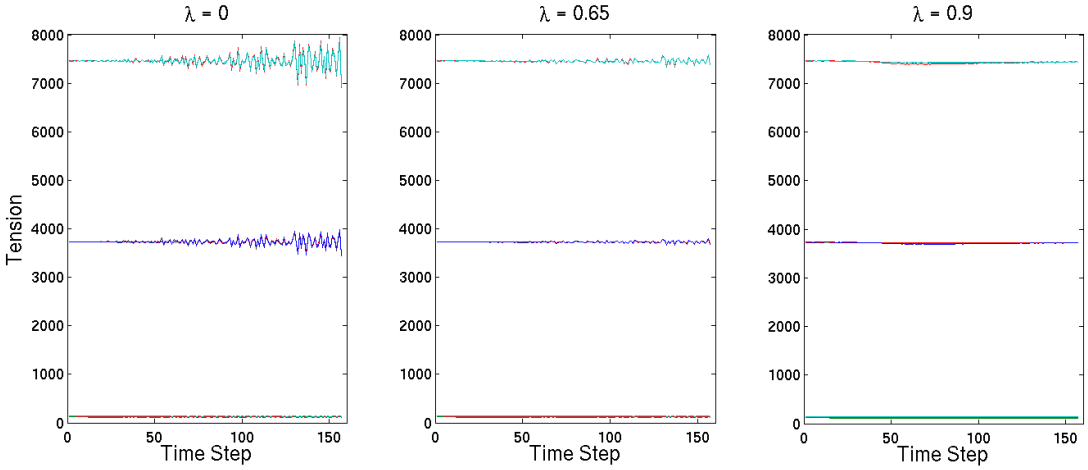

Figure 3.11: Scar output using RLS and multiple forgetting factors

3.6.1 Variable Forgetting Factors

A variable forgetting factor (VFF) has been developed for this study. In this thesis, λ denotes a constant FF, while λ_i is FF which varies over time. Several VFF formulations were discussed in §2.3. When the method uses gradients of the estimate, updates to λ_i may lag behind what is actually happening in the data. In other words, if the parameters of a system stabilise at particular values, the estimator may be slow to track a change in those values. The VFF update law in this study follows the philosophy the original Fortescue formulation [29], and scales λ_i according to an exponential of the normalised prediction error, as shown in Eq. (3.14) through Eq. (3.16).

First, the prediction error ε_i is calculated. The prediction error is normalised by the number of degrees of freedom (DOF), N_{DOF}, in the cell patch. The prediction error at a particular step is the residual one would calculate using the previous step's parameters with the current step's observations. A high prediction error means the parameters are changing quickly.

$$\varepsilon_i = \frac{\|\mathbf{F}_i - \mathbf{G}_i \widehat{\mathbf{T}}_{i-1}\|}{\sqrt{N_{DOF}}} \tag{3.14}$$

Next, a moving average of the prediction error $\bar{\varepsilon}_i$ is calculated, to smooth the volatility that can be present in the prediction error calculations. The size of the window is N_w.

$$\bar{\varepsilon}_i = \frac{\bar{\varepsilon}_{i-1} + \varepsilon_i - \varepsilon_{i-N_w+1}}{N_w} \tag{3.15}$$

Finally, λ_i – the FF at timestep i – is calculated according to the exponential

$$\lambda_i = 1 - e^{\left[\frac{\beta|\bar{\varepsilon}_i|}{\Delta t\, \bar{\mathbf{T}}_{N_w-1}}\right]} \tag{3.16}$$

where the limits $0.02 \leq \lambda_i \leq 1$ are imposed. β is a scaling term which controls the adaptation speed of the update law. In this way, the larger the prediction error, the smaller λ_i becomes. The mean prediction error, $\bar{\varepsilon}$ is normalised by the time increment Δt and the mean value of the parameter estimate vector $\widehat{\mathbf{T}}$ after $N_w - 1$ steps, denoted as $\bar{\mathbf{T}}_{N_w-1}$. It is assumed that the window size is chosen such that the parameter vector has stabilised after $N_w - 1$ steps, however the choice of window size must also account for the smoothing effects N_w has on $\bar{\varepsilon}_i$.

Figure 3.12 shows a representative history for λ_i calculated using the scheme described in this section. The patch used was specifically constructed with slowly and suddenly varying parameters to induce the VFF to adapt. The accompanying surface plot shows how λ_i propagates as a weight on adjacent timesteps j as an exponential function Eq. (3.17), where $w_{j|i}$ is the weight applied to information from timestep j when solving for timestep i. To interpret the surface plot, first determine which timestep i is being solved. Taking timestep 38 as an example, the weights applied to each neighbouring timestep are indicated by the green line. The weight applied to neighbouring timesteps has been introduced in this thesis before, as the exponential terms $(\lambda)^k$ in Eq. (3.13) for the back-looking constant FF. This figure shows a non-causal (forward- and back-looking) formulation, which is presented in §3.7.2.

$$w_{j|i} = (\lambda_i)^{|i-j|} \tag{3.17}$$

3.7 Sub-patches

So far, everything in the discussion has involved patches of cells with free edges. When using synthetic data, this is a condition that can be imposed at will. In the case of live data, we are frequently not so fortunate. Most times what we have is an image of a region of a tissue: the field of view of the microscope. This view of the tissue is referred to as a sub-patch of cells, or alternatively a patch with 'frayed boundaries'.

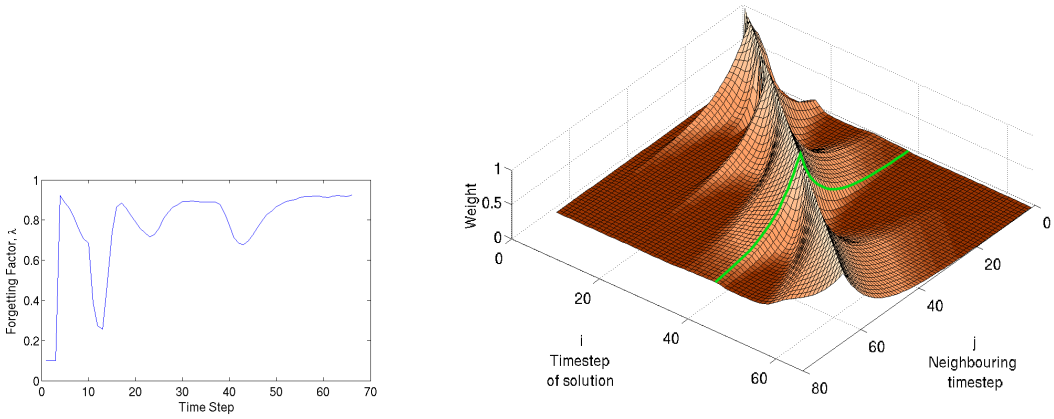

(a) λ_i over time for a patch with slowly time-varying parameters

(b) Propagation of weights on information from neighbouring timestep j, when solving timestep i

Figure 3.12: History of a VFF λ_i, and the distribution of weights across neighbouring timesteps

3.7.1 Contributions to Nodal Forces

Mechanically, the analysis of a sub-patch brings additional forces into play which must be considered. Consider the patch of cell shown in Figure 3.13. In this figure, suppose the solid cells are fully within the microscope's field of view. All other cells are only partially visible, or at least not fully visible for the entire time course.

In Figure 3.13 one can see forces acting on the frayed boundary of the patch from the surrounding tissue. Edges directed radially outward from the boundary of the sub-patch exert tensions on the nodes to which they are connected. Radial edge tensions are shown in red; some are omitted for clarity. Cells along the boundary exert pressures on the sub-patch. Some representative pressures are indicated in blue. Any stresses in the tissue as a whole – called far-field stresses – are transmitted to the sub-patch through these tensions and pressures.

Rather than attempt to identify each tension and pressure which is outside the sub-patch, these parameters are combined into unknown boundary force components in x and y. This approach also accommodates unknown support reactions in the case of statically indeterminate patches with free edges. The unknown force component pairs are shown in yellow in Figure 3.13.

In §3.3 we said that the system of equations $\mathbf{GT} = \mathbf{F}$ was overdetermined for patches with free boundaries. It was for this reason that a simple least squares fit could solve for the unknown tensions and pressures. For the sub-patch with frayed boundaries this is no longer the case. Each boundary force constitutes another pair of unknown parameters to identify. At the same time, there are still only two equations of equilibrium at each node. For the sub-patch, the same system $\mathbf{GT} = \mathbf{F}$ is now underdetermined. Three more equations of equilibrium can be added, taking

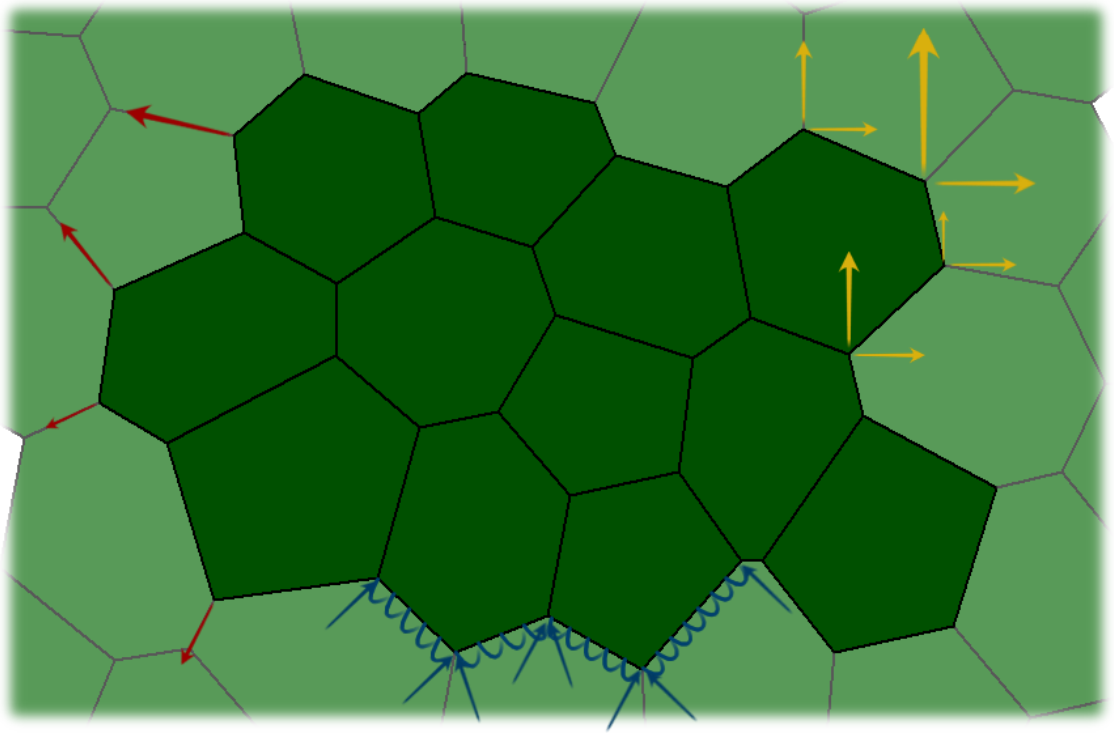

Figure 3.13: Sub-patch of cells showing additional forces from truncated cells

the entire sub-patch as a free body, and the unknown component pairs as forces acting on it.

The form of the new system for a sub-patch with frayed boundaries is shown in Eq. (3.18). The bulk of the matrix is constructed as outlined in §3.2, and these portions of the system are denoted by their respective symbols. The **0** denotes a zero filled region. The upper-right region of $\mathbf{G}^{(Aug)}$ has ones in rows corresponding to DOF on the boundary of the sub-patch, and in columns corresponding the unknown boundary force components R. The last three rows appended to $\mathbf{G}$ are the equations of equilibrium for the sub-patch as a free body: $\sum F_x$, $\sum F_y$, and $\sum M_o$. The coefficients in the last row are the nodal coordinates – N_{1_x}, N_{1_y}, etc. – which are the moment arms for each of the unknown boundary force components. Representing the unknown boundary forces as component pairs greatly simplifies this step.

$$\mathbf{G}^{(Aug)}\mathbf{T}^{(Aug)} = \mathbf{F}^{(Aug)}$$

$$\left[\begin{array}{c|cccccc} & 1 & 0 & 0 & 0 & \cdots & 0 \\ & 0 & 1 & 0 & 0 & & 0 \\ \mathbf{G} & 0 & 0 & 1 & 0 & & 0 \\ & 0 & 0 & 0 & 1 & & 0 \\ & \vdots & & & & \ddots & \vdots \\ & 0 & 0 & 0 & 0 & \cdots & 1 \\ \hline & 1 & 0 & 1 & 0 & & 0 \\ \mathbf{0} & 0 & 1 & 0 & 1 & \cdots & 1 \\ & N_{1_y} & N_{1_x} & N_{2_y} & N_{2_x} & & N_{n_x} \end{array}\right] \left\{\begin{array}{c} \mathbf{T} \\ \hline R_{1_x} \\ R_{1_y} \\ R_{2_x} \\ R_{2_y} \\ \vdots \\ R_{n_y} \end{array}\right\} = \left\{\begin{array}{c} \mathbf{F} \\ \\ \\ \\ \hline 0 \\ 0 \\ 0 \end{array}\right\} \tag{3.18}$$

3.7.2 Non-Causal Variable Forgetting Factor

Having described mathematically the relationships between tensions, pressures, and unknown boundary forces on the sub-patch, the system of equations must be solved. §3.7.1 discussed how the system described by Eq. (3.18) is underconditioned, and cannot be solved by normal means. However, the same technique used to improve the conditioning of the base model can be employe here. RLS combines many observations to estimate the value of a parameter. In the case of the sub-patch, why not then combine observations from several adjacent time steps – resulting again in an over conditioned system – and solve that augmented system.

A proper RLS formulation is back-looking only, that is, RLS is causal. The reason for this is that it allows the RLS filter to be used for on-line identification, as in an industrial plant. This study has no need for on-line identification. This frees us to combine information from time steps both prior and subsequent to the time step of interest: a non-causal approach. A non-causal combining of observations helps to reduce any bias in the estimate; if the value of the parameter is changing monotonically then combining only prior observations would cause the estimate to be skewed higher or lower than its true value. Only at a local extrema will the non-causal combination bias the estimate.

Using the VFF from §3.6.1, and in a manner similar to Eq. (3.13), time steps in both directions are directions are combined to write a system of equations which can be solved using least squares. At time step i, the system to estimate the tensions and pressures in the sub-patch with n timesteps is

$$\begin{bmatrix} (\lambda_i)^i \mathbf{G}_0^{(Aug)} \\ \vdots \\ (\lambda_i)^k \mathbf{G}_{i-k}^{(Aug)} \\ \vdots \\ (\lambda_i)^2 \mathbf{G}_{i-2}^{(Aug)} \\ (\lambda_i) \mathbf{G}_{i-1}^{(Aug)} \\ \mathbf{G}_i^{(Aug)} \\ (\lambda_i) \mathbf{G}_{i+1}^{(Aug)} \\ (\lambda_i)^2 \mathbf{G}_{i+2}^{(Aug)} \\ \vdots \\ (\lambda_i)^k \mathbf{G}_{i+k}^{(Aug)} \\ \vdots \\ (\lambda_i)^{n-i} \mathbf{G}_n^{(Aug)} \end{bmatrix} \left\{ \mathbf{T}^{(Aug)} \right\} = \begin{Bmatrix} (\lambda_i)^i \mathbf{F}_0^{(Aug)} \\ \vdots \\ (\lambda_i)^k \mathbf{F}_{i-k}^{(Aug)} \\ \vdots \\ (\lambda_i)^2 \mathbf{F}_{i-2}^{(Aug)} \\ (\lambda_i) \mathbf{F}_{i-1}^{(Aug)} \\ \mathbf{F}_i^{(Aug)} \\ (\lambda_i) \mathbf{F}_{i+1}^{(Aug)} \\ (\lambda_i)^2 \mathbf{F}_{i+2}^{(Aug)} \\ \vdots \\ (\lambda_i)^k \mathbf{F}_{i+k}^{(Aug)} \\ \vdots \\ (\lambda_i)^{n-i} \mathbf{F}_n^{(Aug)} \end{Bmatrix} \tag{3.19}$$

These equations can be used to estimate the tensions and pressures in a patch with frayed boundaries. Given a series of FE meshes extracted from microscope images of live tissue over time, it is now possible to identify the history of tensions and pressures which drove the observed motions. The performance of the identification algorithm is assessed in Chapter 4.

Chapter 4

Results and Discussion

In this chapter, we first present some metrics by which the performance of the identification algorithm can be assessed, and discuss the merits of each. A series of synthetic data sets are presented, upon which the algorithm is tested. Finally, we show how the algorithm may be refined by adjusting the tuning factors developed in Chapter 3, and discuss the results from synthetic data.

4.1 Performance Measures

To evaluate and compare the effects of the various components of the identification algorithm, it is necessary to develop metrics for the performance of the estimation algorithm. Three metrics were developed for assessing the quality of the estimate. Later, when the algorithm is applied to live data, the actual interfacial tensions and intracellular pressures will not be available; a metric independent of those values will be needed to have any confidence in estimates of parameters in live data patches.

4.1.1 RMS Residual

The first measure of estimator performance to be explored was a normalised RMS residual. Since the least-squares (LS) solution is based on a minimization of the residual, this approach gives us a direct measure of the extent to which the residual has been minimized, and hence, a direct measure of the quality of the fit of the estimated parameters for the system. The RMS residual at Time-step k is calculated according to Eq. (4.1). The term $1/N_{DOF}$ normalizes the residual according to the number of degrees of freedom (DOF) in the FE model.

$$r_{RMS_k} = \sqrt{\frac{1}{N_{DOF}}(\mathbf{F}_k - \mathbf{G}_k\widehat{\mathbf{T}}_k)^T(\mathbf{F}_k - \mathbf{G}_k\widehat{\mathbf{T}}_k)} \tag{4.1}$$

Lower values of r_{RMS} indicate better performance of the estimator. In theory, the normalization by $1/n$ should allow us to compare Scar's performance between different cell patches, since the scale of each patch should be factored out.

The residual has units of force. The discrepancy in the dimensions of tensions and pressures is accounted for in the units of the various entries in $\mathbf{G}$. Those coefficients which multiply a tension parameter are dimensionless; those which multiply a pressure parameter have dimensions of length. Since the edge tensions have units of force and the cell pressures have units of force per length, all terms in the residual vector $\mathbf{F}_k - \mathbf{G}_k\widehat{\mathbf{T}}_k$ have units of force.

4.1.2 Covariance Matrix

The covariance matrix, $\mathbf{\Sigma}$, was discussed in §2.3; it arises as an intermediate step in multidimensional LS solutions. The diagonal of $\mathbf{\Sigma}$ contains estimates of the variance of each parameter. Taking the sum of each variance estimate for edge tensions only, the result can be thought of as an estimate of the quality of the fit of those tensions. This metric is called ψ, and is calculated according to Eq. (4.2) at Time-step k, where $tr(*)$ denotes the trace of a matrix.

$$\psi_k = tr(\mathbf{\Sigma}_k) = tr(\mathbf{P}_k)s_e^2 \tag{4.2}$$

The matrix $\mathbf{P}_k$ is calculated according to either Eq. (2.15) or Eq. (2.16), depending on whether or not the recursive formulation is used. For this model, the estimate of the standard error, s_e^2 is calculated according to Eq. (4.3). Here again, N_{DOF} is the number of DOF in the FE model. N_E and N_C are the number of edges and cells – and hence combined they are the total number of parameters to estimate – in the cell patch.

$$s_{e_k}^2 = \frac{1}{N_{DOF} - (N_E + N_C)}(\mathbf{F}_k - \mathbf{G}_k\widehat{\mathbf{T}}_k)^T(\mathbf{F}_k - \mathbf{G}_k\widehat{\mathbf{T}}_k) \tag{4.3}$$

Only the diagonal terms of $\mathbf{\Sigma}_k$ related to edge tensions are included in ψ_k. This is due to an inability to satisfactorily resolve the incompatible dimensionality between those terms related to tensions and those related to pressures. Any attempt to non-dimensionalise the diagonal terms of $\mathbf{\Sigma}$ must be based on generalized geometric properties of the input patch, which necessarily change over time. These changes would make a metric based on a non-dimensionalised $\mathbf{\Sigma}$ very difficult to defend, and even more difficult to compare between one cell patch and another. This shortcoming is accepted since it has been shown in §2.1.3 that tensions in the cortical edges of cells in a patch are predominantly responsible for driving self-rearrangement of cells and tissue reshaping.

4.1.3 Coefficient of Determination

The classic measure of the quality of a parameter fit for linear regression models is the coefficient of determination, R^2. In general terms, R^2 is one minus the ratio of the sum of squared errors to the total sum of squares [59]. In the context of the multivariate linear fit, R^2 is calculated according to Eq. (4.4).

$$R_k^2 = 1 - \frac{(\mathbf{F}_k - \mathbf{G}_k\widehat{\mathbf{T}}_k)^T(\mathbf{F}_k - \mathbf{G}_k\widehat{\mathbf{T}}_k)}{(\mathbf{F}_k - \bar{\mathbf{F}}_k)^T(\mathbf{F}_k - \bar{\mathbf{F}}_k)} \tag{4.4}$$

As with the RMS residual of §4.1.1, R^2 is dimensionally consistent, and therefore includes information regarding the quality of the estimated tensions *and* pressures. The metric is also normalized from 0 to 1, making comparisons between different cell patches possible. Such comparisons should be used with caution, however, as R^2 does not scale properly with model size [59].

4.1.4 Verification Performance Measures

A χ^2 test will be used with the early synthetic data results to validate the performance measures. χ^2 can be used for the synthetic data runs because the original parameters used in the forward simulations are available. If a correlation is seen between the performance measures and the χ^2 value, we can be more confident in applying the performance measures to the live data runs, and have a better understanding of when certain measures are more appropriate than others. For instance, it may be that one measure is more suitable for comparing results from different input patches, and another is only useful for evaluating how tuning factors affect the output of the identification algorithm. For the multivariate identification algorithm, χ_k^2 is calculated at timestep k according to

$$\chi_k^2 = \frac{1}{N_E + N_C} \sum_{i=1}^{N_E+N_C} \frac{(\widehat{\mathbf{T}}_{i,k} - \mathbf{T}_{i,k})^2}{\mathbf{T}_{i,k}} \tag{4.5}$$

4.2 Sources of Data

There exist two basic classes of displacement data which are available: synthetic data and live data. Synthetic data are generated using the forward model *Simba*, whose output is a displacement history. Live data are gathered by directly observing displacements in live cells over time.

Three different input patches were used for synthetic data. The 3-Cell patch used to demonstrate the identification algorithm in Chapter 3 is extensively used

in testing, partially because of its simplicity. The initial configuration of the patch is shown in Figure 4.1a; the final configuration is found in Figure 4.1b. The Variable Tension patch, as the name suggests, was created such the the tensions being estimated vary over the history of the motion. Initial and final configurations are found in Figure 4.2. The pressures will vary over the history of the motion, it was deemed appropriate to have a test patch where all parameters sought varied over time. Such variability is expected to be seen in live tissues. Finally, a larger patch with two different cell types was used. The interfacial tensions for this patch were set such that the 'red-type' cells sort internally to the 'green-type' cells. The initial and final configurations of the Sorting patch are shown in Figure 4.3.

All three test patches were generated using a random 2D Voronoi tessellation. The 3-Cell patch was stretched in the x direction and allowed to recoil to an equilibrium configuration. The Variable Tension patch was allowed to anneal from the generated Voronoi tessellation, under the influence of the slowly varying edge tensions. The correct values for edge tensions are indicated on any output plots for this patch. Deformations in the Sorting patch were driven by differential interfacial tensions between the two cell types. The forward FE model used to generate the Sorting patch output only one of every four steps. This was done to emulate sampling the continuous nodal displacement functions, such as would be done when extracting a mesh from live data.

The pertinent mechanical and simulation properties for all patches are listed in Table 4.1. These include the edge tensions for the various cell-cell and cell-medium interfaces, cell viscosity, number of time steps, and interval between timesteps. The units for the various physical quantities are discussed in §3.3.

Table 4.1: Mechanical and Model Properties for three test cases

Parameter	3-Cell Figure 4.1	Variable Tension Figure 4.2	Sorting Figure 4.3
γ_{gg}, $10^{-4}dyne$	7460	7310–7460	7500
γ_{gm}, $10^{-4}dyne$	3730	3730–3900	4000
γ_{gr}, $10^{-4}dyne$	—	—	10 000
γ_{rr}, $10^{-4}dyne$	—	—	3000
γ_{rm}, $10^{-4}dyne$	—	—	8000
μ, $g/s \cdot \mu m$	200	200	200
Number of Nodes/DOF	13/26	21/42	43/86
Number of Edges	15	26	57
Number of Cells	3	6	15
Total Number of Unknowns	18	32	72
Number of Steps	400	67	67
Interval between Time Steps	0.1	0.1	4

In Table 4.1, γ_{gg} is the tension in an edge between two green cells; likewise, γ_{gr}

is the tension in an edge between a green cell and a red cell, γ_{rm} is the tension in an edge between a red cell and the medium, and so on. μ is the viscosity of the cell contents. Pertinent model parameters such as the number of nodes, edges, and cells in the model, the total number of degrees of freedom in the model, the number of unknowns, and the number of times steps.

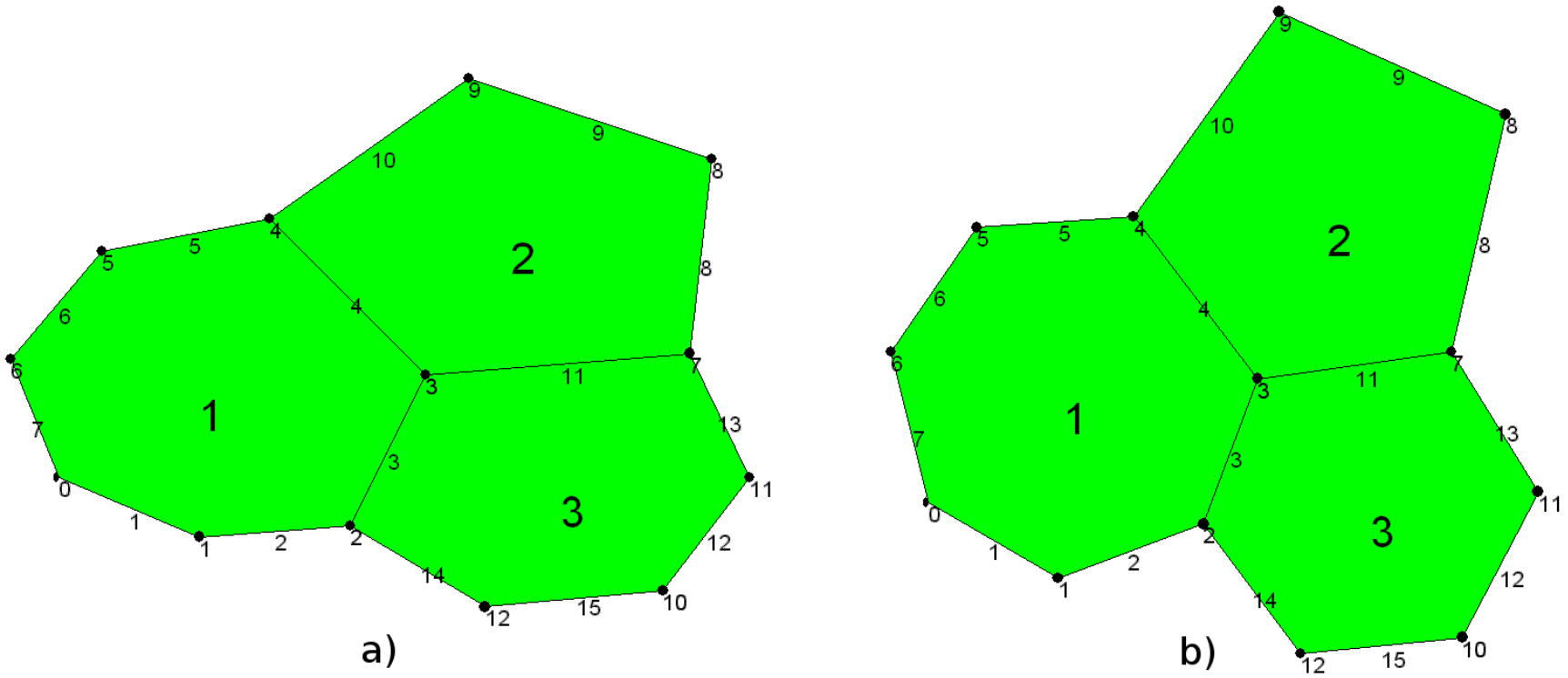

Figure 4.1: 3-Cell patch for Scar performance testing

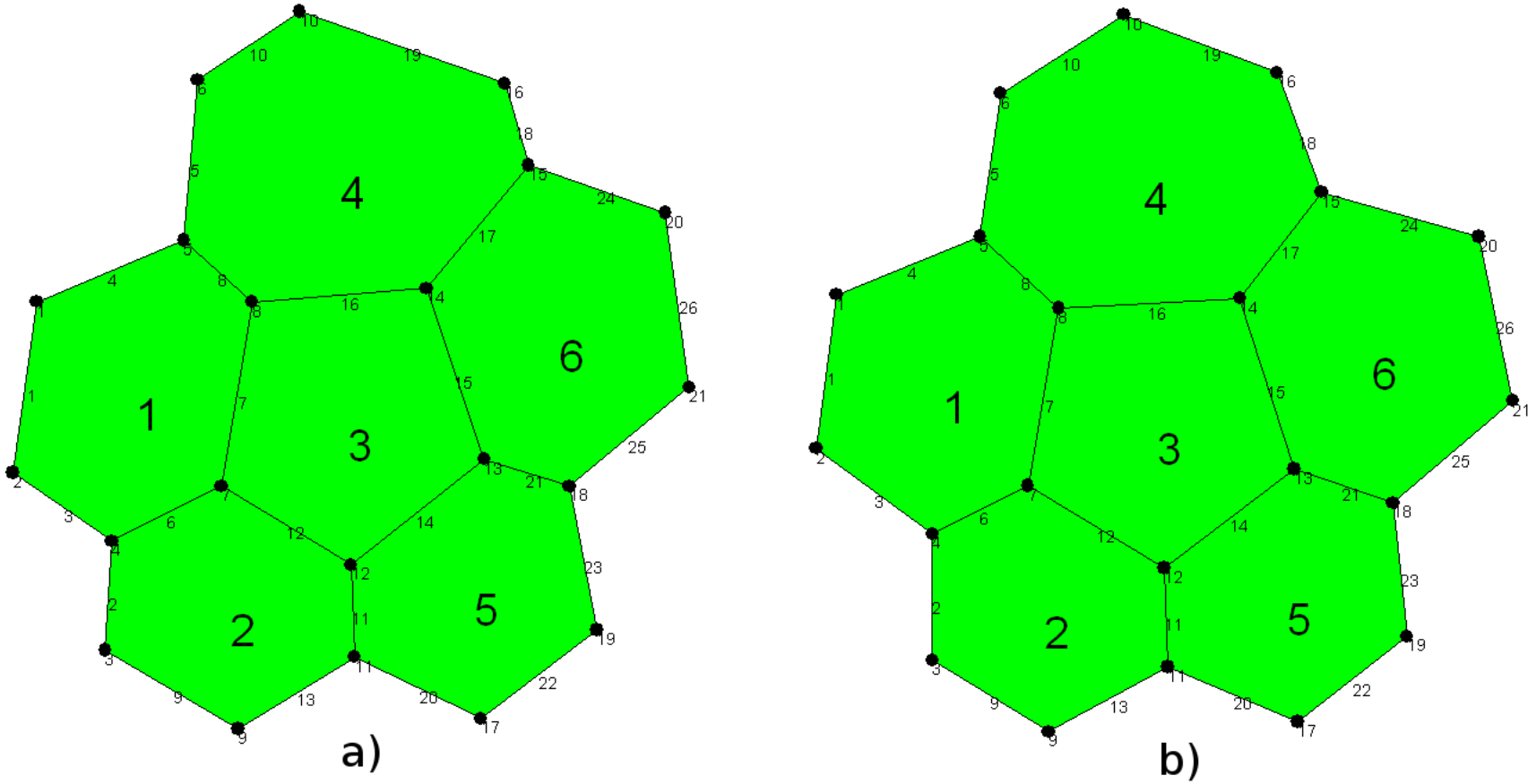

Figure 4.2: Variable Tension patch for Scar performance testing

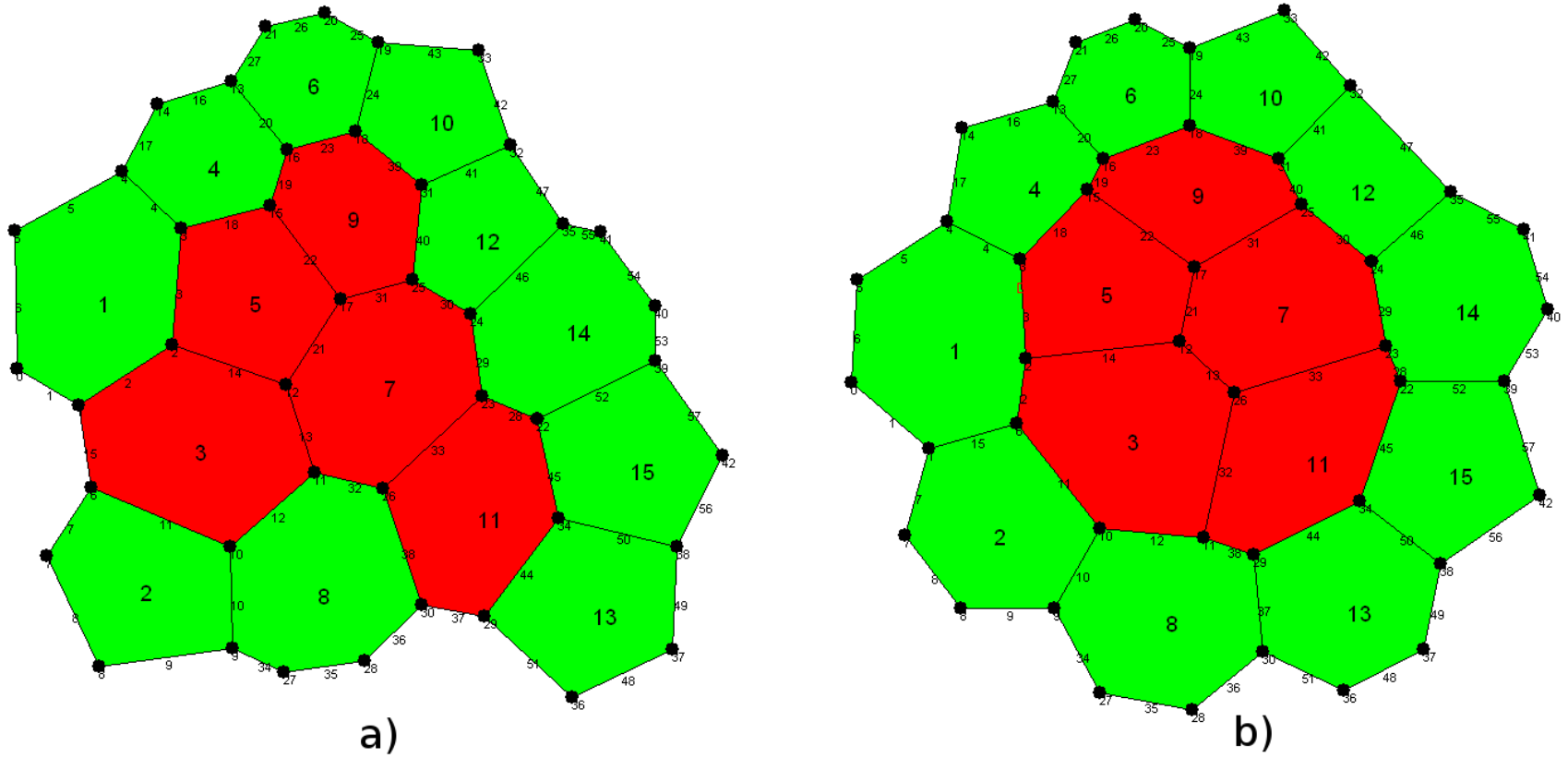

Figure 4.3: Sorting patch for Scar performance testing

4.3 Basic Algorithm Output

First performance of the basic elements of the identification algorithm is evaluated. That is, the elements of the algorithm discussed in §3.1–3.3. The basic algorithm output using the 3-Cell patch is shown in Figure 4.4.

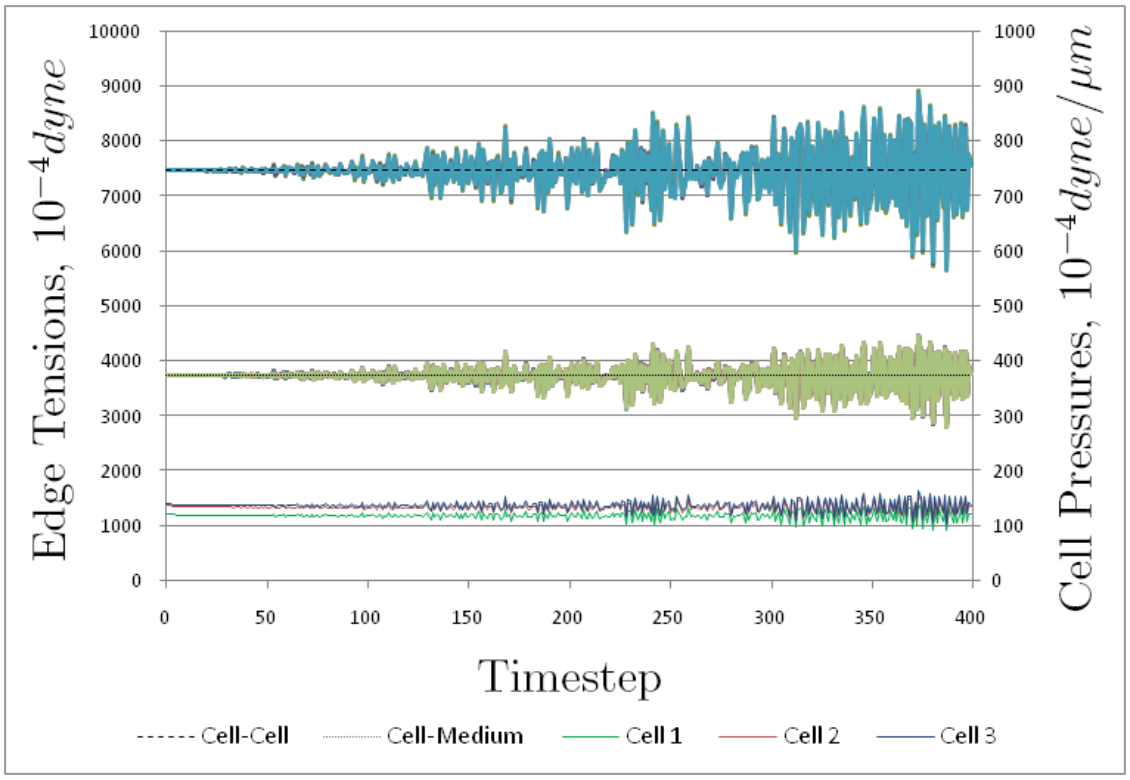

Figure 4.4: Output from the basic algorithm using the 3-Cell patch

The estimated tensions and pressures for the 3-Cell patch are shown in Figure 4.4. One can see that the identification algorithm estimated values for the cell-cell and cell-medium interfaces centred around the correct values from Table 4.1. Correct values are also shown in dashed and dotted black lines for cell-cell and cell-medium interfaces respectively. One also sees the estimate diverging from the correct values at later timesteps, as was done in §3.4. We understand this divergence to be a consequence of numerical artefacts in the solver, and refer to it as *solver noise*.

These qualitative observations of the algorithm output are useful, but it would be more effective to have quantitative measures of performance. Figure 4.5 shows each of the three performance measures defined in §4.1 plotted along with the χ^2 statistic.

The χ^2 measure confirms that the estimate is diverging from the correct parameter values at later timesteps. Both ψ and R^2 reflect that divergence. The r_{RMS} measure shows a consistently low value, which seems to suggest a good fit over the

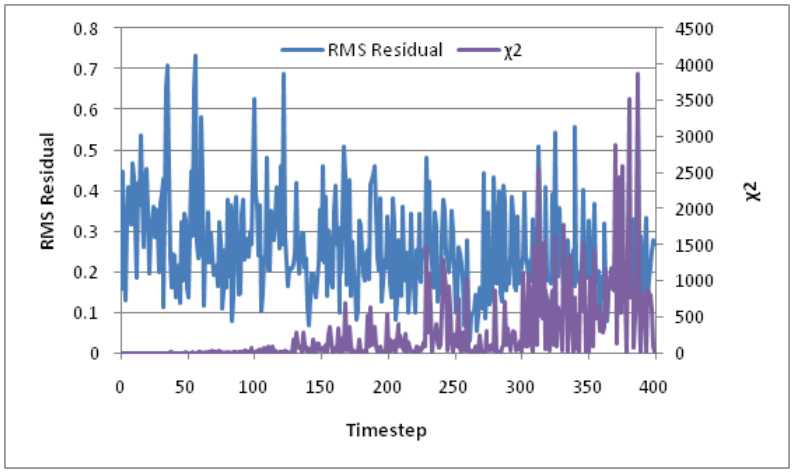

(a) RMS Residual

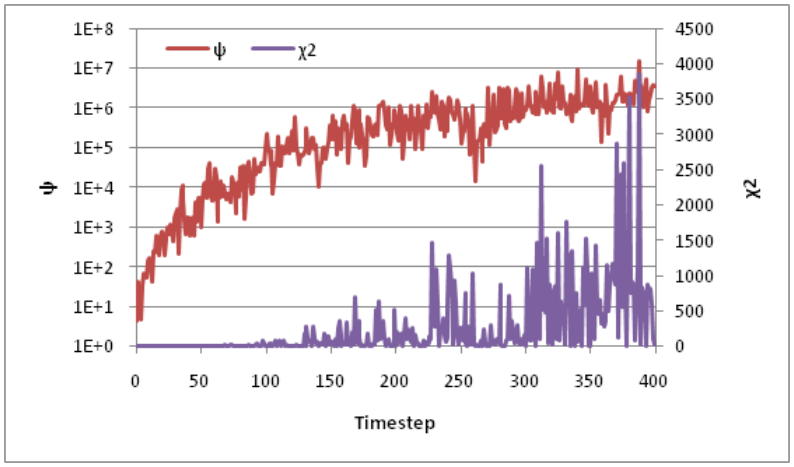

(b) Trace of the Covariance Matrix

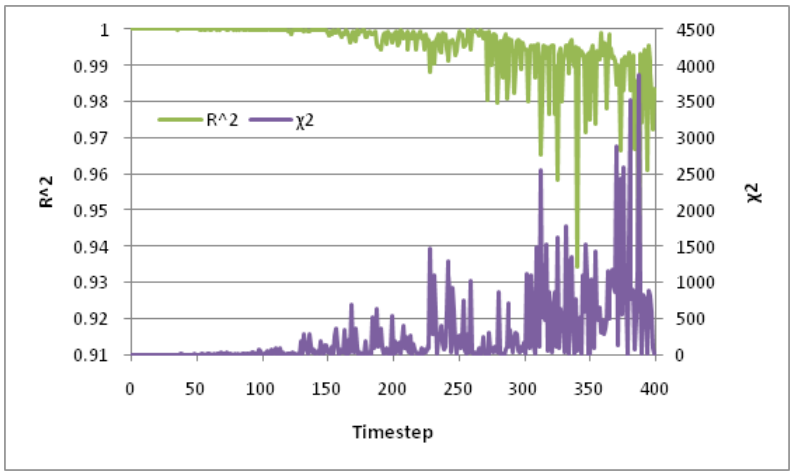

(c) Coefficient of Determination

Figure 4.5: Performance measures for the 3-Cell patch using the basic algorithm

whole history. The low value is deceptive, however, since the LS method minimises the residual. It is expected then, that r_{RMS} is consistently low, and since it disagrees with ψ and R^2, and more importantly χ^2, it shan't be given much credence for the basic algorithm.

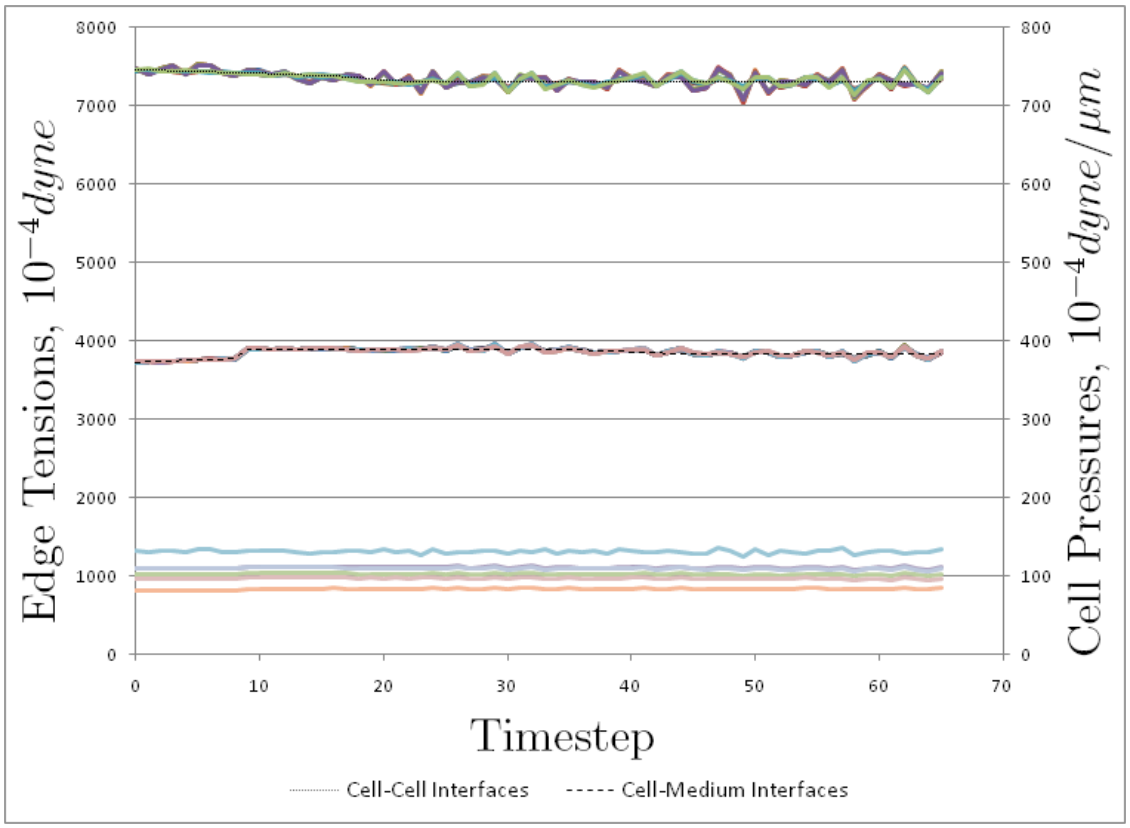

Figure 4.6: Output from the basic algorithm using the Variable Tension patch

The estimated tensions and pressures for the Variable Tension patch are shown in Figure 4.6. The dotted and dashed lines indicate the true values for the cell-cell and cell-medium interfaces respectively. The algorithm tracks changes in these parameters quite well. The sudden jump in cell-medium interfacial tension at timestep 7 is well represented in the estimated tensions. As with the 3-Cell patch there is output solver noise present in the later steps.

The χ^2 measure again confirms that the estimate is diverging slowly from the correct parameter values, a conclusion supported by the ψ and R^2 measures. The r_{RMS} is consistently low, as was seen with the 3-Cell patch, and does not reflect the degrading quality of the estimate.

At first glance, the quality of the estimate for the sorting patch does not appear as good as the previous two patches'. There a number of interesting features in the Figure 4.8. The most obvious are the spikes (truncated for clarity) in the estimated values for the parameters. These spikes coincide with neighbour changes during the simulation, are only one time step long. Since the neighbour change algorithm

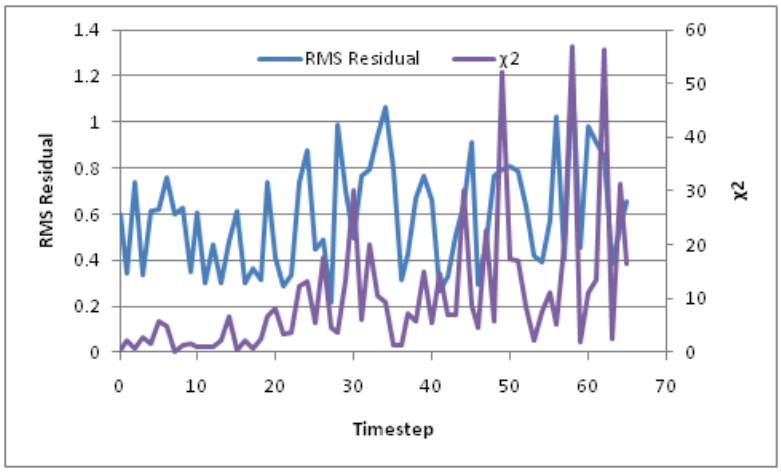

(a) RMS Residual

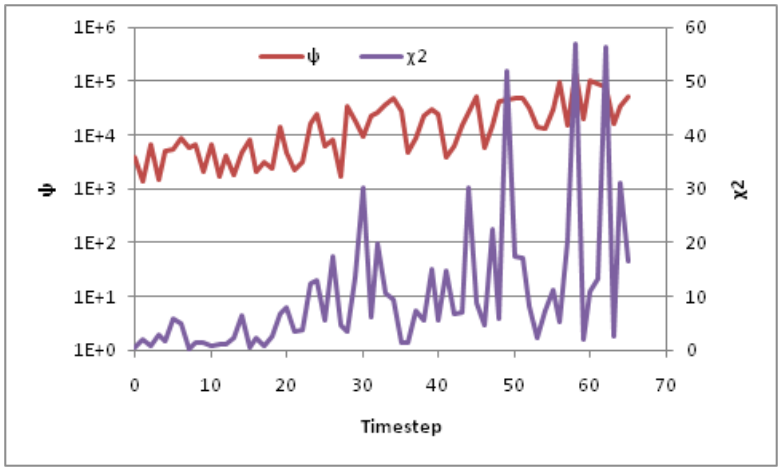

(b) Trace of the Covariance Matrix

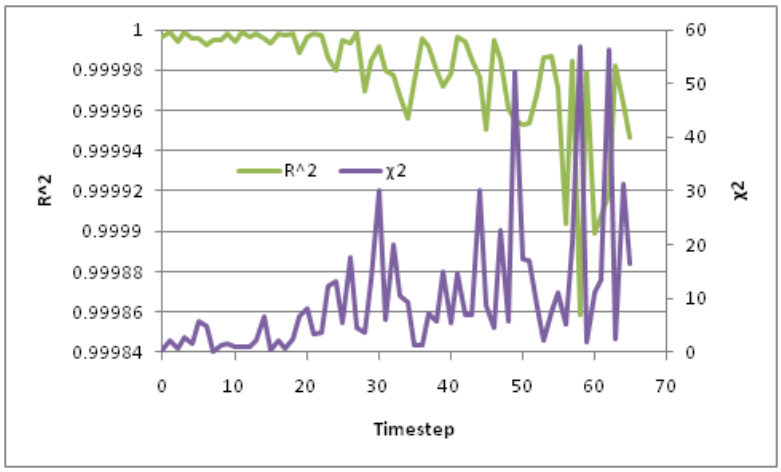

(c) Coefficient of Determination

Figure 4.7: Performance measures for the Variable Tension patch using the basic algorithm

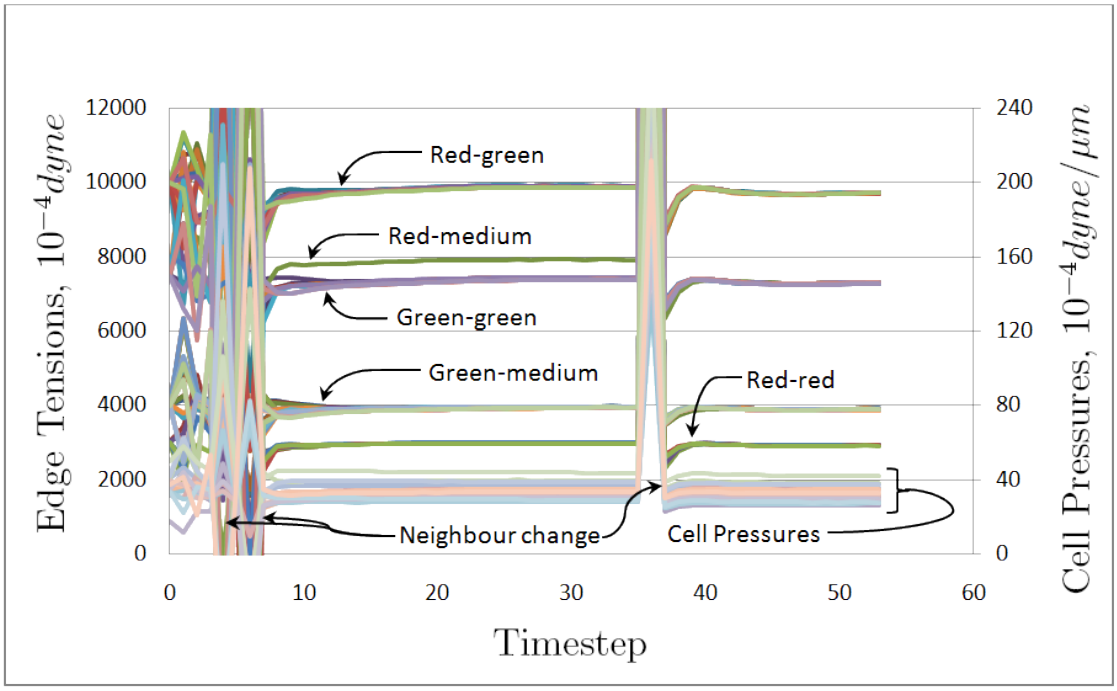

Figure 4.8: Output from the basic algorithm using the Sorting patch

in the forward model is an artificially imposed displacement, it was expected that the identification algorithm would not correctly identify parameters during these steps. One can also see a slow recovery of the solution to the correct value after these neighbour changes. It is unclear exactly why the re-convergence is delayed; the delay may be related to the 4:1 sampling rate used to create input patched for this algorithm from the output of the forward FE simulation. The effects of such sampling are most pronounced over the large displacements in the region of the neighbour change. The earliest timesteps appear to suffer from a similar effect. Further investigation may be required to identify the cause of this effect.

It is also shown in the figure above that Scar accurately tracks the abrupt change in tension in an edge following the neighbour change. During the neighbour change at timestep 37, Edge 52 changed from being a red-medium interface, to a green-green interface, thereby eliminating the last red-medium interface. In the figure, one can see the estimate of the tension in Edge 52 is roughly 8000 prior to the neighbour change - the appropriate value for a red-medium interface according to Table 4.1 - and after the neighbour change the tension is roughly equal to 7500 - the appropriate value for a green-green interface. All neighbour changes were tracked correctly, but this example is the most clearly visible in the figure.

The χ^2 measure shown in Figure 4.9 has spikes so large at each timestep involving neighbour change, accurately reflecting the incorrect parameter estimate during those steps. Those spikes are reflected in each of the three performance measures and the spikes completely dominate both the r_{RMS} and R^2. The ψ measure, however, does show the quality of the estimate improving slowly after neighbour

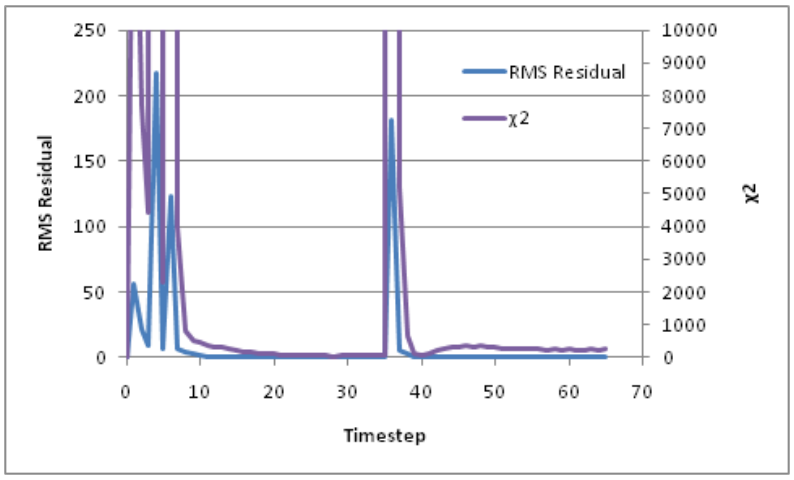

(a) RMS Residual

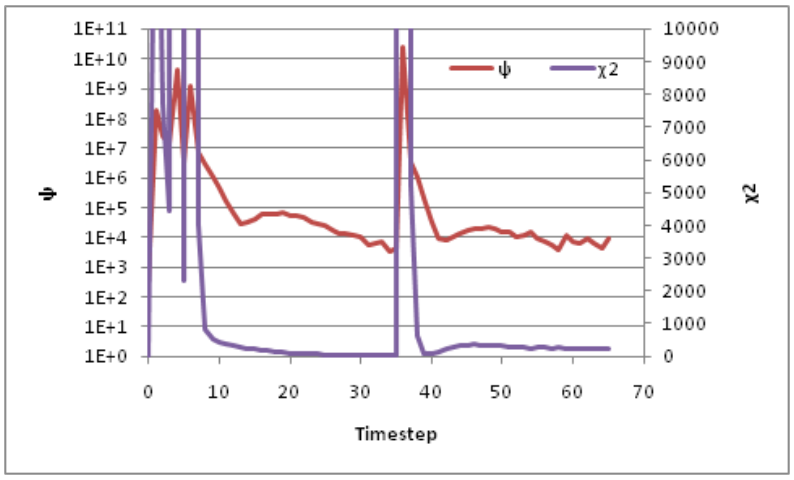

(b) Trace of the Covariance Matrix

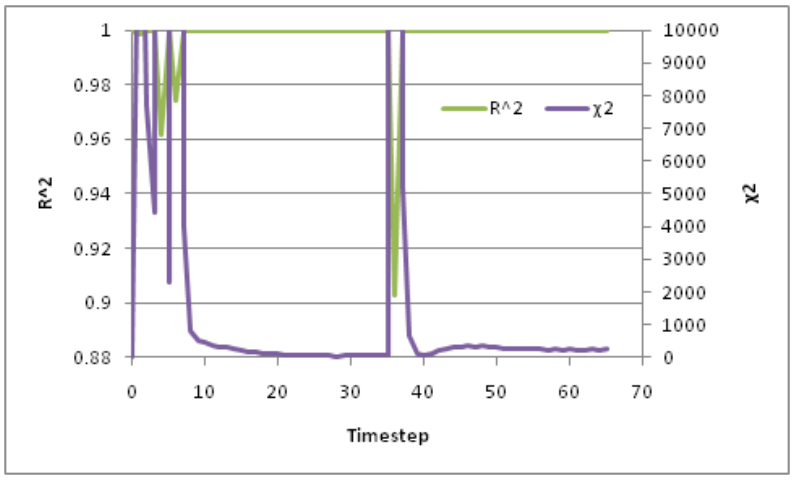

(c) Coefficient of Determination

Figure 4.9: Performance measures for the Sorting patch using the basic algorithm

Table 4.2: Comparison of performance measures for three input patches using the basic algorithm

Input Patch	r_{RMS}	ψ	R^2	χ^2
3-Cell	0.255	7.91e5	0.996	265
Variable Tension	0.594	2.32e4	1.00	10.2
Sorting	9.85	4.47e8	0.997	1.78e5

changes, in line with χ^2. If r_{RMS} were plotted on a log scale as is done for ψ, one sees the same improvement in estimate quality following the neighbour change. That plot is found in Figure 4.10.

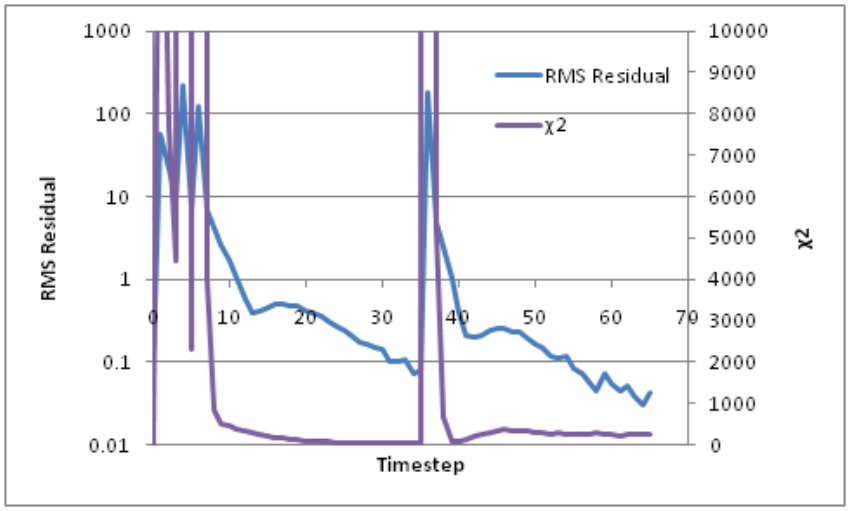

Figure 4.10: RMS Residual for the basic algorithm using the sorting patch - log scale

One can compare the overall performance of the identification algorithm for each patch by taking an average of each measure over the whole time history for each patch. That comparison is shown in Table 4.2. The table shows that by each measure, the algorithm performed best using the Variable Tension patch, and worst for the Sorting patch. Note that these averages do include those timesteps which involved a neighbour change in the Sorting patch, which dramatically effects the performance. One also sees that for all three patches, the R^2 value is nearly unity, which is not particularly useful. In fact, throughout this section so far, it can be said that ψ followed χ^2 most closely, and gave the most useful information.

To reduce the effects of the output solver noise, each patch was re-run using the RLS solution method with multiple constant and variable forgetting factors (FF). Table 4.3 shows the average ψ, R^2, and χ^2 measure for the several FF for each input patch. The r_{RMS} measure is omitted because it was found to be ineffective for the basic algorithm earlier in this section. If, for a particular row in the table, there is a value in the column λ, then that run was done using a constant FF using that value. If, on the other hand, there is a value in the column β, then that run was

done using a variable forgetting factor (VFF), with that value as the adaptation speed in the VFF formulation Eq. (3.16). The best value for each measure for each patch is shown in bold face.

Table 4.3: Basic algorithm performance using RLS with several Forgetting Factors

Input Patch	λ	β	ψ	R^2	χ^2
3-Cell	0.95	—	4.59e6	0.978	2.34
	0.65	—	3.48e6	0.983	17.9
	—	-0.01	-4.92e5	1.01	3.49
	—	-0.1	-4.95e5	1.01	3.49
	—	-1	-8.53e5	1.01	3.49
	—	-10	**4.01e5**	**1.00**	**2.07**
	—	-100	4.09e6	0.980	2.74
Variable Tension	0.95	—	9.33e6	0.992	78.8
	0.65	—	1.45e6	0.999	**2.48**
	—	-0.01	4.52e6	0.997	124
	—	-0.1	4.34e6	0.997	124
	—	-1	4.95e6	0.996	93.2
	—	-10	3.15e5	0.997	10.9
	—	-100	**1.76e4**	**1.00**	3.83
Sorting	0.95	—	5.76e9	1.01	5.30e4
	0.65	—	3.90e9	**0.962**	4.85e4
	—	-0.01	6.30e9	0.847	4.48e4
	—	-0.1	6.30e9	0.847	**4.48e4**
	—	-1	6.24e9	0.849	4.50e4
	—	-10	5.09e9	1.01	5.57e4
	—	-100	**1.67e9**	1.12	1.48e5

For the 3-Cell patch, all performance measures indicate that using a VFF with $\beta = -10$ produced the best estimates. The other two patches are less definitive. For the Variable Tension patch, χ^2 indicates that a constant FF of $\lambda = 0.65$ produced the best estimates, while the other two measures suggest that a VFF with $\beta = -100$ is best. For the Sorting patch, each measure indicated a different (V)FF was best. Since χ^2 directly measures deviations from the expected values, it must be used, when available, to determine the optimal (V)FF in this case. The identification algorithm output for the optimal case is shown, for each patch, in Figure 4.11. Whenever the notation (V)FF is used, it refers to constant and variable FF concomitantly.

Crucially, for each patch, most or all runs performed better with some from of RLS with either FF or VFF than the original runs reported in Table 4.2. Note however that the output shown in Figure 4.11(c) does not appear to be very good, despite having the best reported χ^2. Shown in Figure 4.12, one can see that using a constant $\lambda = 0.65$ produces much better results. This could be due to including the steps involving neighbour changes in the performance measures. The performance

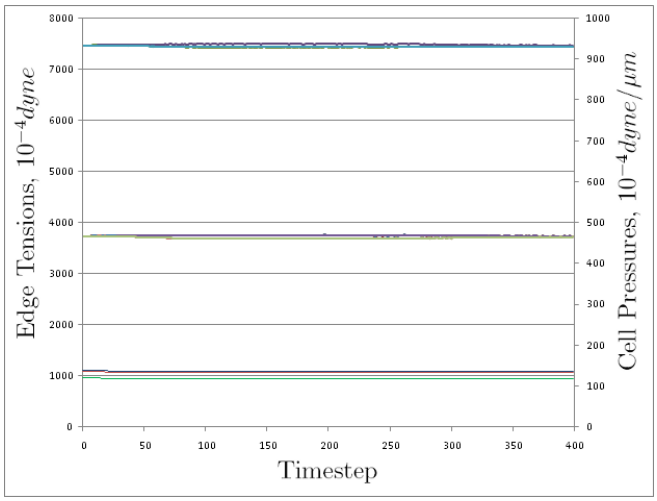

(a) 3-Cell - VFF: $\beta = -10$

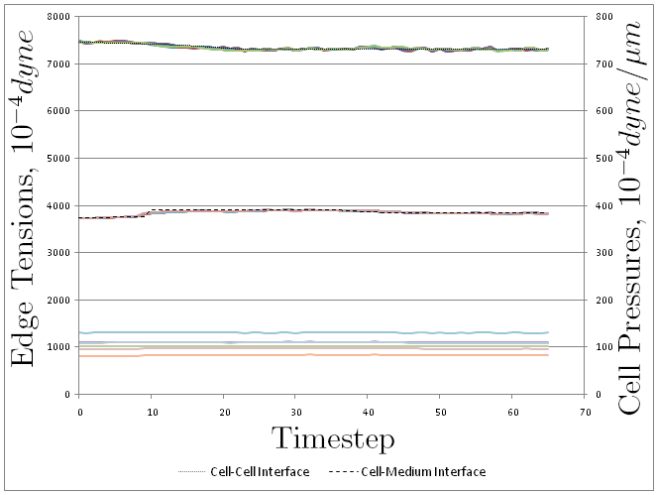

(b) Variable Tension - $\lambda = 0.65$

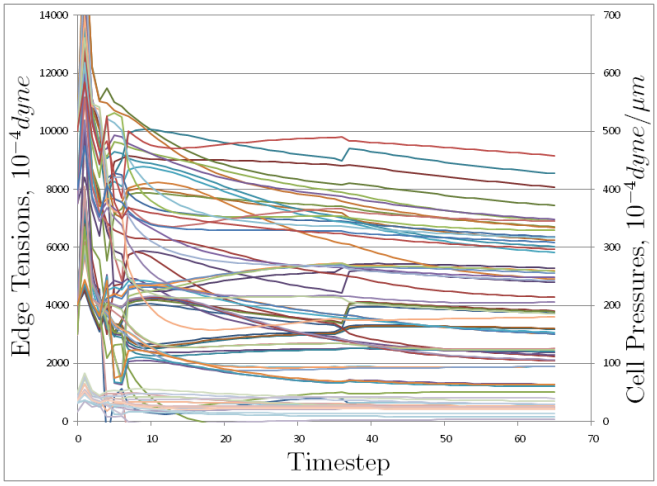

(c) Sorting - VFF: $\beta = -0.1$

Figure 4.11: Basic algorithm output using optimal RLS tuning factor

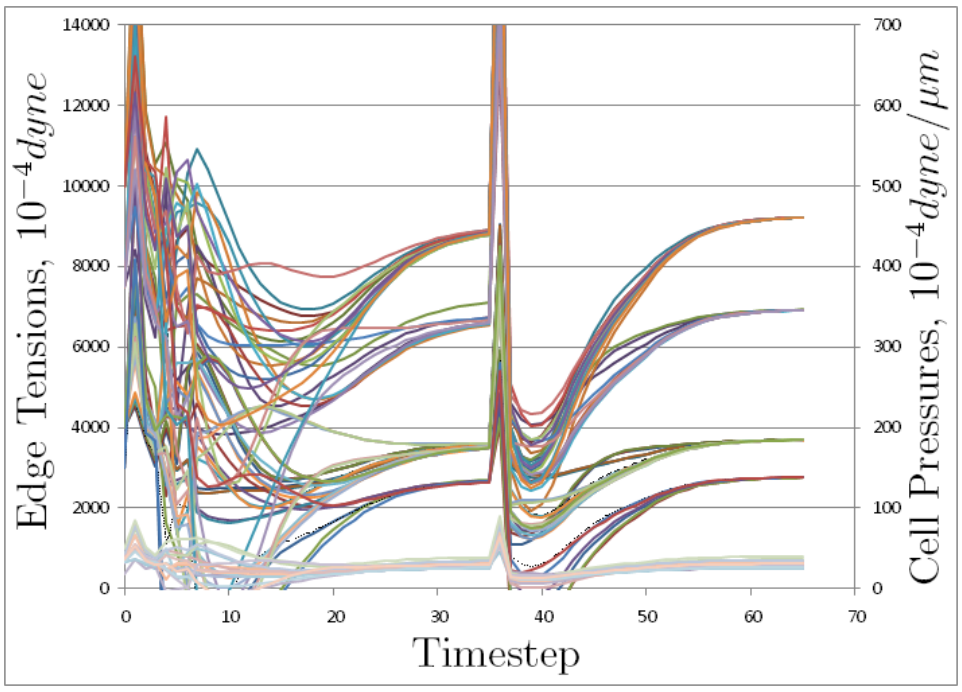

Figure 4.12: Basic algorithm output for the Sorting patch with constant $\lambda = 0.65$. These estimates appear better than what the performance measures indicate.

measures are examined more closely in the following sections discussing how the identification algorithm copes with noise and patches with frayed boundaries, both of which are of far greater concern this algorithm is to be used with live data.

Perhaps most concerning about the results in Table 4.3 is the apparent lack of correlation between χ^2 and the other performance measures. The correlation is good for the 3-Cell patch, but less well correlated for the other two.

It can be concluded that the basic identification algorithm – that including the elements from §3.1-3.3 – does estimate tensions and pressures in patches of cells generated synthetically. Though subject to solver noise, the means of these estimates tracked the correct values very well. RLS solution methods with either constant or variable FF are able to reduce the effects of the output solver noise. Furthermore, there exists some correlation between the χ^2 measure of estimated vs. expected values, and the ψ and R^2 performance measures developed in §4.1. The correlation is discussed further in the subsequent §4.4 and §4.6, in the hopes that they can be of use in future live-data studies.

4.4 Effects of Noise

As was shown in §3.4, the identification algorithm is extremely sensitive to noise corrupting the input nodal coordinates and displacements. In this section, two methods for reducing the effects of this input noise are explored: smoothing, and

Table 4.4: Average performance measures for smoothed noise corrupted input

Input Patch	O_S	W_S	r_{RMS}	ψ	R^2	χ^2
	—	—	502	2.76e10	0.888	2.00e7
	2	15	68.9	1.44e9	0.883	7.46e5
	2	21	47.8	7.39e8	0.878	2.66e5
	2	31	31.6	4.62e8	0.882	1.62e5
3-Cell	2	41	23.6	**3.73e8**	0.893	**1.61e5**
	3	15	70.6	1.46e9	0.873	5.50e5
	3	21	48.1	8.16e8	0.882	3.55e5
	3	31	31.2	4.41e8	0.891	1.81e5
	3	41	**23.4**	4.00e8	**0.900**	2.15e5
	—	—	699	2.03e9	0.896	1.04e7
	2	15	109	1.56e9	0.907	6.36e5
	2	21	74.8	1.46e9	0.933	4.56e5
Variable	2	31	52.8	1.24e9	0.954	3.94e5
Tension	2	41	**45.5**	1.29e9	0.956	1.79e5
	3	15	105	1.95e9	0.921	1.20e6
	3	21	89.0	1.83e9	0.935	3.58e5
	3	31	69.2	1.36e9	0.950	6.38e5
	3	41	47.6	**8.66e8**	**0.962**	**1.74e5**

the same RLS-FF solution method used to reduce output solver noise in §4.3. Following that, a combination of smoothing and RLS-FF was tested for reducing the effects of input noise.

Nodal co-ordinates for the input patches were corrupted with Gaussian white noise with a standard deviation $\sigma = 0.002\epsilon_0$, where ϵ_0 is given by Eq. (3.12). Given the issues with the sorting patch in §4.3, only the 3-Cell and Variable Tension patches will be tested in this section.

4.4.1 Smoothing

In §3.5.2, a method to smooth the input nodal co-ordinates was developed to reduce the effects of input noise. Shown in Table 4.4 are the performance measures for both the 3-Cell and Variable Tension patch using several different tuning factors for the smoothing filter. The performance measures for both patches without any smoothing applied are shown with '—' in the O_S (smoothing order) and W_S (window size) columns for comparison. Again, the best value for each performance measure for each patch is shown in bold face.

One can see good agreement between the various performance measures for the 3-Cell patch, the tuning factors which r_{RMS} and R^2 indicate are optimal had the second best values of ψ and χ^2. For the variable tension patch, the second best value for r_{RMS} corresponds to the optimal runs as indicated by the other measures.

For both patches larger smoothing window sizes produced better results. The table also shows the results using a smoothing order of either $O_S = 2$ or $O_S = 3$ produce very similar results. For the 3-Cell patch, $O_S = 2$ was slightly better, while for the Variable Tension patch $O_S = 3$ was slightly better. In any case, the difference between the two is negligible. Finally, any set of tuning factors for the smoothing filter yields substantially better results than no smoothing at all.

The algorithm output using the optimal tuning factors for the smoothing filter from Table 4.4 are shown, for the 3-Cell patch in Figure 4.13(a), and for the Variable Tension patch in Figure 4.14(a)

Figure 4.13(a) does not show the full 400 available timesteps, however, even from the 75 steps shown one can see that the quality of the estimate degrades quickly. Even though the performance measures may indicate that a particular set of tuning factors produces the best output for a particular patch, that output may still be highly inaccurate. It is clear that all measures excepting the r_{RMS} indicate that the estimate is substantially better at earlier timesteps.

Turning to the Variable Tension patch, whose output and performance are found in Figure 4.14, there is a region between timesteps 10 and 20 where the estimates do match up with the correct values for both the cell-cell and cell-medium interfaces. Looking closer at the plots of the performance measures, we see that R^2 primarily, but also the r_{RMS} and the ψ measures though to a lesser extent, do indicate a better quality estimate over those timesteps. This assertion is confirmed by χ^2.

A problem arises in that there are other timesteps where the several performance measures suggest that estimate is as good as timesteps 10–20, a suggestion not borne out by looking qualitatively at the algorithm output. This effect is similar to observations made with Anscombe's quartet, where four dramatically different sets of data yield identical regression statistics. The example is often used to stress the importance of physically looking at the data, and not simply relying on one's analyses [1, 84].

4.4.2 Recursive Least Squares

Another technique available to reduce the effects of input noise is the RLS solution method with either constant or variable FF. Table 4.5 shows the average performance measure for the 3-Cell and Variable Tension patches with the various (V)FF. If, for a particular row in the table, there is a value in the column λ, then that run was done using a constant FF using that value. If, on the other hand, there is a value in the column β, then that run was done using a variable forgetting factor (VFF), with that value as the adaptation speed in the VFF formulation Eq. (3.16). The performance measures for both patches without (V)FF applied are shown with '—' in the λ and β columns for comparison. The best value for each measure for each patch is shown in bold face.

From the table, it is unclear as to whether RLS-(V)FF improved the performance of the algorithm when the input was corrupted by noise. The output, χ^2

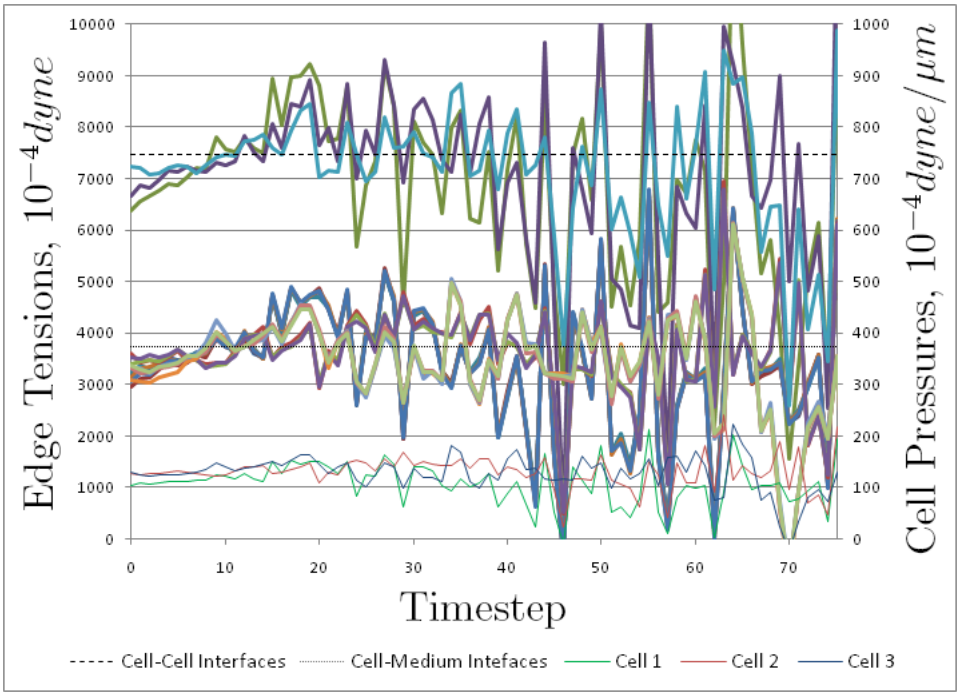

(a) Identification algorithm output

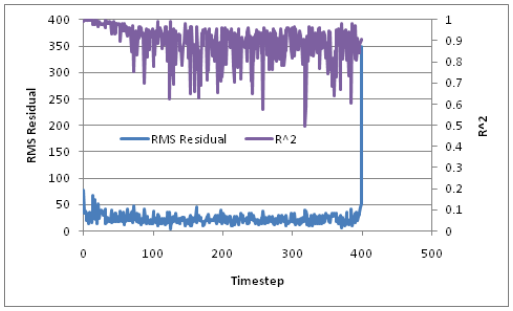

(b) r_{RMS} and R^2 performance measures

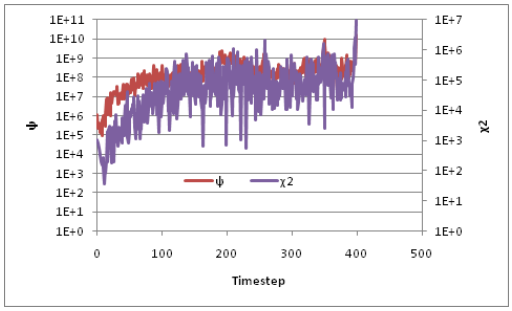

(c) ψ and χ^2 performance measures

Figure 4.13: Output and performance of noise corrupted 3-Cell patch with optimal smoothing $O_S = 2$ and $W_S = 41$

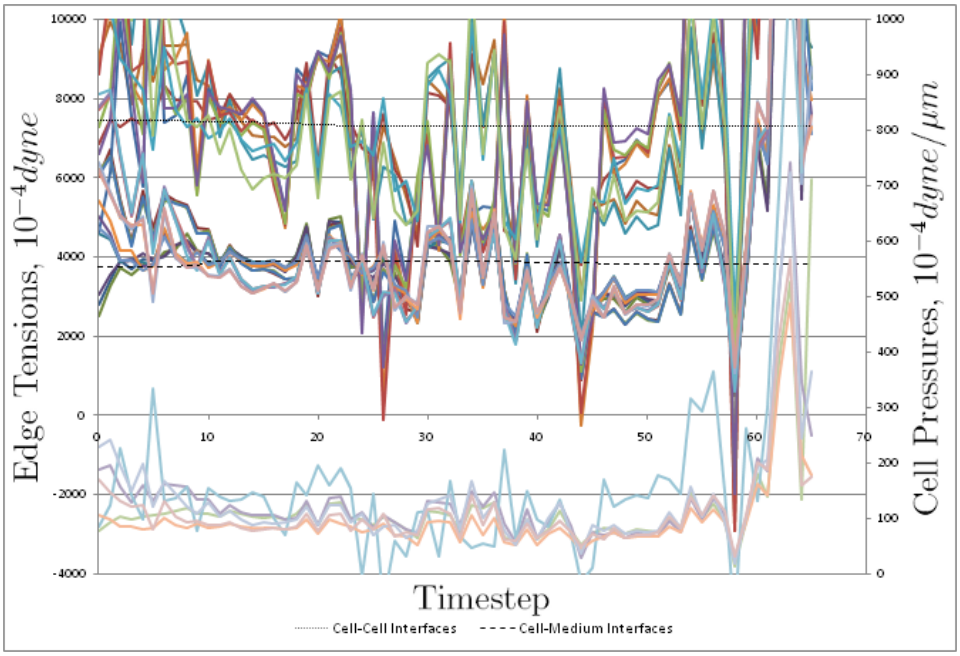

(a) Identification algorithm output

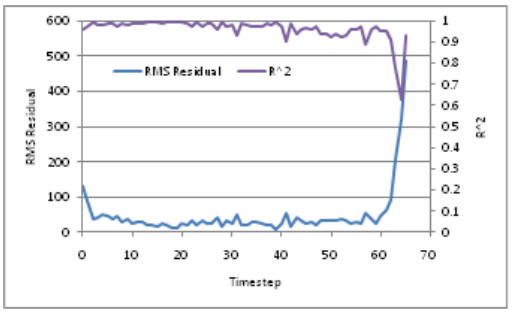

(b) r_{RMS} and R^2 performance measures

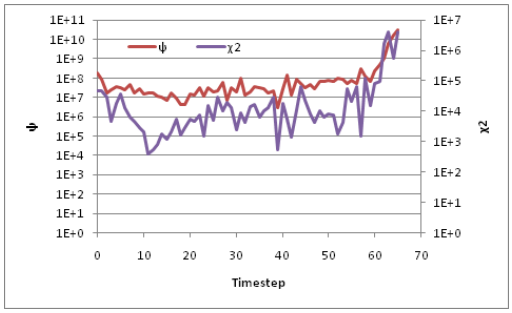

(c) ψ and χ^2 performance measures

Figure 4.14: Output and performance of noise corrupted Variable Tension patch with optimal smoothing $O_S = 3$ and $W_S = 41$

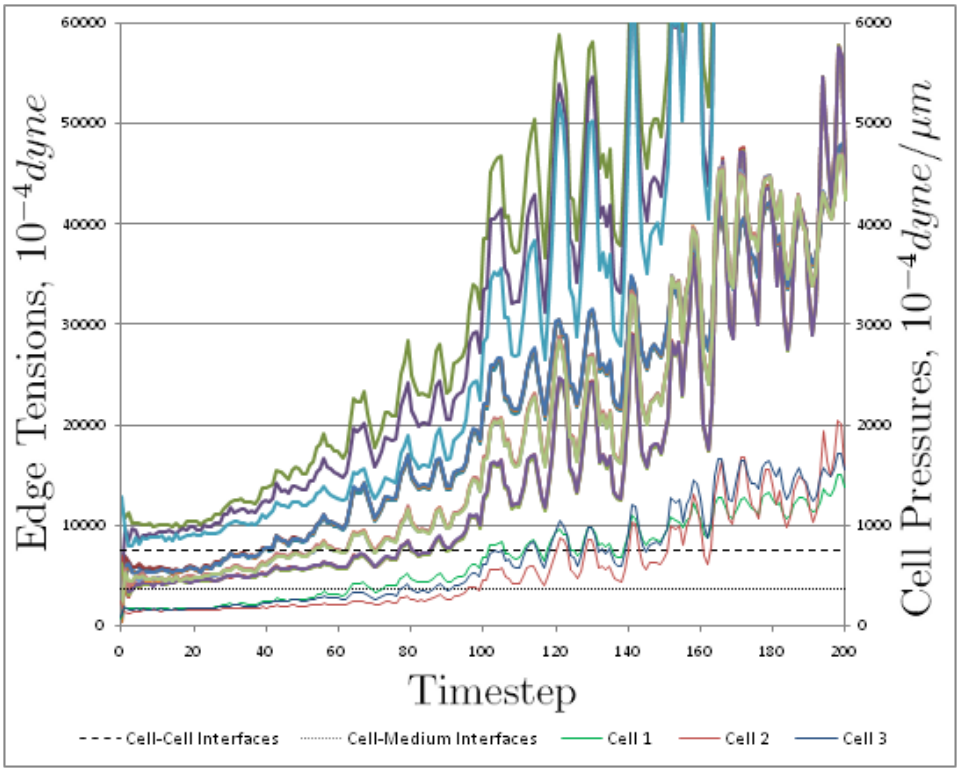

(a) Identification algorithm output

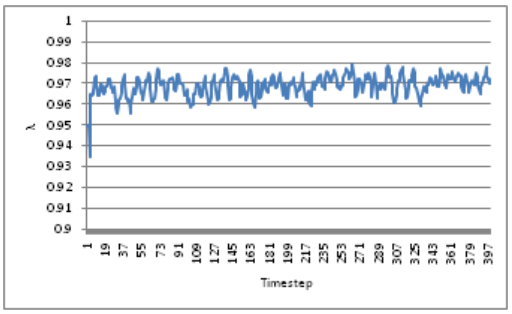

(b) Forgetting Factor, λ

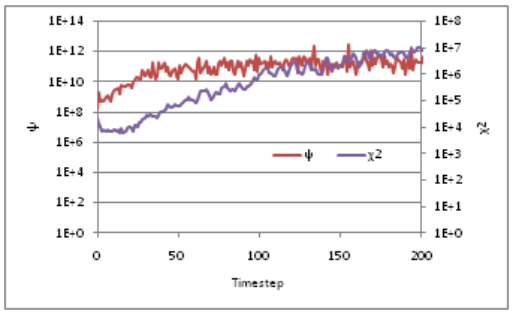

(c) ψ and χ^2 performance measures

Figure 4.15: Output, performance, and FF of noise corrupted 3-Cell patch with optimal RLS-VFF: $\beta = -0.01$

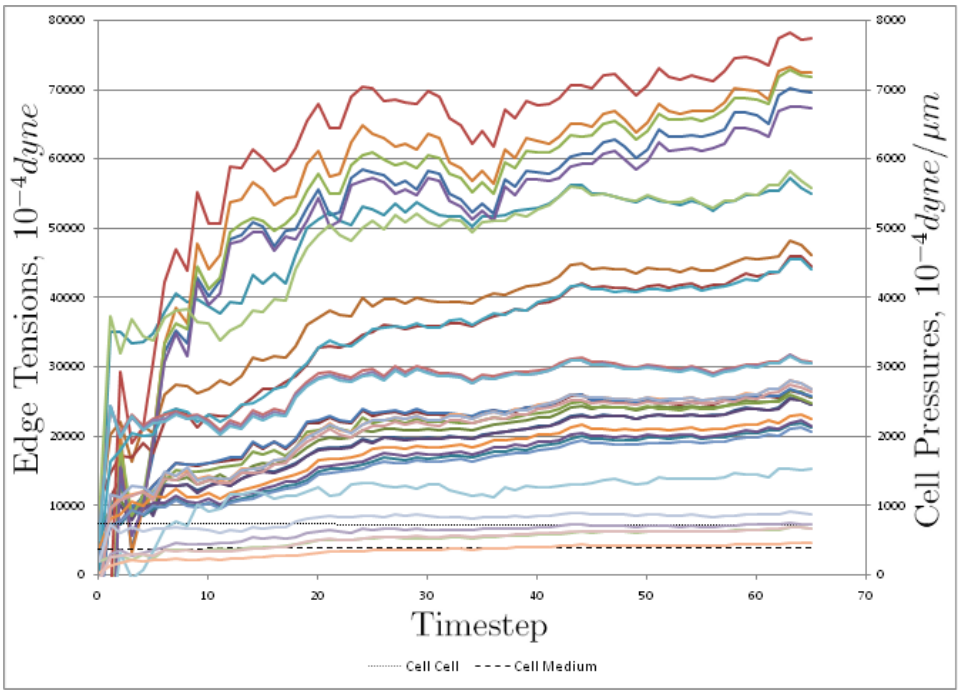

(a) Identification algorithm output

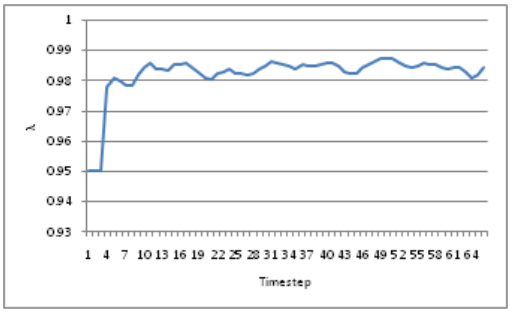

(b) Forgetting Factor, λ

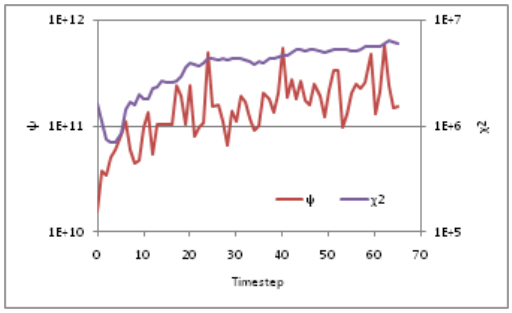

(c) ψ and χ^2 performance measures

Figure 4.16: Output, performance, and FF of noise corrupted Variable Tension patch with optimal RLS-VFF: $\beta = -0.01$

Table 4.5: Average performance measures for noise corrupted input with RLS-(V)FF

Input Patch	λ	β	r_{RMS}	ψ	R^2	χ^2
	—	—	**502**	2.76e10	**0.888**	2.00e7
	0.95	—	1.43e3	6.38e11	0.225	7.33e6
	0.65	—	1.22e3	2.05e11	0.406	1.12e7
3-Cell	0.5	—	1.16e3	1.58e11	0.483	1.21e7
	—	-0.01	1.47e3	2.86e11	0.193	**6.26e6**
	—	-0.1	1.28e3	2.19e11	0.369	1.14e7
	—	-1	522.	**4.92e9**	0.887	1.51e7
	—	—	**699**	**2.03e9**	**0.896**	1.04e7
	0.95	—	1.99e3	1.91e11	0.162	5.48e6
Variable	0.65	—	1.84e3	1.64e11	0.363	1.66e7
Tension	0.5	—	1.70e3	2.83e11	0.463	1.82e7
	—	-0.01	2.05e3	1.71e11	0.138	**3.95e6**
	—	-0.1	1.97e3	2.41e11	0.215	1.05e7
	—	-1	931	4.70e9	0.825	9.76e6

and ψ performance measures, and VFF for the runs with the best χ^2 are shown for each patch in Figure 4.15 and Figure 4.16. Higher values of β than those shown in the table were found to produce no variation in the FF whatsoever, and the algorithm returned the same results as when the basic algorithm was used to produce the top rows shown for each patch.

Figure 4.15 shows that the use of RLS with the VFF shown in (b) does, at least at earlier steps, reduce the effects of input noise on the identification algorithm. There is good correlation between the two performance measures shown in (c); both indicate the quality of the estimate degrades at later timesteps. It is not known why the estimate increases over time. The increase was so severe, that only the first 200 timesteps are plotted.

The output in Figure 4.16(a) is not as definitive as that of the 3-Cell patch. The estimates even at early timesteps are significantly higher than the correct values. The algorithm did, at least, yield estimates which grouped cell-cell and cell-medium interface tensions together, even though the values of the estimates are far too high. The performance measures χ^2 and ψ are well correlated, and support the observation that the estimate is of higher quality earlier in the history of the patch. One can also see that the FF is higher for the Variable Tension patch than it was for the 3-Cell patch (Figure 4.15(b)) over the entire history. Given that the update law for λ – Eq. (3.16) – is based on prediction error, higher values of λ could suggest that the identification algorithm had difficulty in producing acceptable estimate.

We can conclude then, that the use of the RLS-VFF solution method can improve the estimates of edge tension and cell pressure when inputs are corrupted by noise, and that such improvement is concentrated in earlier timesteps rather than later ones. More importantly, the performance measure ψ is well correlated with

χ^2 for noise corrupted inputs. Finally, when using VFF, it appears as though the history of the FF itself can yield useful information about estimate quality, so long as consistent β is used for each run. It is unclear as to why the estimates increase over time. This surprising result is clearly worthy of further investigation.

4.4.3 Smoothing and Recursive Least Squares

Having shown that both smoothing and RLS-VFF can have positive effects on algorithm output when the inputs are corrupted by noise, both methods are implemented concomitantly, to see if estimates can be further improved. The 3-Cell and Variable Tension patches, corrupted by input noise, were run with the best tuning factors for the smoothing filter and RLS-VFF solution method as determined in §4.4.1 and §4.4.2.

Figure 4.17 shows the algorithm output for the 3-Cell patch, as well as r_{RMS} and ψ performance measures plotted against χ^2. A smoothing order of $O_S = 2$ and window size of $W_S = 41$ were used, along with the adaptation speed $\beta = -0.01$ for the VFF update. One can immediately see that the combination of both smoothing and RLS-VFF has radically improved the estimate. Thought the estimated values are slightly lower than the correct parameter values, the algorithm performed much better when both methods were used to reduce the effects of input noise.

Both Figure 4.17(b) and Figure 4.17(c), do not show good correlation of the performance measures with χ^2. This is somewhat troubling; since the combination of smoothing and RLS-VFF will be used in future studies to reduce the effects of input noise for live data, and since χ^2 will not be available when using live data, the lack of good correlation reduces confidence when these performance measures are used to assess the quality of any live data-based estimates. In fact, both the r_{RMS} and ψ suggest that the estimates are better in the last 25 or so timesteps, when in fact, χ^2 shows this region to be of lowest quality.

Figure 4.18 shows the algorithm output for the Variable Tension patch, as well as r_{RMS} and ψ performance measures plotted against χ^2. $O_S = 3$ and $W_S = 41$ were used, along with the adaptation speed $\beta = -0.01$ for the VFF update. In Figure 4.18(a), especially at later timesteps, the estimates appear to converge nicely to the correct values for tension and pressure. Though the algorithm did not perform as well for this patch is it did for the 3-Cell patch, the combination of smoothing and RLS-VFF does dramatically reduce the effects of input noise when compared with either smoothing or RLS-VFF alone.

Again with the Variable Tension patch, the lack of correlation between the performance measures and χ^2 is apparent. This shortcoming will need to be addressed in future live-data studies.

We can conclude that a combination of smoothing with a large window size, and a RLS-VFF solution method with slow adaptation (low β) are highly effective at reducing the effects of input noise on the identification algorithm. This section

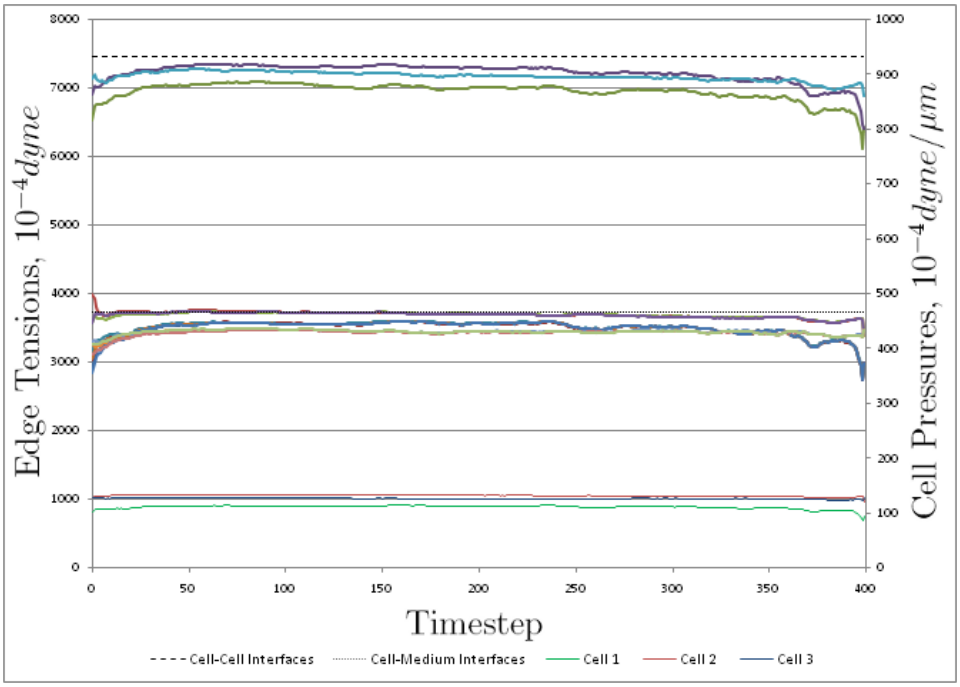

(a) Identification algorithm output

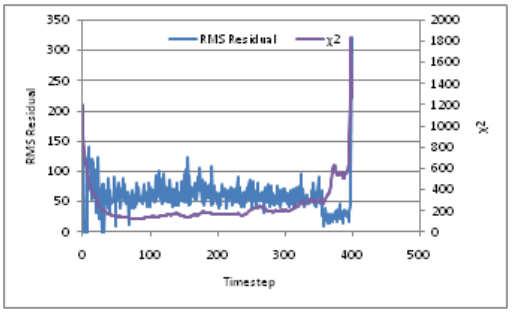

(b) r_{RMS} and χ^2 performance measures

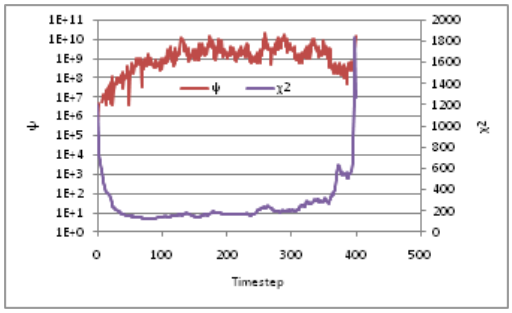

(c) ψ and χ^2 performance measures

Figure 4.17: Output and performance of noise corrupted 3-Cell patch with optimal optimal smoothing $O_S = 2$ and $W_S = 41$, RLS-VFF: $\beta = -0.01$

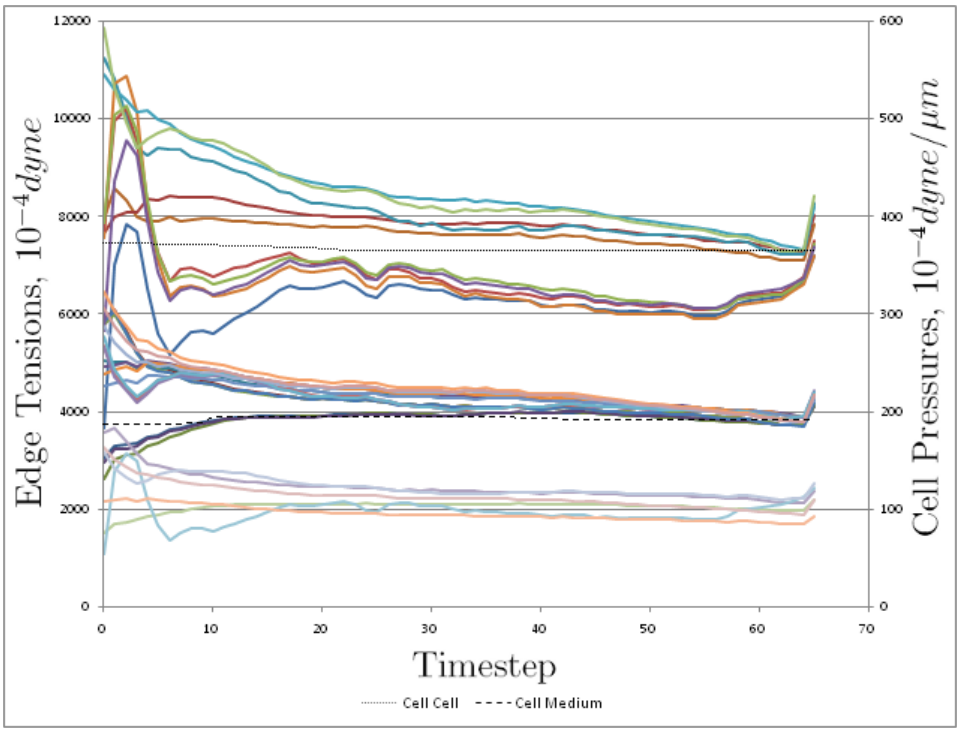

(a) Identification algorithm output

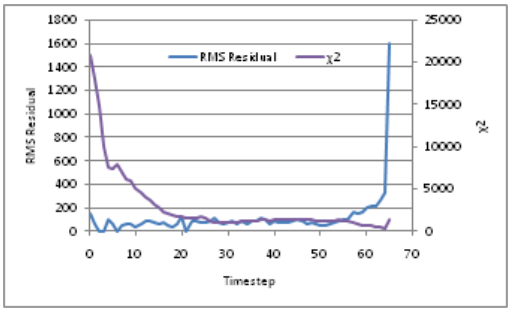

(b) r_{RMS} and χ^2 performance measures

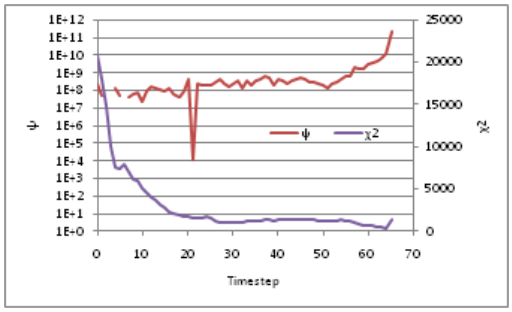

(c) ψ and χ^2 performance measures

Figure 4.18: Output and performance of noise corrupted Variable Tension patch with optimal optimal $O_S = 2$ and $W_S = 41$, RLS-VFF: $\beta = -0.01$

has revealed some issues with the performance measures used, namely that neither r_{RMS} nor ψ appear well correlated with χ^2, which directly measures deviations from the expected values of the estimated parameters. The performance measures may still be useful to compare the quality of estimates made with different tuning factors, but statements regarding estimate quality at a certain timestep in a given run may not be as reliable when inputs are corrupted by noise and both smoothing and RLS-VFF are employed.

4.5 Validation of Non-Causal Forgetting Factors

In §3.7, an augmented system of equations and used a non-causal forgetting factor was constructed to combine information from neighbouring timesteps in arriving at a solution. At the time, the only justification given was to reduce estimator bias when parameters were changing monotonically. Now, a comparison between causal (back-looking) and non-causal (forward- and back-looking) RLS-FF is presented, using the 3-Cell patch and χ^2 to measure the accuracy of the estimates. That comparison is shown in Table 4.6. If, on the other hand, there is a value in the column β, then that run was done using a variable forgetting factor (VFF), with that value as the adaptation speed in the VFF formulation Eq. (3.16). Values greater than unity in the 'Improvement Ratio' column indicate the the non-causal approach is better.

Table 4.6: Comparison of estimate accuracy using causal and non-causal FF solution methods. 3-Cell patch using χ^2 as a measure of accuracy.

λ	β	Causal	Non-Causal	Improvement Ratio
0.95	—	2.34	3.33	0.703
0.65	—	**17.9**	**2.23**	**8.03**
—	-0.01	3.49	3.75	0.931
—	-0.1	3.49	3.75	0.931
—	-1	3.49	3.66	0.954
—	-10	2.07	2.08	0.995
—	-100	**2.74**	**0.623**	**4.40**

The table shows that in most cases the estimates made using the non-causal approach are very close those made using the causal approach. In other cases, such as the two runs set in bold face, the non-causal approach yields estimates that are closer to the expected values by a large margin. The two cases above yielded estimates that were better by factors of 4 and 8 respectively when compared to estimates made using the causal approach. This justifies the use of the non-causal FF in the identification algorithm.

Table 4.7: Average performance measure for the frayed boundary sub-patch

λ	β	r_{RMS}	ψ	R^2	χ^2
0.95	—	20.7	2.04e7	**0.916**	1.99e3
0.65	—	**18.9**	1.87e7	0.911	2.10e3
—	-0.01	23.8	2.84e7	0.854	**110**
—	-0.1	23.8	2.84e7	0.854	**110**
—	-1	23.7	2.84e7	0.854	**110**
—	-10	20.5	2.10e7	0.907	1.16e3
—	-100	19.0	**1.86e7**	0.912	2.08e4

4.6 Patches with Frayed Boundaries

One of the most critical aspects of the identification algorithm if it is ever to be used with live data is the capacity to handle patches with frayed boundaries. As discussed in §3.7, the patch with frayed boundaries, or sub-patch, is treated as having unknown forces in x and y at each node on the sub-patch boundary; these unknown boundary forces are included along with the unknown tensions and pressures, and the augmented system, described by Eq. (3.18) and Eq. (3.19), is solved using a QR factorisation.

This aspect of the algorithm is tested using the familiar 3-Cell patch shown in Figure 4.1 but with additional concentrated loads at nodes 0, 1, 7, 9, and 10. These additional forces cause the final configuration of the patch to differ from that shown in Figure 4.1b), but only slightly. Also, there are only 150 timesteps in this patch.

The structure of the sub-patch problem requires the use of the RLS-(V)FF solution method. Shown in Table 4.7 are the average performance measures for several different constant and variable FF. Where a value is present in the λ column, that run used a constant FF; where a value is present in the β column, that run used a VFF. The best value for each performance measure is shown in bold face.

None of the performance measure averages agree with χ^2 as to which tuning factor produced the best estimate. In this case, it appears that averages will be inadequate for comparisons between runs, except to say that values of β between -0.01 and -1 give very similar results. The algorithm output $\lambda = 0.95$ and VFF runs with $\beta = -1$ and $\beta = -10$ are shown in Figure 4.19. The performance measures for these runs are shown in Figure 4.20.

One can see by looking at the algorithm output, and Figure 4.20(c) that a VFF with $\beta = -1$ produced the best estimates for tensions and pressures. Full plots of ψ and R^2 bear out the lack of correlation between these measures and χ^2 that was suggested by the average values presented in Table 4.7. r_{RMS} was omitted from these plots since it has been shown in previous sections that r_{RMS} tends to report how far the estimate deviates from the simple LS fit, and not how good or bad the estimate itself is.

It should be stated that $\beta = -1$ did not produce much variation in the FF;

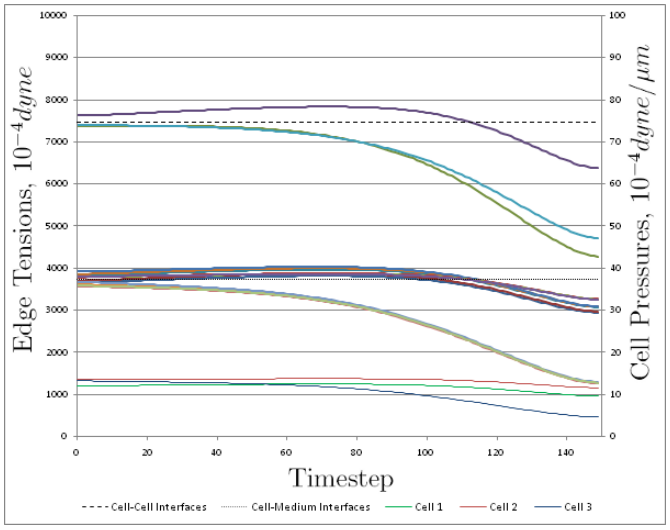

(a) $\lambda = 0.95$

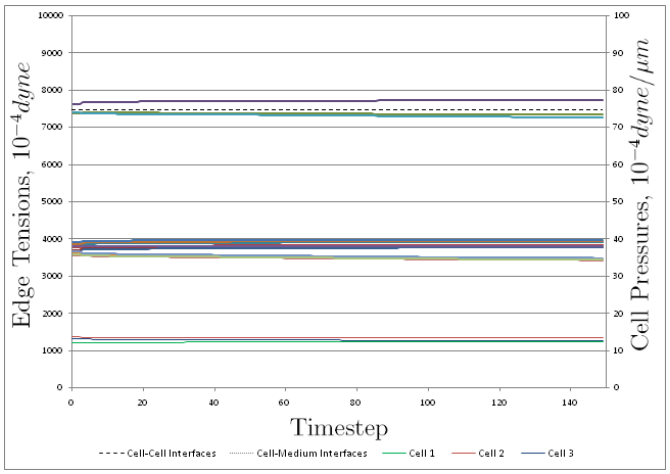

(b) VFF: $beta = -1$

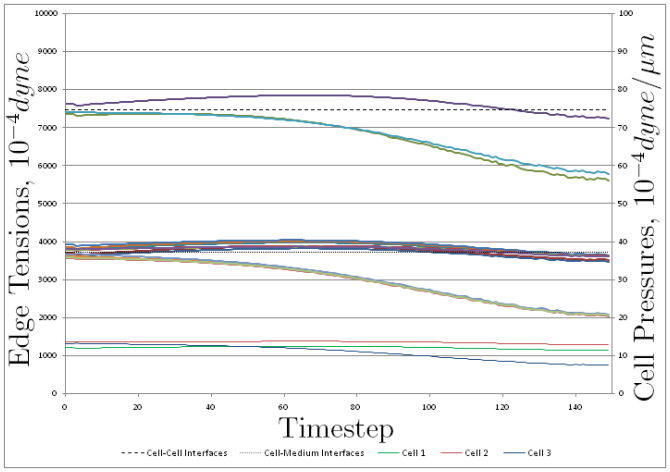

(c) VFF: $\beta = -10$

Figure 4.19: Output for the sub-patch with frayed boundaries and differing (V)FF

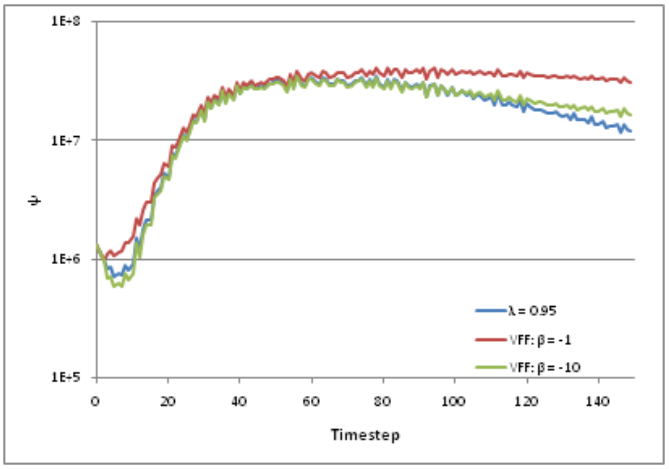

(a) ψ

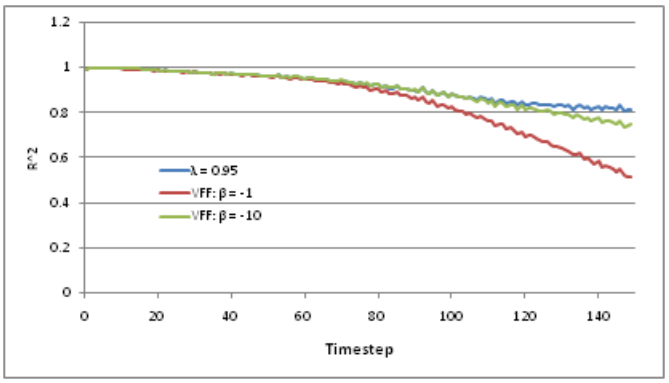

(b) R^2

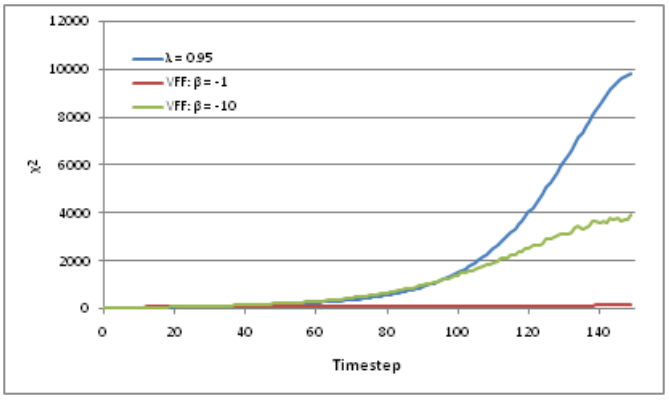

(c) χ^2

Figure 4.20: Performance measures for the sub-patch with frayed boundaries and differing (V)FF

in fact, λ had a nearly constant value of 0.99 throughout the run shown in Figure 4.19(b). A constantly high FF like this is biased toward producing good results for constant parameters as is the case with the test patch used here. In the case of live data, it cannot be assumed that parameters are constant, and should the VFF update produce consistently high λ such as occurred here, the estimate may be unduly drawn toward a constant value. We will have to take care in selecting values for β and interpreting the results with live data.

4.6.1 Frayed Boundaries with Noise

Because meshes extracted from live data will necessarily be subject to input error, the analyses of the previous section were repeated using the same frayed boundary sub-patch but with Gaussian white noise added to the nodal co-ordinates. As in §4.4, the corrupting noise has $\sigma = 0.002\epsilon_0$, where ϵ_0 is calculated according to Eq. (3.12).

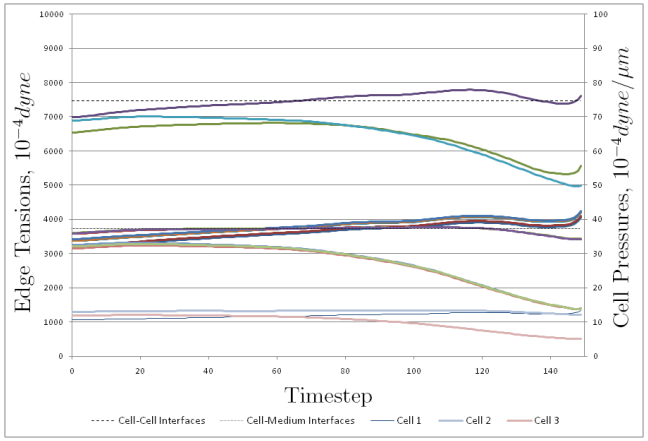

(a) $\lambda = 0.95$

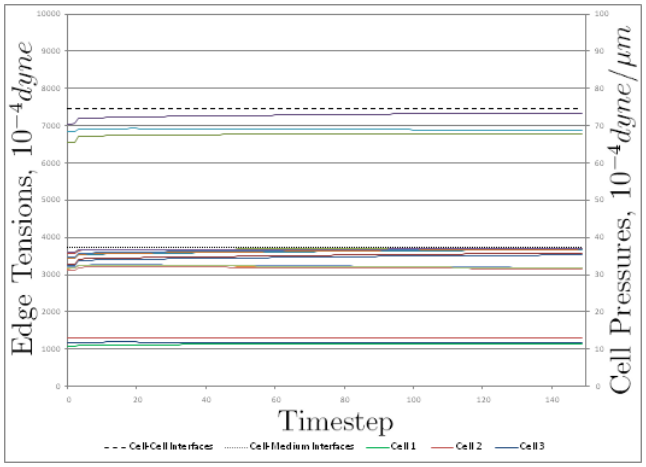

(b) VFF: $\beta = -0.1$

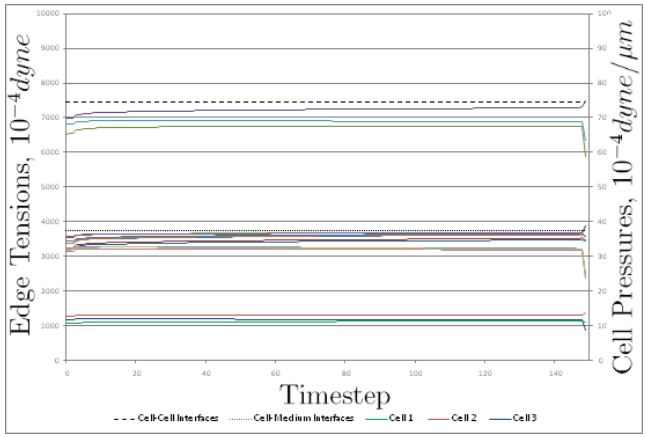

(c) VFF: $\beta = -1$

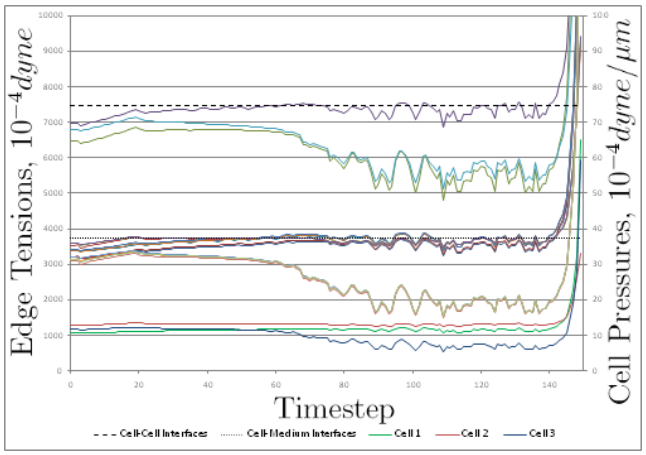

(d) VFF: $\beta = -10$

Figure 4.21: Output for the noise corrupted sub-patch with frayed boundaries and differing (V)FF

The tuning factors determined to be optimal for noise reduction in §4.4.1 were used, along with different constant and variable FF. As the sub-patch is based on the 3-Cell patch, these were a smoothing order $O_S = 2$, and a window size $W_S = 41$. The algorithm output is shown in Figure 4.21, and the performance measures are shown in Figure 4.22.

One can see from Figure 4.21 that VFF with $\beta = -0.1$ and $\beta = -1$ yield estimates which are quite close to the correct parameter values. The other two plots – $\lambda = 0.95$ and VFF with $\beta = -10$ – also yield very good estimates, but not as close to the expected values as the runs mentioned previously. This observation is borne out by Figure 4.22(c). The χ^2 histories for the $\lambda = 0.95$ and VFF with $\beta = -10$ runs still indicate a very good fit. It is difficult to say anything definitive based on the ψ or R^2 performance measures. They do, however, indicate that the quality of the estimates degrades at later timesteps, which agrees with both the χ^2 plots and qualitative assessment of the algorithm output. In all cases, the estimates are slightly lower than the expected values. the cause of the low estimates is not known at this time.

We can conclude that the identification algorithm is quite capable of estimating tensions and pressures in sub-patches with frayed boundaries, even when the inputs are noise corrupted. The synthetic data used in this section were designed to simulate as closely as possible those aspects of live data with which identification algorithm must cope and, following the discussion above, we can say that the algorithm is ready to be tested with live data.

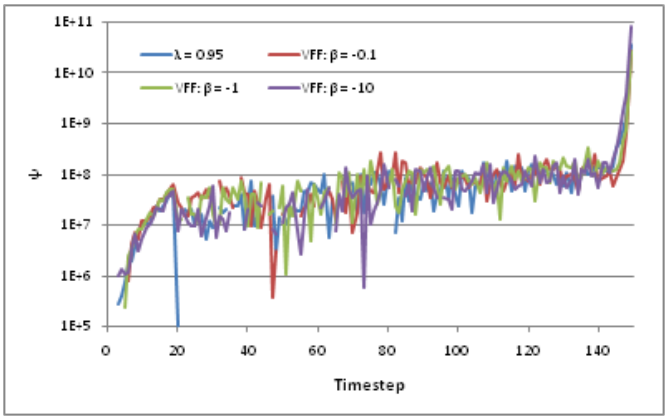

(a) ψ

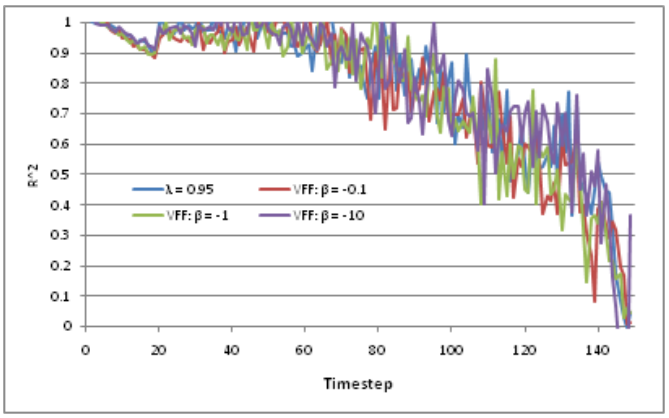

(b) R^2

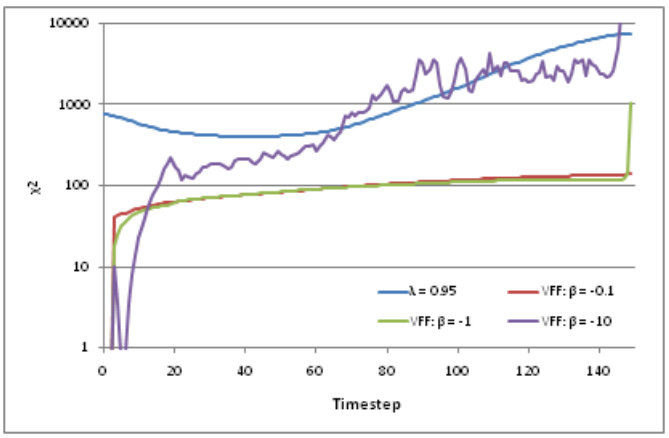

(c) χ^2

Figure 4.22: Performance measures for the noise corrupted sub-patch with frayed boundaries and differing (V)FF

Chapter 5

Conclusions and Recommendations

The purpose of this thesis was to develop an algorithm to identify forces driving the self-rearrangement of cells in biological tissues. Large strides have been made toward that goal. Using an extant Finite Element (FE) model as a foundation, and implementing Least Squares (LS) estimation methods, an identification algorithm called 'Scar' was developed, and extensively tested using synthetic data.

It was shown that the algorithm yielded very accurate estimates of tensions and pressures driving cellular self-rearrangement in synthetic data. This was shown using a number of different input patches of cells designed to test the algorithms performance on different fronts. Estimates accurately tracked slowly varying edge tensions, as well as abrupt changes arising from neighbour changes over the history of the motion in the patch.

The estimates were found to be subject to output solver noise, arising from the numerically ill-conditioned system of equations, represented as the Geometric matrix used to calculate the parameter estimates. It was shown that using a Recursive Least Squares (RLS) solution method incorporating a Forgetting Factor (FF) reduces the output solver noise. Selection of an appropriate FF is largely dependent on the input patch. To aide with the selection an appropriate FF, a new variable FF was formulated based on prediction error. The VFF was found to produce better estimates of tensions and pressures than a constant FF tried for reducing output solver noise. It is still necessary to select a value for the adaptation speed in the VFF update law.

The sensitivity of the algorithm was assessed by adding Gaussian white noise to the nodal co-ordinates in the synthetic data patches. The ill-conditioned nature of the Geometric matrix means that the algorithm is highly sensitive to errors in the input. It was found that any amount of input error dramatically reduced the quality of the estimates, and that increasing input error produced increasingly poor estimates.

Two approaches were taken to reduce the effects of input errors on the algorithm. A Savitsky-Golay smoothing filter was implemented to smooth the noisy inputs, and the RLS solution method with variable and constant FF was again used. On their own, both smoothing and RLS-(V)FF were shown to reduce the effects of input errors; a combination of both approaches was quite effective at mitigating the effects of input errors. The ability of the algorithm to effectively cope with input errors is necessary for the treatment of live data. It was found that a large smoothing window and a slowly adapting VFF were most effective in reducing the effects of input errors.

With the future treatment of live data in mind, a method to calculate parameter estimates in sub-patches with frayed boundaries was developed. By adding unknown forces at each boundary node in the sub-patch, and combining information from neighbouring timesteps weighted by the exponentially decaying (V)FF. The addition of the unknown boundary forces causes the Geometric matrix for each individual timestep to be underdetermined. Including the neighbouring timesteps' information is not a necessity. For the sub-patch problem, information from neighbouring timesteps in both directions was included, and hence the RLS-(V)FF formulation is non-causal. The non-causal approach was validated experimentally by comparing estimates from the basic algorithm (synthetic data, no noise) for the tradition causal (V)FF and the non-causal (V)FF. In most cases the difference between estimates from the two methods was negligible; in the remaining cases, the non-causal (V)FF performed significantly better.

The identification algorithm produced good estimates of tensions and pressures in the sub-patch both with and without imposed input error. This portion of the algorithm was tested with a synthetic data patch which had concentrated loads placed at several boundary nodes, representing the forces which would have been transfered to the sub-patch from the surrounding tissue. The tuning factors for the smoothing filter were the same as those found to produce the best results in the synthetic data patches tested during the sensitivity analysis. A VFF with moderate adaptation speed was found to produce the best estimates when input errors were included. The synthetic data sub-patch with input error is the closest representation to live data available for algorithm testing.

To assess the effect of the several tuning factors used in the algorithm, three different performance measures were developed and evaluated against the χ^2 hypothesis test for estimated vs. expected values. The RMS residual is closely related to the quantity which the LS method seeks to minimise; as a result, it tends to report deviations from the pure LS fit. In nearly all cases, a FF is used to drive the estimate away from the pure LS estimate, rendering the RMS residual useless in most cases. While some correlation seen between the other two measures – the coefficient of determination and the trace of the covariance matrix – and the hypothesis test, the correlation was sporadic at best.

Several avenues for further research presented themselves during the course of this study. Foremost, further refinement of the algorithm's response to input noise

is needed. The algorithm was tested with a small quantity of input noise compared to noise levels expected to be present in future live data mesh extractions. Robust noise mitigation is absolutely necessary should one seek to obtain meaningful results using live data, the ultimate goal of this project in the long term.

Related to the handling of input noise, general improvement of the algorithm's conditioning is warranted. The Geometric matrix was shown to be ill-conditioned, resulting in significant output solver noise. While RLS solution methods using constant and variable forgetting factors were shown to reduce the output solver noise, improving the mathematical conditioning of the system of equations would see improvements in the estimates in all cases.

Expansion of these techniques to three spatial dimensions is recommended. It can be shown that the 3D case does not result in under-conditioned systems of equations when treating the sub-patch problem. This property removes the restriction seen in the 2D case for the sub-patch problem, namely that either causal or non-causal forgetting factors (FF) are necessary to reach a solution.

The χ^2 hypothesis test directly measures the deviation of the estimate from the expected values, which are available for synthetic data. In treating live data, the expected parameter values are not available. Further investigation is needed into performance measures which correlate well with the hypothesis test for synthetic data, so as to be more reliable as a measure of how well the algorithm estimates tensions and pressures from live data.

The algorithm makes use of a number of tuning factors at the various steps of the solution, such the initial value of the FF, the speed of adaptation in the VFF update law, the smoothing order and window size, and others besides. Following some of the improvements suggested above, a rigorous parametric study to determine optimal values for these tuning factors should be undertaken with a number of different input patches. To assess the suitability of specific tuning factors for use with live data, improvement of the performance measures is a necessity.

Implementing a Singular Value Decomposition (SVD) in the identification algorithm should be explored. The SVD can be used to improve the numerical conditioning of linear systems, especially those whose inputs are corrupted by noise. SVD is also more stable computationally than the QR decomposition used currently.

As work progresses more toward live data applications for this algorithm, it would be beneficial to improve current mesh extraction techniques to reduce input errors. Furthermore, better characterisation of the nature of the input errors could lead to more sophisticated methods to reduce its impact on the final estimates. Even so, the method in its current form seems suitable for application to live data.

The identification algorithm presented here has the potential to grant new insights into the developing embryo, especially when applied to data live real embryos. Positive results with live data would provide strong support for the DITH based FE model upon which the new algorithm is based. But perhaps most importantly, success with live data would remove the need to engage in long and tedious trial-and-error methods to tune computational models to live observations; for the first

time it may be possible to measure the forces driving cellular self-rearrangement directly and in a non-invasive and non-destructive manner, and with a level of refinement never before seen.

References

[1] F. J. Anscombe. Graphs in statistical analysis. *American Statistician*, 27:17–21, 1973. 66

[2] ASTM. Standard E837-08e1, "Standard test method for determining residual stresses by the hole-drilling strain-gage method", 2008. 10

[3] M. Bellanger. *Adaptive digital filters and signal analysis*. M. Dekker, New York, 1987. 23

[4] L. V. Beloussov. *The Interplay of Active Forces and Passive Mechanical Stresses in Animal Morphogenesis*. NATO ASI series. Series H, Cell biology. Springer-Verlag, Berlin ; New York, 1994. 4, 5, 7, 10, 11, 12, 13

[5] L. V. Beloussov. *The dynamic architecture of a developing organism: an interdisciplinary approach to the development of organisms*. Kluwer Academic Publishers, Dordrecht, 1998. 5, 7, 9

[6] G. W. Brodland. The differential interfacial tension hypothesis (DITH): A comprehensive theory for the self-rearrangement of embryonic cells and tissues. *Journal of Biomechanical Engineering*, 124(2), 2002. 1, 10

[7] G. W. Brodland. Computational modeling of cell sorting, tissue engulfment, and related phenomena: A review. *Applied Mechanics Reviews*, 57(1):47–76, 2004. 1

[8] G. W. Brodland, D. I. L. Chen, and J. H. Veldhuis. A cell-based constitutive model for embryonic epithelia and other planar aggregates of biological cells. *International Journal of Plasticity*, 22(6):965–995, 2006. 12, 13

[9] G. W. Brodland and H. H. Chen. The mechanics of cell sorting and envelopment. *Journal of Biomechanics*, 33(7):845–851, 2000. 1, 10, 13, 16

[10] G. W. Brodland and H. H. Chen. The mechanics of cell sorting and envelopment. *Journal of Biomechanics*, 33(7):845–851, 2000. 13

[11] G. W. Brodland, D. Viens, and J. H. Veldhuis. A new cell-based fe model for the mechanics of embryonic epithelia. *Computer Methods in Biomechanics and Biomedical Engineering*, 10(2):121, 2007. 1, 13, 15, 17

[12] X. Chen and G. W. Brodland. Multi-scale finite element modeling allows the mechanics of amphibian neurulation to be elucidated. *Physical Biology*, 5(1):15003, 2008. 1, 8, 13

[13] M. G. Chown and S. Kumar. Imaging and manipulating the structural machinery of living cells on the micro- and nanoscale. *International Journal of Nanomedicine*, 2(3):333–344, 2007. 11

[14] D. A. Clausi and G. W. Brodland. Mechanical evaluation of theories of neurulation using computer simulations. *Development*, 118(3):1013–1023, 1993. 8, 13, 17, 33

[15] J. Colombelli, E. G. Reynaud, J. Rietdorf, R. Pepperkok, and E. H. K. Stelzer. In vivo selective cytoskeleton dynamics quantification in interphase cells induced by pulsed ultraviolet laser nanosurgery. *Traffic*, 6(12):1093–1102, 2005. 11

[16] J. E. Cooper and K. Worden. On-line physical parameter estimation with adaptive forgetting factors. *Mechanical Systems and Signal Processing*, 14(5):705–730, 2000. 24

[17] A. O. Cordero and D. Q. Mayne. Deterministic convergence of a self-tuning regulator with variable forgetting factor. *IEE Proceedings D (Control Theory and Applications)*, 128(1):19–23, 1981. 24

[18] M. F. Coughlin and D. Stamenovic. A tensegrity structure with buckling compression elements: Application to cell mechanics. *Journal of Applied Mechanics-Transactions of the ASME*, 64(3):480–486, 1997. 12

[19] S. C. Cowin and S. B. Doty. *Tissue mechanics*. Springer, New York, 2006. 4, 5, 7, 12, 13

[20] J. Dai and M. P. Sheetz. Mechanical properties of neuronal growth cone membranes studied by tether formation with laser optical tweezers. *Biophysical Journal*, 68(3):988–996, 1995. 7

[21] J. Dai, H. P. Ting-Beall, R. M. Hochmuth, M. P. Sheetz, and M. A. Titus. Myosin I contributes to the generation of resting cortical tension. *Biophysical Journal*, 77(2):1168–1176, 1999. 6, 7

[22] J. W. Dai, H. P. Ting-Beall, and M. P. Sheetz. The secretion-coupled endocytosis correlates with membrane tension changes in rbl 2h3 cells. *Journal of General Physiology*, 110(1):1–10, 1997. 6, 7

[23] L. A. Davidson, A. M. Ezin, and R. Keller. Embryonic wound healing by apical contraction and ingression in xenopus laevis. *Cell Motility and the Cytoskeleton*, 53(3):163–176, 2002. 11

[24] L. A. Davidson, M. A. R. Koehl, R. Keller, and G. F. Oster. How do sea-urchins invaginate - using biomechanics to distinguish between mechanisms of primary invagination. *Development*, 121(7):2005–2018, 1995. 13

[25] L. A. Davidson, G. F. Oster, R. E. Keller, and M. A. R. Koehl. Measurements of mechanical properties of the blastula wall reveal which hypothesized mechanisms of primary invagination are physically plausible in the sea urchin strongylocentrotus purpuratus. *Developmental biology*, 209(2):221–238, 1999. 13

[26] T. A. Davis. *Direct Methods for Sparse Linear Systems*. Society for Industrial an Applied Mathematics, Philadelphia, 2006. 22, 33

[27] P. M. DeRusso, R. J. Roy, C. M. Close, and A. A. Desrochers. *State Variable for Engineers*. John Wiley & Sons, Inc., New York, 1998. 21, 22, 23, 24

[28] C. R. Ethier and C. A. Simmons. *Introductory Biomechanics: From Cells to Organisms*. Cambridge University Press, Cambridge ; New York, 2007. 4, 5, 6, 7, 12

[29] T. R. Fortescue, L. S. Kershenbaum, and B. E. Ydstie. Implementation of self-tuning regulators with variable forgetting factors. *Automatica*, 17(6):831–5, 1981. 24, 41

[30] R. A. Foty and M. S. Steinberg. The differential adhesion hypothesis: a direct evaluation. *Developmental biology*, 278(1):255–263, 2005. 7, 10

[31] C. F. Gauss. *Theoria Combinationis Observationum Erroribus Minimis Obnoxiae*. Societas Regia Scientiarum Gottingensis, Göttingen, 1825. 21

[32] C. F. Gauss. *Theory of the Combination of Observations Least Subject to Errors*. Classics in Applied Mathematics Series. Society for Industrial and Applied Mathematics, Philidelphia, 1995. Translation by G. W. Stewart. 21

[33] J. Glazier and F. Graner. Simulation of the differential adhesion driven rearrangement of biological cells. *Physical Review E*, 47(3):2128–2154, 1993. 12

[34] R. Gonzalez, R. Woods, and S. Eddins. *Digital image processing using MATLAB*. Prentice-Hall, Upper Saddle River, NJ, 2003. 37

[35] B. C. Goodwin and L. E. H. Trainor. Tip and whorl morphogenesis in acetabularia by calcium-regulated strain fields. *Journal of Theoretical Biology*, 117(1):79–106, 1985. 11, 13

[36] P. G. Groh. Multi-view imaging of *Drosophila* embryos. Master's thesis, University of Waterloo, Waterloo, Ontario, 2008. 37

[37] A. K. Harris. Is cell sorting caused by differences in the work of intercellular adhesion? A critique of the Steinberg hypothesis. *Journal of Theoretical Biology*, 61(2):267–285, 1976. 9, 10

[38] A. K. Harris. *Multicellular Mechanics in the Creation of Anatomical Structures*. NATO ASI series. Series H, Cell biology. Springer-Verlag, Berlin ; New York, 1994. 7, 8, 9, 10, 14

[39] S. S. Haykin. *Modern filters*. Collier Macmillan, New York : London, 1989. 22

[40] A. Heisterkamp, J. Baurngart, I. Z. Maxwell, A. Ngezahayo, E. Mazur, and H. Lubatschowski. Fs-laser scissors for photobleaching, ablation in fixed samples and living cells, and studies of cell mechanics. *Laser Manipulation of Cells and Tissues*, 82:293–307, 2007. 11

[41] S. Hilgenfeldt, S. Erisken, and R. Carthew. Physical modeling of cell geometric order in an epithelial tissue. *Proceedings of the National Academy of Sciences*, 105(3):907, 2008. 10

[42] J. Holtfreter. Gewebeaffinität, ein mittel der embryonalen formbildung. *Archiv für Experimentelle Zellforschung*, 23:169–209, 1939. 8

[43] M. L. Honig and D. G. Messerschmitt. *Adaptive filters: structures, algorithms, and applications*. The Kluwer international series in engineering and computer science; SECS. Kluwer, Boston, 1984. 22, 23

[44] M. S. Hutson, Y. Tokutake, M.-S. Chang, J. W. Bloor, S. Venakides, D. P. Kiehart, and G. S. Edwards. Forces for morphogenesis investigated with laser microsurgery and quantitative modeling. *Science*, 300(5616):145–149, 2003. 11, 13

[45] M. S. Hutson, J. Veldhuis, X. Ma, H. E. Lynch, P. G. Cranston, and G. W. Brodland. Combining laser microsurgery and finite element modeling to assess cell-level epithelial mechanics. *Biophysical Journal*, 97(12):In press, 2009. 1, 11, 13, 17, 19

[46] D. E. Ingber. Cellular tensegrity - defining new rules of biological design that govern the cytoskeleton. *Journal of Cell Science*, 104:613–627, 1993. 12

[47] D. E. Ingber. Tensegrity: The architectural basis of cellular mechanotransduction. *Annual Review of Physiology*, 59:575–599, 1997. PT: J; TC: 624. 12

[48] R. M. Johnstone, C. R. J. Johnson, R. R. Bitmead, and B. D. O. Anderson. Exponential convergence of recursive least squares with exponential forgetting factor. *Systems & Control Letters*, 2(2):77–82, 1982. 24

[49] P. Karfunkel. The mechanisms of neural tube formation. *International Review of Cytology - A Survey of Cell Biology*, 38:245–271, 1974. 8

[50] D. P. Kiehart, C. G. Galbraith, K. A. Edwards, W. L. Rickoll, and R. A. Montague. Multiple forces contribute to cell sheet morphogenesis for dorsal closure in drosophila. *The Journal of Cell Biology*, 149(2):471–490, 2000. 11, 29

[51] J. S. Kim and S. X. Sun. Continuum modeling of forces in growing viscoelastic cytoskeletal networks. *Journal of Theoretical Biology*, 256(4):596–606, 2009. 14

[52] D. Kong, B. Ji, and L. Dai. Nonlinear mechanical modeling of cell adhesion. *Journal of Theoretical Biology*, 250(1):75–84, 2008. 14

[53] M. Krieg, Y. Arboleda-Estudillo, P. Puech, J. Käfer, F. Graner, D. Müller, and C. Heisenberg. Tensile forces govern germ-layer organization in zebrafish. *Nature Cell Biology*, 10(4):429–436, 2008. 10

[54] S. Kumar and P. R. LeDuc. Dissecting the molecular basis of the mechanics of living cells. *Experimental Mechanics*, 49(1):11–23, 2009. 11

[55] T. Lecuit and P. Lenne. Cell surface mechanics and the control of cell shape, tissue patterns and morphogenesis. *Nature Reviews Molecular Cell Biology*, 8(8):633–644, 2007. 10

[56] S.-H. Leung and C. F. So. Gradient-based variable forgetting factor rls algorithm in time-varying environments. *IEEE Transactions on Signal Processing*, 53(8):3141–3151, 2005. 24

[57] D. Longo, S. M. Peirce, T. C. Skalak, L. Davidson, M. Marsden, B. Dzamba, and D. W. DeSimone. Multicellular computer simulation of morphogenesis: blastocoel roof thinning and matrix assembly in *xenopus laevis*. *Developmental Biology*, 271(1):210–222, 2004. 12

[58] X. Ma, H. E. Lynch, P. C. Scully, and M. S. Hutson. Probing embryonic tissue mechanics with laser hole drilling. *Physical biology*, 6(3):036004 (12pp), 2009. 11

[59] I. Miller, J. E. Freund, and R. A. Johnson. *Miller & Freund's Probability and Statistics for Engineers*. Prentice Hall, Upper Saddle River, N.J., 2000. 23, 49

[60] J. M. Mitchison and M. M. Swann. The mechanical properties of the cell surface. 1. the cell elastimeter. *Journal of Experimental Biology*, 31(3):443–461, 1954. 5, 6

[61] C. E. Morris and U. Homann. Cell surface area regulation and membrane tension. *The Journal of Membrane Biology*, 179(2):79–102, 2001. 5, 7

[62] S. Narasimhan. Linear systems, control and identification. CivE 700 Course Notes. University of Waterloo, Waterloo Ontario, 2008. 21, 22

[63] J. C. Nash. *Compact Numerical Methods for Computers*. Adam Hilget Ltd., Bristol, 1979. 21, 22, 32

[64] A. E. Needham. *Regeneration and Wound-healing*. Methuen; New York, London, 1952. 11

[65] G. M. Odell, G. Oster, P. Alberch, and B. Burnside. The mechanical basis of morphogenesis. *Developmental Biology*, 85(2):446–462, 1981. 4, 7, 11, 13, 19

[66] C. Paleologu, J. Benesty, and S. Ciochina. A robust variable forgetting factor recursive least-squares algorithm for system identification. *IEEE Signal Processing Letters*, 15:597–600, 2008. 24

[67] E. Palsson. A three-dimensional model of cell movement in multicellular systems. *Future Generation Computer Systems*, 17(7):835–852, 2001. 14

[68] W. Press, S. Teukolsky, W. Vetterling, and B. Flannery. *Numerical Recipes 3rd Edition: The Art of Scientific Computing*. Cambridge University Press, 2007. 37, 38

[69] M. Rauzi, P. Verant, T. Lecuit, and P. Lenne. Nature and anisotropy of cortical forces orienting *Drosophila* tissue morphogenesis. *Nature Cell Biology*, 10(12):1401–1410, 2008. 10

[70] A. Rodriguez-Diaz, Y. Toyama, D. L. Abravanel, J. M. Wiemann, A. R. Wells, U. S. Tulu, G. S. Edwards, and D. P. Kiehart. Actomyosin purse strings: renewable resources that make morphogenesis robust and resilient. *HFSP Journal*, 2(4):220–237, 2008. 11

[71] B. Rubinstein, K. Jacobson, and A. Mogilner. Multiscale two-dimensional modeling of a motile simple-shaped cell. *Multiscale Modeling & Simulation*, 3(2):413–439, 2005. 14

[72] C. F. So, S. C. Ng, and S. H. Leung. Gradient based variable forgetting factor rls algorithm. *Signal Processing*, 83(6):1163–1175, 2003. 24

[73] S. Song, J.-S. Lim, S. Baek, and K.-M. Sung. Gauss newton variable forgetting factor recursive least squares for time varying parameter tracking. *Electronics Letters*, 36(11):988–990, 2000. 24

[74] D. Stamenovic and M. F. Coughlin. The role of prestress and architecture of the cytoskeleton and deformability of cytoskeletal filaments in mechanics of adherent cells: a quantitative analysis. *Journal of Theoretical Biology*, 201(1):63–74, 1999. 12

[75] D. Stamenovic, J. J. Fredberg, N. Wang, J. P. Butler, and D. E. Ingber. A microstructural approach to cytoskeletal mechanics based on tensegrity. *Journal of Theoretical Biology*, 181(2):125–136, 1996. 12

[76] G. D. Stark. *Spina Bifida: Problems and Management*. Blackwell Scientific Publications ; distributed by J. B. Lippincott, Oxford : Philadelphia, 1977. 2

[77] M. S. Steinberg. On the mechanism of tissue reconstruction by dissociated cells, I. population kinetics, differential adhesiveness, and the absence of directed migration. *Proceedings of the National Academy of Sciences*, 48(9):1577–1582, 1962. 8, 9, 12

[78] M. S. Steinberg. Does differential adhesion govern self-assembly processes in histogenesis? Equilibrium configurations and the emergence of a hierarchy among populations of embryonic cells. *Journal of Experimental Zoology*, 173(4):395–433, 1970. 8, 9, 12

[79] M. S. Steinberg. Cell-cell recognition in multicellular assembly: levels of specificity. In A. S. G. Curtis, editor, *Symposia of the Society for Experimental Biology*, volume 32, pages 25–49, 1978. 11, 12

[80] W. Supatto, D. Debarre, B. Moulia, E. Brouzes, J. L. Martin, E. Farge, and E. Beaurepaire. In vivo modulation of morphogenetic movements in drosophila embryos with femtosecond laser pulses. *Proceedings of the National Academy of Sciences of the United States of America*, 102(4):1047–1052, 2005. 11

[81] D. W. Thompson. *On Growth and Form*. Cambridge University Press, Cambridge, [Cambridgeshire], 1942. 11

[82] P. L. Townes and J. Holtfreter. Directed movements and selective adhesion of embryonic amphibian cells. *Journal of Experimental Zoology*, 128(1):53–120, 1955. 8

[83] Y. Toyama, X. G. Peralta, A. R. Wells, D. P. Kiehart, and G. S. Edwards. Apoptotic force and tissue dynamics during drosophila embryogenesis. *Science*, 321(5896):1683–1686, 2008. 11

[84] E. R. Tufte. *The Visual Display of Quantitative Information*. Graphics Press, Cheshire, CT, 2^{nd} edition, 2001. 66

[85] D. Viens. *A 3D finite element model for the mechanics of cell-cell interactions*. PhD thesis, University of Waterloo, 2006. 12

[86] H. V. Wilson. On some phenomena of coalescence and regeneration in sponges published with the permission of hon. geo. m. bowers, us commissioner of fisheries. *Journal of Experimental Zoology*, 5(2), 1907. 8

[87] J. Yang and G. W. Brodland. Estimating interfacial tension from the shape histories of cells in compressed aggregates: A computational study. *Annals of Biomedical Engineering*, 37(5):1019–1027, 2009. 13

[88] P. C. Young. Applying parameter estimation to dynamic systems. I. *Control Engineering*, 16(10):119–125, 1969. 24

[89] P. C. Young. Applying parameter estimation to dynamic systems. II. *Control Engineering*, 16(11):118–126, 1969. 24